

Kjeld Fjeldberg

Laboratory Testing of Virtual Inertia Provided by Converters in Weak Grids

Master's thesis in Energy and Environmental Engineering

Supervisor: Kjetil Uhlen and Trond Leiv Toftevaag

January 2021



Norwegian University of
Science and Technology

Kjeld Fjeldberg

Laboratory Testing of Virtual Inertia Provided by Converters in Weak Grids

Master's thesis in Energy and Environmental Engineering
Supervisor: Kjetil Uhlen and Trond Leiv Toftevaag
January 2021

Norwegian University of Science and Technology
Faculty of Information Technology and Electrical Engineering
Department of Electric Power Engineering



Abstract

Increasing penetration of intermittent renewable energy production raises the need for flexible energy storage to ensure the electric grid’s frequency balance. Pumped hydropower is the most mature technology to meet this demand. With variable speed drive the potential to respond to rapid fluctuations in the grid is improved. However, decoupling the synchronous machine from the grid with power electronics decouples the frequencies, and as a result, the inertia support of the machine is lost. This thesis’s primary motivation is the increasing interest in and the need for artificial inertia in power systems.

This thesis aims to test the virtual inertia capabilities of a voltage source converter (VSC) connected variable speed hydropower plant (VSHP) in a laboratory experiment. The laboratory experiment has a generator/motor set consisting of a 75 kVA synchronous generator and 45 kW DC-motor. The synchronous machine will act as a single-machine equivalent of a weak grid while the hydropower plant is approximated with a VSC, supplied by a DC-source. A conventional PLL-synchronised control system regulates the converter with an added virtual inertia control loop. The method used to emulate virtual inertia consists of a regular droop control combined with a branch regulating on the derivative of the frequency (df/dt). A simplified sketch of the laboratory set-up is shown in Figure 1.

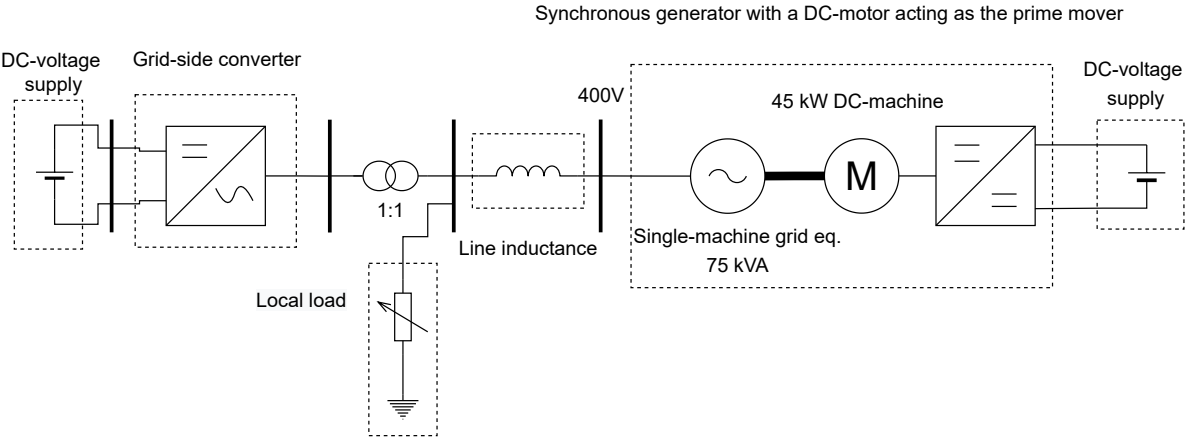


Figure 1: Simplified overview of the laboratory set-up used for virtual inertia experiments.

It is found that the inertia control loop effectively contributes with frequency support. When droop and df/dt control was added to the converter control, the frequency deviation was reduced

with 50 % compared to the base case. The base case's frequency deviation was found to be 2.6 Hz while for df/dt inertia emulation (IE) the frequency deviation was found to be 1.3 Hz. It is possible to increase the frequency support further, but this comes at the cost of the stability of the system. The inertia support of the converter is constrained by stability limits of the converter and the rated power. The stability limits were identified in this thesis for the given system.

Another objective of this thesis was to identify the electrical parameters of the synchronous generator used in the set-up for future simulation studies. Due to the old age of the machine in question, it was deemed too hazardous to perform the traditional short circuit test. Three load shedding experiments were therefore performed to estimate the standard parameters, saturation effects were not considered. These tests were a d -axis, q -axis and an arbitrary axis load rejection test. The result from the estimation is presented in Table 1. A simulation model was established to evaluate the accuracy of the parameter estimation. The simulation results were promising, and it is deemed that the parameters were estimated with an accuracy of a few percentages. The leakage reactance was not estimated, but it can be assumed that this value lies in the range of 10 - 15 % of the d -axis reactance.

Table 1: Summary of the Estimated Electrical Parameters for the Siemens-Schuckert Synchronous Machine. The Impedance Base is 2.406 Ω .

| Parameter | Estimated Value |
|------------|-----------------|
| R_a | 0.0236 pu |
| x_d | 0.7029 pu |
| x'_d | 0.1657 pu |
| x''_d | 0.1051 pu |
| x_q | 0.3542 pu |
| x''_q | 0.1012 pu |
| T'_d | 0.42 s |
| T'_{do} | 1.80 s |
| T''_d | 0.007 s |
| T''_{do} | 0.011 s |
| T''_q | 0.029 s |
| T''_{qo} | 0.10 s |

Sammendrag

Økende andel av uregelmessig fornybar energiproduksjon i nettet gir et økt behov for fleksibel energilagring for å sikre frekvensbalansen. Pumpekraftverk er den mest modne teknologien for å dekke dette behovet. Med variabel hastighet blir muligheten for å respondere til raske endringer i nettet forbedret. Når man kobler synkronmaskina fra nettet med kraftelektronikk blir frekvensene frikoblet og man mister det mekaniske treghetsmomentet til maskina. Hovedformålet med denne oppgaven er den økende interessen og behovet for virtuelt treghetsmoment.

Hensikten med denne oppgaven er å teste potensialet for å skape virtuelt treghetsmoment i et pumpekraftverk med variabel hastighet i et laboratoriumsforøk. Laboratoriumsoppsettet har en 75 kVA synkronmaskin og en 45 kW DC-motor. Synkronmaskina skal representere et svakt nett, mens vannkraftverket er forenklet med en spenningskildeomformer som er forsynt av en DC-kilde. Et konvensjonelt PLL-synkronisert styresystem er valgt for omformereren. I tillegg til dette er det lagt til en supplementær kontrollsløyfe for å skape virtuelt treghetsmoment. Denne sløyfa består av en grein med droopregulering og en grein som gir et pådrag som er omvendt proporsjonalt med den deriverte av frekvensen (df/dt). En forenklet skisse over laboratoriumsoppsettet er vist i Figur 2.

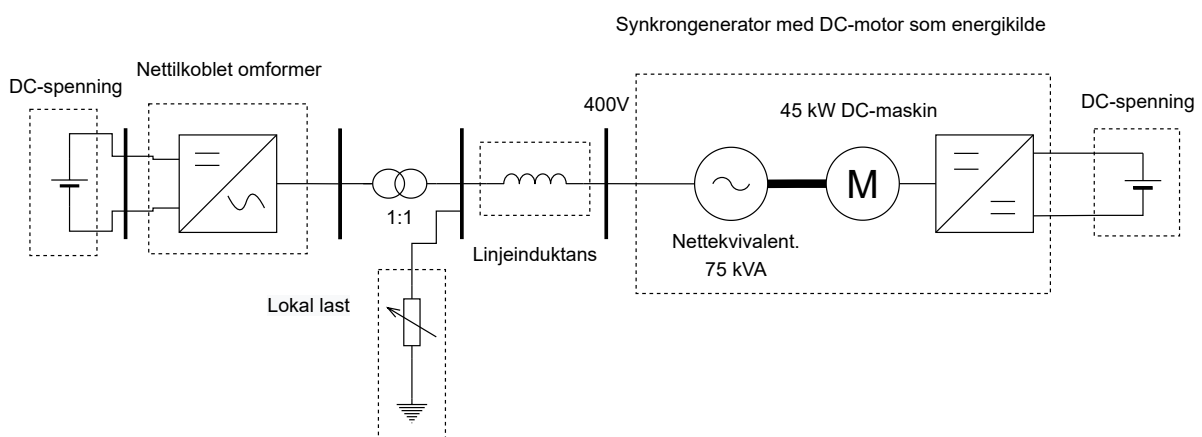


Figure 2: Forenklet oversikt over laboratoriumsoppsettet brukt for testing av virtuelt treghetsmoment.

Forsøket viste at kontrollsløyfa for treghetsemulering effektivt bidro med frekvensstøtte. Med både droop og df/dt regulering aktivert ble frekvensfallet redusert med 50 %, sammenliknet med den konvensjonelle omformerstyringen. For den konvensjonelle reguleringa var frekvensfallet

2,6 Hz, mens for reguleringsystemet med treghetsemulering ble frekvensfallet 1,3 Hz. Det var mulig å øke frekvensstøtten noe mer, men dette på bekostning av stabiliteten til systemet. Stabilitetsgrensene for det gitte systemet ble identifisert.

Et annet formål med denne oppgaven var å identifisere de elektriske standardparameterne for synkronmaskina brukt i forsøkene. Dette for fremtidige simuleringsstudier. Siden maskina var gammel ble det vurdert at den tradisjonelle kortslutningstesten kunne medføre skade på maskina. Det ble derfor utført lastavslagstester for å estimere verdiene. Testene som ble gjennomført var d -akse, q -akse og arbitrær akse lastavslagstest. Metninga av maskina ble ikke tatt hensyn til. Resultatene fra parameterestimeringa er vist i Tabell 2. En simuleringsmodell ble etablert for å kunne vurdere presisjonen for de estimerte parameterne. Det ble anslått at parameterne var innenfor de virkelige verdiene med noen få prosent. Verdi for lekkreaktansen ble ikke estimert, men man kan anta at denne verdien er 10 – 15 % av d -aksereaktansen.

Table 2: Oppsummering av de estimerte elektriske parameterne for synkronmaskina produsert av Siemens-Schuckert. Impedansbasen er 2,406 Ω .

| Parameter | Estimert verdi |
|------------|----------------|
| R_a | 0,0236 pu |
| x_d | 0,7029 pu |
| x'_d | 0,1657 pu |
| x''_d | 0,1051 pu |
| x_q | 0,3542 pu |
| x''_q | 0,1012 pu |
| T'_d | 0,42 s |
| T'_{do} | 1,80 s |
| T''_d | 0,007 s |
| T''_{do} | 0,011 s |
| T''_q | 0,029 s |
| T''_{qo} | 0,10 s |

Acknowledgements

I want to thank the technical staff at NTNU Service-lab for helping me with the practical considerations of establishing the laboratory set-up. Especially Bård Almås for installing the control cabinet for the "big red" synchronous machine. I would also like to thank Kjell Ljøkelsøy at SINTEF for showing me the ropes of the smart grid laboratory and for his great enthusiasm for laboratory experiments. A special thanks to Salvatore D'Arco and Raymundo E. Torres-Olguin for helping me with the control of the converter and operating the OPAL-RT. I would also like to thank my supervisor Kjetil Uhlen for sharing his profound insights into electrical power systems. Special gratitude to co-supervisor Trond Leiv Toftevaag for countless good discussions of both academic and informal character and inspiring me throughout my studies. Lastly, I would like to thank all of my friends and colleagues at both EMIL and Studentersamfundet for five great years in Trondheim.

Table of Contents

| | |
|---|-------------|
| Abstract | i |
| Sammendrag | iii |
| Acknowledgement | v |
| Table of Contents | x |
| List of Tables | xii |
| List of Figures | xvi |
| Nomenclature | xvii |
| Abbreviations | xxi |
| 1 Introduction | 1 |
| 1.1 Background and Motivation | 1 |
| 1.2 Objective | 2 |
| 1.3 Scope of Work | 2 |
| 1.4 Structure of the Thesis | 3 |
| 1.5 Limitations | 3 |
| 2 Background Theory | 5 |
| 2.1 Frequency Stability in the Electric Grid | 5 |
| 2.1.1 Swing Equation | 6 |
| 2.1.2 Rate of Change of Frequency | 8 |
| 2.1.3 Frequency Control | 9 |
| 2.2 Variable Speed Hydro Power | 10 |
| 2.2.1 Different Technologies for Variable Speed Hydro Power | 10 |
| 2.2.2 Potential Benefits of Variable Speed Hydro Power | 11 |
| 2.3 Virtual Inertia | 11 |
| 2.3.1 Virtual Inertia by Supplementary Control | 11 |
| 2.3.2 Virtual Synchronous Machine (VSM) | 12 |
| 2.4 Modelling of the Salient-Pole Synchronous Machine | 13 |

| | | |
|----------|---|-----------|
| 2.5 | Parameter Estimation for the Salient-Pole Machine | 16 |
| 2.5.1 | d -axis Parameters | 17 |
| 2.5.2 | q -axis Parameters | 18 |
| 3 | Laboratory Set-Up and Equipment | 23 |
| 3.1 | Description of Laboratory Set-Up for Virtual Inertia Experiments | 23 |
| 3.2 | Description of Laboratory Set-Up for Parameter Estimation Experiments | 26 |
| 3.3 | Description of Equipment | 27 |
| 3.3.1 | Synchronous Generator | 27 |
| 3.3.2 | Excitation Control for the Synchronous Generator | 28 |
| 3.3.3 | DC-Motor | 29 |
| 3.3.4 | Control System for the DC-Motor | 29 |
| 3.3.5 | Transformer | 31 |
| 3.3.6 | Water-Cooled Load Resistance | 31 |
| 3.3.7 | Line Inductance | 31 |
| 3.3.8 | 2-Level Voltage Source Converter (VSC) | 31 |
| 3.3.9 | Control system for the VSC | 32 |
| 3.4 | Description of Measurement Equipment | 34 |
| 3.4.1 | Tektronix Oscilloscopes | 34 |
| 3.4.2 | PicoZed-Based Processor Board for Synchronous Generator Measure- ments | 34 |
| 3.4.3 | LEM Voltage and Current Transducers | 35 |
| 3.4.4 | Speed Measurement with Rotary Encoder | 35 |
| 4 | Preliminary Laboratory Work | 37 |
| 4.1 | Measurement of Armature Resistance | 37 |
| 4.2 | Tuning of Speed Controller for the DC-Motor Control System | 37 |
| 4.2.1 | Initial Tuning | 37 |
| 4.2.2 | Tuning with a Step in Electrical Load | 38 |
| 4.3 | Tuning of Automatic Voltage Regulator (AVR) | 40 |
| 4.4 | Initial Test of the Virtual Inertia Laboratory Set-Up | 43 |
| 4.4.1 | Test with Automatic Tuning of the AVR | 43 |
| 4.4.2 | Test with Manual Tuning of the AVR | 43 |
| 4.5 | Accuracy of Measurements | 46 |
| 4.5.1 | Voltage Measurements | 46 |
| 4.5.2 | Speed Measurements | 46 |
| 4.5.3 | Active Power Measurements | 47 |
| 4.5.4 | Current Measurements | 47 |
| 4.5.5 | Summary of the Measurements Accuracy Evaluation | 48 |
| 5 | Results and Discussion - Virtual Inertia Experiments | 49 |
| 5.1 | Case Description | 49 |
| 5.2 | Comparison of the Different Converter Control Schemes | 52 |
| 5.3 | Comparison of Droop Constant and df/dt Constant | 55 |
| 5.4 | Stability Limit for the Virtual Inertia Loop | 56 |
| 5.5 | Comparison of Different Initial Load Scenarios | 59 |
| 5.6 | Comparison of Load Increase and Load Rejection | 61 |

| | | |
|----------|--|------------|
| 5.7 | Drop in DC-Voltage | 62 |
| 5.8 | Active Power Oscillations | 62 |
| 6 | Results and Discussion - Parameter Estimation Experiments | 65 |
| 6.1 | Base Values for the Per-Unit Calculations | 65 |
| 6.2 | <i>d</i> -axis Parameter Test | 65 |
| 6.3 | <i>q</i> -axis Parameter Tests | 70 |
| 6.3.1 | <i>q</i> -axis Load Rejection Test | 70 |
| 6.3.2 | Arbitrary Axis Load Rejection Test | 71 |
| 6.4 | Summary and Discussion of Parameter Estimation Results | 73 |
| 6.5 | Comparison of Simulated Load Rejection Tests with Laboratory Results | 74 |
| 6.5.1 | Simulation Model | 74 |
| 6.5.2 | <i>d</i> -axis Load Rejection Simulation | 75 |
| 6.5.3 | Arbitrary Axis Load Rejection Simulation | 77 |
| 7 | Conclusion and Further Work | 81 |
| 7.1 | Conclusion | 81 |
| 7.2 | Further Work | 83 |
| | Bibliography | 85 |
| | Appendices | 89 |
| A | Results - Virtual Inertia | 89 |
| A.1 | Close-Up of Initial ROCOF After Step in Load | 89 |
| A.2 | Close-Up of the Active Power Flow From the Generator During Step in Load . | 90 |
| A.3 | Close-Up of the Active Power Flow From the Converter During Step in Load . | 90 |
| A.4 | Frequency Plots for the Remaining Cases of the Stability Limit Study | 91 |
| A.5 | Fast Fourier Transform Analysis of Case 35 | 92 |
| A.6 | Current for Unstable Case | 93 |
| A.7 | Active Power Plots for the Inital Load Conditions Study | 94 |
| B | Results - Parameter Estimation | 97 |
| B.1 | <i>d</i> -axis Parameter Estimation | 97 |
| B.2 | <i>q</i> -axis Parameter Estimation | 100 |
| B.2.1 | <i>q</i> -axis Load Rejection Test | 100 |
| B.2.2 | Arbitrary Axis Load Rejection Test | 101 |
| B.3 | OCC and SCC for the Siemens-Schuckert Synchronous Machine | 102 |
| C | Preliminary Laboratory Work | 103 |
| C.1 | Voltage Measurements Circuit Diagram | 103 |
| C.2 | Voltage Measurements | 104 |
| C.3 | AVR Tuning | 105 |
| D | Laboratory Set-Up | 107 |
| D.1 | Control Cabinet for the Siemens-Schuckert Motor/Generator Set | 107 |
| D.2 | Picture of the VSC | 108 |
| D.3 | Picture of the EGSTON Power Amplifier | 109 |

| | | |
|-----|--|-----|
| D.4 | Screenshot of the Auto Tune Window in Basler BESTCOMSPlus Software . . | 110 |
| D.5 | Single-Line Schematic for the Laboratory Experiment | 111 |
| D.6 | Overview of the Smart Grid Laboratory | 112 |
| D.7 | Schematic of the Smart Grid Laboratory | 113 |

List of Tables

| | | |
|------|--|----|
| 1 | Summary of the Estimated Electrical Parameters for the Siemens-Schuckert Synchronous Machine. The Impedance Base is 2.406Ω | ii |
| 2 | Oppsummering av de estimerte elektriske parameterne for synkronmaskina produsert av Siemens-Schuckert. Impedansbasen er $2,406 \Omega$ | iv |
| 3.1 | List of the Main Components for the Virtual Inertia Experiment as Presented in Figure 3.2. | 25 |
| 3.2 | List of Equipment Used for Measurements in the Virtual Inertia Experiments. | 25 |
| 3.3 | List of the Main Components for the Parameter Estimation Experiments as Presented in Figure 3.3. | 26 |
| 3.4 | List of Equipment Used for Measurements in the Parameter Estimation Experiments. | 27 |
| 3.5 | Parameters for the Synchronous Machine. | 27 |
| 3.6 | Nameplate Values for the DC-Machine. | 29 |
| 4.1 | Measured Armature Resistance of the Siemens-Schuckert Synchronous Generator, Series-Star Connection. | 37 |
| 4.2 | Parameter Values for the Speed Controller. | 38 |
| 4.3 | The Gains for the AVR Proposed by Basler's Automatic Tuning Algorithm. | 40 |
| 4.4 | List of Gain Values Tested for Tuning of the AVR. | 41 |
| 4.5 | Control System Parameters for Initial Test of Laboratory Experiment. | 43 |
| 4.6 | List of AVR Gain Values Tested for the Initial Virtual Inertia Experiment. | 43 |
| 4.7 | List of Equipment Used for Accuracy Examination. | 46 |
| 4.8 | rms Armature Voltage of the Synchronous Generator Measured with Different Measurement Equipment. | 46 |
| 4.9 | Speed Measurements through the DC-motor Drive. | 47 |
| 4.10 | Active Power Measurements with Different Measurement Equipment. | 47 |
| 4.11 | Current Measurements with Different Measurement Equipment. | 47 |
| 5.1 | Case Description for the Virtual Inertia Experiments. | 50 |
| 5.2 | Control System Parameters of Laboratory Experiment. | 52 |
| 5.3 | Frequency Nadir for the Different Control Schemes. | 53 |
| 5.4 | Frequency Nadir and THD on Current From Converter for Different Droop Gains. | 57 |
| 5.5 | Frequency Nadir and THD on Current From Converter for Different df/dt Gains. | 57 |
| 5.6 | Initial and Peak Frequency for Case 42 and Case 43. | 61 |

| | | |
|------|---|----|
| 6.1 | Base Values for the Estimation of Parameters. | 65 |
| 6.2 | Initial Loading of the Synchronous Generator for the d -axis Test, Underexcited Operation. | 66 |
| 6.3 | Speed Reduction of the Generator During d -axis Load Rejection. | 69 |
| 6.4 | Initial Loading of the Synchronous Generator for the q -axis Test, Under-Excited Generator. | 70 |
| 6.5 | Initial Loading of the Synchronous Generator for the Arbitrary Axis Load Rejection Test, Overexcited Generator. | 71 |
| 6.6 | Summary of the Electrical Parameters for the Siemens-Schuckert Synchronous Machine. Per-unit values calculated with the base values presented in Chapter 6.1. | 73 |
| 6.7 | Initial Conditions for the Simulated d -axis Test. | 75 |
| 6.8 | Voltage Comparison for the d -axis Simulation. | 77 |
| 6.9 | Initial Conditions for the Simulated Arbitrary Axis Test. | 77 |
| 6.10 | Voltage Comparison for the Arbitrary Axis Simulation. | 78 |
| 7.1 | Summary of the Estimated Electrical Parameters for the Siemens-Schuckert Synchronous Machine. The Impedance Base is 2.406Ω | 82 |

List of Figures

| | | |
|------|---|-----|
| 1 | Simplified overview of the laboratory set-up used for virtual inertia experiments. | i |
| 2 | Forenklet oversikt over laboratoriumsoppsettet brukt for testing av virtuelt treghetsmoment. | iii |
| 1.1 | Overview of the laboratory set-up used for IE experiments. | 2 |
| 2.1 | Classification of power system stability [7]. | 5 |
| 2.2 | Frequency response of a loss of a large generator [13]. | 9 |
| 2.3 | Single-line diagram of the DFIM and the CFSM [14]. | 10 |
| 2.4 | Typical efficiency for variations in head and power output for a single speed and variable speed turbine [16]. | 11 |
| 2.5 | Several supplementary inertia control methods [9]. | 12 |
| 2.6 | Virtual inertia based on the swing equation [22]. | 13 |
| 2.7 | Simplified model of a salient-pole synchronous machine [23, p. 576]. | 14 |
| 2.8 | Phasor diagram of a overexcited salient-pole machine in generating mode [23, p. 578]. | 15 |
| 2.9 | Complete phasor diagram for an overexcited salient-pole machine in generator mode [7, p. 86]. | 16 |
| 2.10 | The equivalent circuit diagram for the salient-pole machine in steady-state [7, p. 87]. | 16 |
| 2.11 | Phasor diagram of the initial conditions for d -axis load rejection scenario, underexcited generator. | 17 |
| 2.12 | Transient development of the terminal voltage after load rejection of purely reactive load, d -axis load rejection scenario [26]. | 18 |
| 2.13 | Transient development of the field current after load rejection of purely reactive load, d -axis load rejection scenario [26]. | 19 |
| 2.14 | Phasor diagram of the initial conditions for q -axis load rejection scenario, underexcited generator. | 19 |
| 2.15 | Transient development of the field current after load rejection of reactive load, q -axis [26]. | 20 |
| 2.16 | An example of the d -axis voltage curve during an arbitrary axis load rejection [27]. | 21 |
| 3.1 | Overview of the laboratory set-up used for IE experiments. | 23 |
| 3.2 | Circuit diagram of the laboratory setup | 24 |
| 3.3 | Laboratory set-up for the parameter estimation experiments. | 26 |

| | | |
|------|---|----|
| 3.4 | Picture of the Siemens-Schuckert motor/generator (45 kW / 75 kVA) set. | 28 |
| 3.5 | Control panel for the Basler Electric DECS-250N digital excitation control system. | 29 |
| 3.6 | User interface for the DC-motor control unit (right) and the communication interface for the PicoZed processor card, as described in Chapter 3.4.2. | 30 |
| 3.7 | Block diagram of the control system for the Siemens-Schuckert DC-motor, based on [29]. | 30 |
| 3.8 | Block diagram of the PI-regulator used for speed control in the DC-motor control system, based on [29]. | 31 |
| 3.11 | Workflow using the OPAL-RT to control the converter, inspired by [35]. | 32 |
| 3.9 | Block diagram of the main control loops for the VSC control system. | 33 |
| 3.10 | Block diagram of the supplementary virtual inertia control loop. | 33 |
| 3.12 | Picture of the MSO 3014 mixed signal oscilloscope. | 34 |
| 4.1 | Plots of step responses for a step in reference from 300 rpm to 400 rpm with variations for proportional gain K_p and integral time constant T_i | 38 |
| 4.2 | Plot of step responses for a step in electrical load from no load to a resistance of 11.6 Ω | 39 |
| 4.3 | Step response for the synchronous generator's terminal voltage for a step in voltage reference from 0.95 pu to 1.1 pu with the gains suggested by Basler Electric automatic tuning algorithm. | 41 |
| 4.4 | Step response for the synchronous generator's terminal voltage for a step in voltage reference from 0.95 pu to 1.1 pu case 2 to 4. | 42 |
| 4.5 | Step response for the synchronous generator's terminal voltage for a step in voltage reference from 0.95 pu to 1.1 pu for case 5 to 7. | 42 |
| 4.6 | Step in load from 39.4 Ω to 7.8 Ω with AVR gains $K_p = 40$ and $K_i = 0$ | 44 |
| 4.7 | Step in load from 39.4 Ω to 7.8 Ω with AVR gains $K_p = 40$ and $K_i = 8$ | 45 |
| 4.8 | Terminal voltages of the generator for a step in load from 39.4 Ω to 7.8 Ω | 45 |
| 5.1 | Frequency for the three different control schemes. | 53 |
| 5.2 | Active power delivered from the generator for the three different control schemes. | 54 |
| 5.3 | Active power delivered from the converter for the three different control schemes. | 55 |
| 5.4 | Frequency during a step in load with different droop gains. | 56 |
| 5.5 | Frequency during a step in load with different droop gains. | 57 |
| 5.6 | Frequency during a step in load with different df/dt gains. | 58 |
| 5.7 | Frequency during a step in load with positive, negative and zero reactive power flow out from the converter. The active power load is shared between the generator and converter. | 59 |
| 5.8 | Frequency during a step in load with positive, negative and zero reactive power flow out from the generator. The generator is running no-load. | 60 |
| 5.9 | Frequency during a step up, and step down of a load of 13.3 kW. | 61 |
| 5.10 | Active power from the converter and voltage during a drop in voltage on the DC-side of the converter. | 62 |
| 5.11 | Active power for three different cases of droop and df/dt gains. | 63 |
| 6.1 | The envelope of the voltage during d -axis load rejection. | 66 |
| 6.2 | Close-up of the voltage envelope during load shedding. | 67 |
| 6.3 | Amplification of the field current for the estimation of T'_{do} | 68 |

| | | |
|------|---|-----|
| 6.4 | Amplification of the field current for the estimation of T''_{do} | 69 |
| 6.5 | Voltage envelope of the terminal voltage during q -axis load rejection. | 70 |
| 6.6 | Results from the arbitrary axis parameter test. | 71 |
| 6.7 | Amplification of the d -axis armature voltage envelope plotted on a semilogarithmic scale. | 72 |
| 6.8 | Model used for simulating of load rejection tests. | 75 |
| 6.9 | Simulated armature voltage envelope from the simulated d -axis load rejection test plotted together with the laboratory results. | 76 |
| 6.10 | d -axis armature voltage envelope for the simulated arbitrary load rejection test, plotted together with the laboratory result. | 78 |
| 6.11 | Simulated armature voltage envelope, plotted together with the laboratory result. | 79 |
| | | |
| A.1 | Close-up of Figure 5.1 showing the initial ROCOF after a step in electrical load from 11.6Ω to 5.7Ω | 89 |
| A.2 | Close-up of Figure 5.2 showing the active power flow from the generator after a step in electrical load from 11.6Ω to 5.7Ω | 90 |
| A.3 | Close-up of Figure 5.3 showing the active power flow from the converter after a step in electrical load from 11.6Ω to 5.7Ω | 90 |
| A.4 | Frequency during step in load with different droop gains, rest of the cases. | 91 |
| A.5 | Frequency during step in load with different droop gains, rest of the cases. | 91 |
| A.6 | FFT analysis of current from the converter in case 35. | 92 |
| A.7 | Current for unstable case 36, $K_w = 5$, $K_j = 12$ | 93 |
| A.8 | Active power from generator during step in load with positive, negative and zero reactive power flow out from the converter. The active power load is shared between the generator and converter. | 94 |
| A.9 | Active power from converter during step in load with positive, negative and zero reactive power flow out from the converter. The active power load is shared between the generator and converter. | 94 |
| A.10 | Active power from generator during step in load with positive, negative and zero reactive power flow out from the generator. The generator is running no-load. | 95 |
| A.11 | Active power from converter during step in load with positive, negative and zero reactive power flow out from the generator. The generator is running no-load. | 95 |
| | | |
| B.1 | Instantaneous values of the terminal voltages during d -axis load rejection. | 97 |
| B.2 | Field current during d -axis load rejection. | 98 |
| B.3 | Speed of motor/generator set during d -axis load rejection. | 99 |
| B.4 | Instantaneous values of the terminal voltages during the q -axis load rejection test. | 100 |
| B.5 | Instantaneous values of the terminal voltages during the arbitrary axis load rejection test. | 101 |
| B.6 | The open circuit characteristics and the short circuit characteristics for the Siemens-Schuckert synchronous machine as measured by [25]. | 102 |
| | | |
| C.1 | Circuit for voltage measurement for phase L1-L2 on the synchronous generator, identical circuits exist for L2-L3 and L3-L1 [42]. | 103 |
| C.2 | The three phase voltage as measured with the oscilloscope, generator running open circuit with rms voltage of 400.4 V as measured with the multimeter. | 104 |
| C.3 | Step response for the terminal voltage of the synchronous generator for a step in voltage reference from 0.95 pu to 1.1 pu. | 105 |

| | | |
|-----|---|-----|
| D.1 | Picture of the control cabinet for the Siemens-Schuckert motor/generator set. . . | 107 |
| D.2 | Picture of the voltage source converter. | 108 |
| D.3 | Picture of the EGSTON 200 kVA power amplifier. | 109 |
| D.4 | Screenshot of the Auto Tune Window in Basler BESTCOMSPlus Software . . | 110 |
| D.5 | Single-line schematic for the laboratory experiment. | 111 |
| D.6 | Overview of the smart grid laboratory [43]. | 112 |
| D.7 | Single-line schematic of the buses in the smart grid Laboratory [43]. | 113 |

Nomenclature

Greek

| | |
|---------------|---|
| α | Angular acceleration |
| δ | Rotor angle or power angle |
| ω | Angular velocity |
| ω_0 | Rated angular velocity of rotor, electrical rad/s |
| ω_m | Angular velocity of rotor, mechanical rad/s |
| ω_r | Angular velocity of rotor, electrical rad/s |
| ω_{0m} | Rated angular velocity of rotor, mechanical rad/s |
| Φ | Magnetic flux |
| ϕ | Phase angle |
| τ_e | Electrical torque |
| τ_m | Mechanical torque |

Latin

| | |
|---------------|--|
| E_d | d -component of armature emf |
| E_f | Field emf |
| E_q | q -component of armature emf |
| E_r | Resultant air-gap emf in a synchronous machine |
| I_a | Armature current |
| I_d | d -component of the armature current |
| I_q | q -component of the armature current |
| \mathcal{P} | Permeance |

| | |
|----------------|--|
| \vec{F}_d | d -component of armature mmf |
| \vec{F}_f | Field mmf |
| \vec{F}_q | q -component of armature mmf |
| \vec{F}_{ar} | Armature mmf |
| f | Frequency |
| f_0 | Rated frequency |
| H | Per unit inertia constant |
| I_f | Field winding current |
| J | Moment of inertia |
| j | The imaginary unit |
| K_D | Damping-torque coefficient |
| P | Active power |
| P_f | Number of pole pairs |
| Q | Reactive power |
| R_a | Armature reactance of a synchronous machine |
| S | Apparent power |
| S_n | Nominal apparent power |
| T''_{qo} | Open-circuit subtransient q -axis time constant |
| T''_{qo} | Subtransient q -axis time constant |
| T_a | Mechanical starting time constant for the synchronous machine |
| T''_{do} | Open-circuit subtransient d -axis time constant |
| T'_{do} | Open-circuit transient d -axis time constant |
| T''_d | Short-circuit subtransient d -axis time constant |
| T'_d | Short-circuit transient d -axis time constant |
| V_t | Terminal voltage of electrical machine |
| x''_d | Total subtransient d -axis reactance including leakage reactance |
| x'_d | Total transient d -axis reactance including leakage reactance |
| x_d | Total d -axis reactance including leakage reactance |

| | |
|---------|--|
| x_l | leakage reactance |
| x_q'' | Total subtransient q -axis reactance including leakage reactance |
| x_q' | Total transient q -axis reactance including leakage reactance |
| x_q | Total q -axis reactance including leakage reactance |

Abbreviations

| | |
|--------------|-----------------------------------|
| AVR | Automatic Voltage Regulation |
| CFSM | Converter Fed Synchronous Machine |
| emf | Electromotive Force |
| IE | Inertia Emulation |
| mmf | Magnetomotive Force |
| PHIL | Power Hardware in the Loop |
| PLL | Phase-Locked Loop |
| ROCOF | Rate of Change of Frequency |
| THD | Total Harmonic Distortion |
| VSC | Voltage Source Converter |
| VSHP | Variable Speed Hydro Power |
| VSM | Virtual Synchronous Machine |

Introduction

1.1 Background and Motivation

The electric power grids are presently undergoing an extensive transformation, giving rise to a range of challenges to the grid's stability and integrity. Old thermal power plants and nuclear plants are being decommissioned and replaced with intermittent converter-interfaced renewable energy. In Europe, a trend for an increasing number of large-capacity DC-interconnections being installed is also seen. The increasing integration of intermittent renewable energy can make it challenging to balance electric power production and consumption. The large share of converter-interfaced generation will reduce the total amount of mechanical inertia that is an inherent feature of the traditional large synchronous generator. The increasing capacity of converter-interfaced production can lead to load situations where the total inertia in the grid is insufficient to withstand a large disturbance [1].

Energy storage will be crucial for supporting the balance between production and consumption [2]. Pumped-storage hydropower can play an essential role in this context, and it is the large-scale energy storage technology with the highest overall efficiency. Variable speed pumped hydropower has greater flexibility for frequency regulation than conventional pumped hydropower and can assist the integration of more intermittent renewable energy [3]. One method of enabling variable speed pumped hydropower is to use a converter fed synchronous machine (CFSM). This method uses a power electronic converter to decouple the pump/turbine's frequency from the power grid. However, this will also hide the synchronous machine's mechanical inertia from the grid, and virtual inertia is needed to maintain the machine's inertial support.

The use of virtual inertia can reduce the frequency nadir and help maintain frequency stability. Virtual inertia is created by the converter control system to emulate an inertial response from the converter. Virtual inertia is also called hidden inertia, artificial inertia or synthetic inertia, but the concept is the same [4]. Many different methods exist for creating inertia emulation (IE) and they range in complexity from a supplementary inertia control loop to the more complex emulation of a synchronous generator called virtual synchronous machine (VSM). Virtual inertia is deemed an essential solution for ensuring the total inertia is high enough in future power grids [5]. The aim of the present report is to study different existing methods for creating IE via experiments with a laboratory set-up.

1.2 Objective

This thesis is a continuation of a specialisation project [6] and aims to analyse the virtual inertia capabilities of a converter-interfaced power plant in a weak grid application. This will be done through experiments on a realistic 3-phase 400 V laboratory set-up with a 75 kVA synchronous generator acting as the weak grid and 60 kVA 2-level voltage source converter (VSC) presenting the converter interfaced power plant. A single-line diagram depicting the laboratory set-up is shown in Figure 1.1.

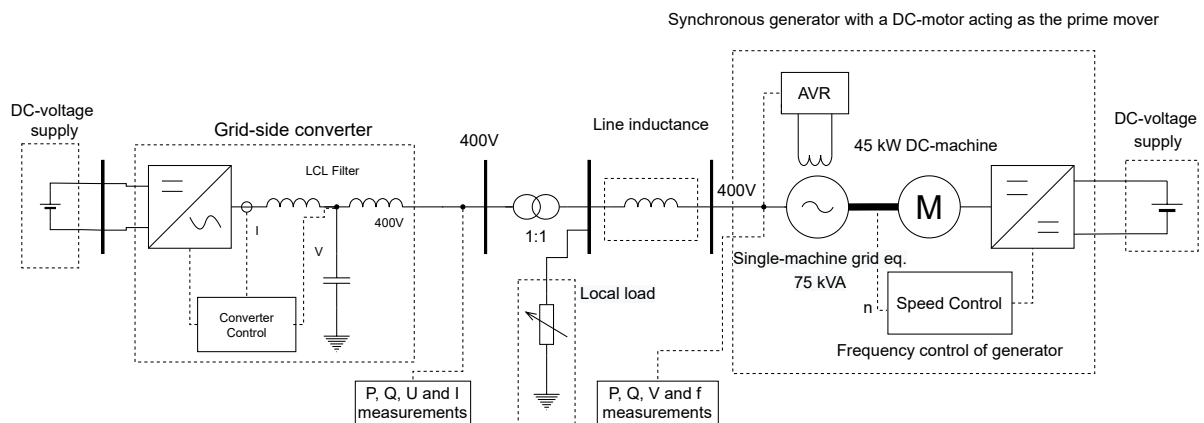


Figure 1.1: Overview of the laboratory set-up used for IE experiments.

1.3 Scope of Work

- Establish a laboratory set-up suitable for testing of artificial inertia capabilities.
- Identify the virtual inertia capabilities of the chosen system.
- Estimate the unsaturated electrical standard parameters of the synchronous generator to be used for future simulations studies.
- Verification of the estimated parameters of the synchronous generator with a simulation model.
- Preparation of sensors, instrumentation and measurements.
- Determine the stability limits of the virtual inertia control loops.
- Tuning of the AVR and the speed controller used for the synchronous generator.

1.4 Structure of the Thesis

Chapter 1 - *Introduction*: Provides the background for the thesis, the objective and scope of work

Chapter 2 - *Background Theory*: Presents the necessary background theory

Chapter 3 - *Laboratory Set-Up and Equipment*: Presents technical descriptions of the laboratory set-up, including the necessary measurement equipment.

Chapter 4 - *Preliminary Laboratory Work*: Present the preliminary laboratory work and a short discussion concerning measurement accuracy.

Chapter 5 - *Results and Discussion - Virtual Inertia Experiments*: Presents and discuss the results from the experiments considering virtual inertia

Chapter 6 - *Results and Discussion - Parameter Estimation Experiments*: Presents and discuss the results from the experiments considering the estimation of the electrical parameters of the synchronous generator, including a simulation comparison.

Chapter 7 - *Conclusion and Further Work*: Summarise and concludes the thesis and point out further work.

1.5 Limitations

The limitations of the virtual inertia experiments are as following:

- The virtual inertia experiments are limited to the grid side of the back-to-back converter. The power plant and the generator side of the converter is simplified as a DC-voltage source.
- The converter is not required to have grid forming capabilities or black start capabilities.
- Thermal conditions are not considered for the components used in the laboratory experiments.

The limitations of the parameter estimation are as following:

- Mechanical constants are not considered.
- Saturation effects are not considered.
- The accuracy of the parameter estimation is limited by the accuracy of the available measurement equipment.
- Thermal conditions are not considered for the components used in the laboratory experiments.

Background Theory

2.1 Frequency Stability in the Electric Grid

The power system stability can be seen as the grid’s ability to retain a stable operating point within the given requirements after being subjected to a disturbance. The stability problem can be grouped into three different main categories, as shown in Figure 2.1. These are rotor angle stability, frequency stability and voltage stability. Even though these different categories are not independent of each other (for example a frequency collapse will affect the voltage and vice versa) it can be practical to use these different classifications. The focus of this report will be on frequency stability.

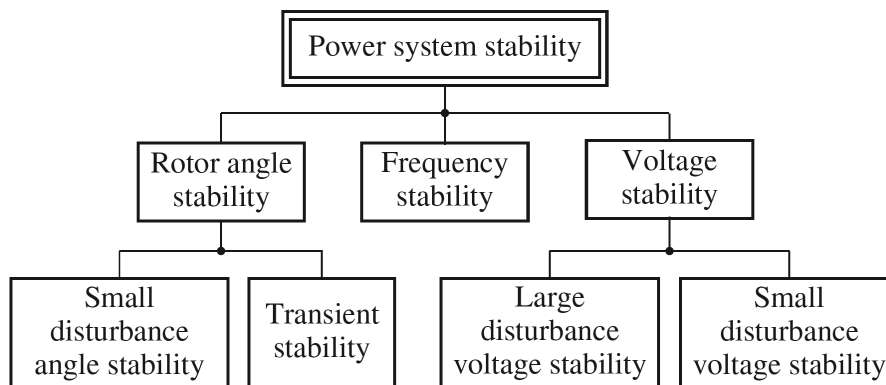


Figure 2.1: Classification of power system stability [7].

It is essential to keep the frequency within certain limits. The national grid codes define these limits for the respective synchronous area. For example, under normal conditions, the Nordic synchronous grid’s frequency should be within 50 ± 0.1 Hz [8]. The frequency is directly tied with the balance of active power in the grid. An unbalance between the total production and consumption will result in a change of frequency. The system should be designed to withstand the loss of the biggest generating unit [9]. An important contributing factor to maintaining the frequency stable is the total rotating kinetic energy stored in the grid. The inertia of the grid is the system’s ability to withstand changes. High inertia yields a large resistance to change of frequency and vice versa. The main contribution to inertia is the large synchronous generators. These aspects will be further explained in the following section.

2.1.1 Swing Equation

The swing equation is fundamental for the understanding of the initial frequency stability of the electric power grid. In the following subchapter a derivation of the swing equation based on Kundur [10, pp. 128-132] with inspiration from [7, pp. 170-172] and [11, pp. 13-17] is shown. The swing equation is derived from the general Newton's second law for uniform circular motion shown in Equation 2.1.

$$J\alpha = \sum \tau \quad (2.1)$$

Where J is the moment of inertia, α is the angular acceleration, and the right-hand side is the sum of the torques acting on the object. Specifying this to a turbine/generator set gives the following equation, noting that the angular velocity's time derivative is the same as the angular acceleration.

$$J \frac{d\omega_m}{dt} = \tau_m - \tau_e \quad (2.2)$$

Here J is the total moment of inertia for the generator/turbine set, ω_m is the mechanical rotational velocity, and τ_m and τ_e is the net mechanical torque and the electrical torque, respectively. An observation can be made for this equation. While the mechanical torque of the turbine changes slowly due to the mechanical time constants being relatively large, the electrical torque can change almost instantaneously when a fault or disturbance occurs on the generator's electrical side.

In Equation 2.3, the per-unit inertia constant, H , is introduced.

$$H = \frac{1}{2} \frac{J\omega_{0m}^2}{S_n} \quad (2.3)$$

Where ω_{0m} is the rated angular velocity of the rotor and S_n is the rated apparent power of the generator. The inertia constant can be seen as the rated kinetic energy of the generator normalised by the rated power. Having defined the inertia constant H , it is also possible to define the mechanical starting time constant for the synchronous generator T_a , which is the time required to accelerate the rotor from standstill to rated speed with rated torque [10].

$$T_a = 2H \quad (2.4)$$

The inertia constant can be used to normalise Equation 2.2. For this purpose H is rearranged in terms of J .

$$J = \frac{2H}{\omega_{0m}^2} S_n \quad (2.5)$$

Inserting Equation 2.5 into Equation 2.2 yields

$$\frac{2H}{\omega_{0m}^2} S_n \frac{d\omega_m}{dt} = \tau_m - \tau_e \quad (2.6)$$

If multiplying the previous equation with ω_{0m} , it can be rewritten to Equation 2.7, noting that ω_{0m} is a constant and can be embedded in the derivative.

$$2H \frac{d}{dt} \left(\frac{\omega_m}{\omega_{0m}} \right) = \frac{\tau_m - \tau_e}{S_n / \omega_{0m}} \quad (2.7)$$

This is a convenient way of arranging the equation as ω_{0m} is the base for the rotational velocity, and S_n / ω_{0m} is the torque base. This is then converted into per-unit form where the bar indicates per-unit.

$$2H \frac{d\bar{\omega}_r}{dt} = \bar{\tau}_m - \bar{\tau}_e \quad (2.8)$$

The conversion to $\bar{\omega}_r$ in the equation above is made possible by the following equation, where ω_0 is the generator's rated electrical speed.

$$\bar{\omega}_r = \frac{\omega_r}{\omega_0} = \frac{\omega_r / p_f}{\omega_0 / p_f} = \frac{\omega_m}{\omega_{0m}} \quad (2.9)$$

Here, p_f is the number of pole pairs on the generator. To continue, the rotor angle δ is defined with respect a rotating reference synchronised to the nominal grid frequency. δ_0 is the initial angle at $t = 0$.

$$\delta = \omega_r t - \omega_0 t + \delta_0 \quad (2.10)$$

The time derivative of the angle is

$$\frac{d\delta}{dt} = \omega_r - \omega_0 = \Delta\omega_r \quad (2.11)$$

Since ω_0 is constant, the double derivative can be found to be

$$\frac{d^2\delta}{dt^2} = \frac{d\omega_r}{dt} = \frac{d(\Delta\omega_r)}{dt} \quad (2.12)$$

Using the definition of the per-unit, this can be rewritten to

$$\frac{d^2\delta}{dt^2} = \omega_0 \frac{d\bar{\omega}_r}{dt} = \omega_0 \frac{d(\Delta\bar{\omega}_r)}{dt} \quad (2.13)$$

The per-unit expression is then inserted into Equation 2.8 to give

$$\frac{2H}{\omega_0} \frac{d^2\delta}{dt^2} = \bar{\tau}_m - \bar{\tau}_e \quad (2.14)$$

In Equation 2.15, the last term is added to include damping effects, which is proportional to the speed deviation from rated speed. K_D is the damping factor in pu.

$$\frac{2H}{\omega_0} \frac{d^2\delta}{dt^2} = \bar{\tau}_m - \bar{\tau}_e - K_D \Delta\bar{\omega}_r \quad (2.15)$$

The damping factor represents, primarily, the damping effect of the damper windings in the synchronous generator. In the transient state when the rotor speed is differing from the synchronous speed, the air-gap flux will induce an emf in the opposite direction (according to Lenz law) that will try to force the generator speed back to synchronous speed [7, p. 172]. An approximate expression for the damping power can be found in [7, pp. 172-175].

Finally, the time derivative of the rotor angle, as shown in Equation 2.11, is used to substitute $\Delta\bar{\omega}_r$ to give Equation 2.16.

$$\frac{2H}{\omega_0} \frac{d^2\delta}{dt^2} = \bar{\tau}_m - \bar{\tau}_e - \frac{K_D}{\omega_r} \frac{d\delta}{dt} \quad (2.16)$$

This is known as the swing equation and describes the acceleration and deceleration of the turbine/generator set due to imbalance between mechanical and electrical torque. It can be practical to express the swing equation in terms of power instead of torques. This is done by assuming that the rotor velocity is approximately the same as the synchronous speed, such that the per-unit torque is approximately the same as the per-unit power. This is shown in Equation 2.17.

$$\frac{2H}{\omega_0} \frac{d^2\delta}{dt^2} + \frac{K_D}{\omega_0} \frac{d\delta}{dt} = \bar{P}_m - \bar{P}_e \quad (2.17)$$

2.1.2 Rate of Change of Frequency

The per-unit swing equation given in Equation 2.17 can be converted to SI-units by multiplying both sides by the nominal apparent power S_n . The resulting equation is

$$\frac{2HS_n}{\omega_0} \frac{d^2\delta}{dt^2} + S_n \frac{K_D}{\omega_0} \frac{d\delta}{dt} = P_m - P_e \quad (2.18)$$

To find the rate of change of frequency (ROCOF) the term describing the damping is neglected, assuming that the generators stay synchronised with the grid frequency during an event. Instead of looking at one generator, the focus now will be on the grid as a whole. The per-unit inertia constant, H , is then the aggregated inertia constant for the grid, including the inertia of both generators and motors. The power difference is now the difference between the total produced and consumed power in the grid.

$$\frac{2HS}{\omega_0} \frac{d^2\delta}{dt^2} = P_{prod} - P_{cons} \quad (2.19)$$

Here S is the total rated apparent power in the grid. By looking at Equation 2.3, it can be seen that $H \cdot S$ is the total kinetic energy in the power system. For the next step, the angular position is converted to the angular velocity.

$$\frac{d\omega}{dt} = \frac{1}{2}\omega_0 \left(\frac{P_{prod} - P_{cons}}{S \cdot H} \right) \quad (2.20)$$

By using that $\omega = 2\pi f$ it is found that

$$\frac{d(2\pi f)}{dt} = \frac{1}{2}2\pi f_0 \left(\frac{P_{prod} - P_{cons}}{S \cdot H} \right) \quad (2.21)$$

Finally, the equation describing the initial rate of change of frequency after a disturbance in the electric power grid is found, as shown in Equation 2.22 [12, p. 422].

$$\frac{df}{dt} = \frac{1}{2}f_0 \frac{P_{prod} - P_{cons}}{S \cdot H} \quad (2.22)$$

It has been shown that the initial ROCOF is linearly proportional to the difference in power. A surplus in power produced gives a positive derivative frequency. Similarly, a deficiency in

power gives a negative derivative. The frequency response is also inversely proportional to the cumulative kinetic energy in the grid, which linearly depends on the total system inertia. As a consequence, it is seen that the inertia tries to resist any speed changes. Large system inertia is therefore beneficial for the stability of the electric power grid frequency.

2.1.3 Frequency Control

Typical frequency response for the loss of a large generating unit is shown in Figure 2.2. The same development would be seen for a loss of a large power-consuming unit, but the frequency would rise instead. The response after a large disturbance is often divided into four stages. These stages are shortly described here based on the description given in [7, pp. 350 - 363]. The focus in this thesis is on the initial frequency drop and the primary control.

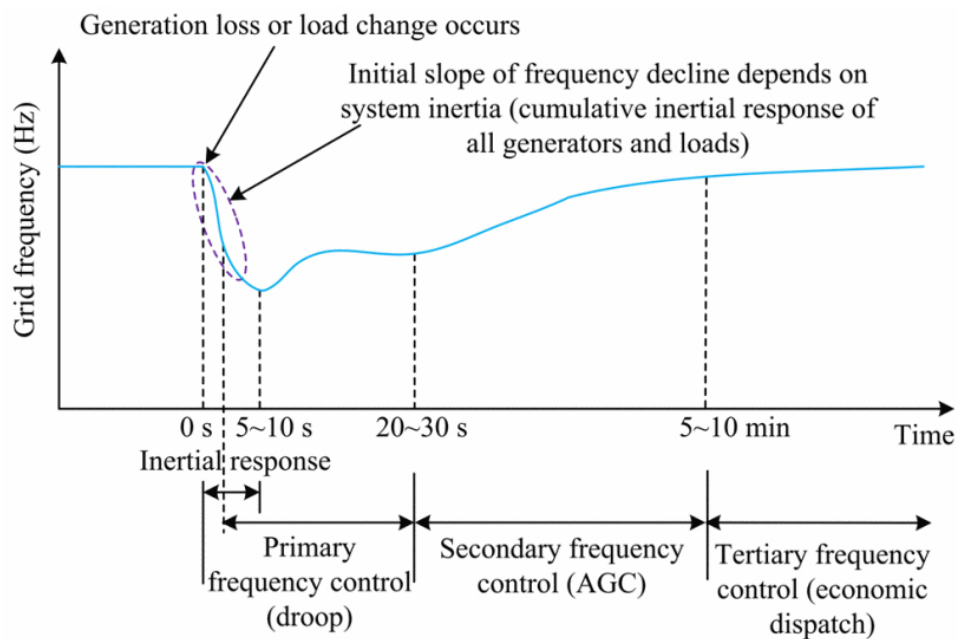


Figure 2.2: Frequency response of a loss of a large generator [13].

Stage 1: Rotor swings in generators (inertial response)

In the first few seconds, rotor swings in the generators will occur. If the rotor swings are too large and have poor damping, the system can lose synchronism.

Stage 2: Frequency drop

The imbalance in active power will decelerate the generators. The frequency's initial slope is determined by the system inertia, as described in Equation 2.22.

Stage 3: Primary control

The turbine governors start reacting and will increase the active power output. This stabilises the frequency at a new steady-state due to the droop. The point where the frequency reaches the bottom point of the curve is called frequency nadir.

Stage 4: Secondary control

The automatic generation control starts reducing the area control error to zero, returning the

frequency to its nominal value. This stage has a time scale of minutes.

2.2 Variable Speed Hydro Power

2.2.1 Different Technologies for Variable Speed Hydro Power

Subchapter 2.2.1 is, with small modifications, copied from the preliminary specialisation project [6].

Two different technologies are used in variable-speed hydropower. These are the Doubly Fed Induction Machine (DFIM) and the Converter Fed Synchronous Machine (CFSM). A third historical alternative exists, and that is the pole changing synchronous machine that can alternate between two different speeds, this alternative is not discussed in this report as it is deemed obsolete due to limited speed variations and its heavy construction [3]. The single-line diagrams for the two systems are shown in Figure 2.3. As seen in the figure, the stator terminals of the DFIM is directly connected to the grid while the rotor terminals are connected with a back-to-back converter through a set of slip rings. The rotor is consuming considerably less power than the stator, typically 15 % of rated power. To allow for low voltage ride through capabilities, the converter for the DFIM can be designed for about 30 % of rated power [14]. Adjustable speed drive is enabled by varying the slip frequency of the rotor. The DFIM solution has been the most utilised of the two technologies in existing variable-speed pumped hydro. This is mainly due to the smaller and cheaper converter for the DFIM compared to the CFSM [3].

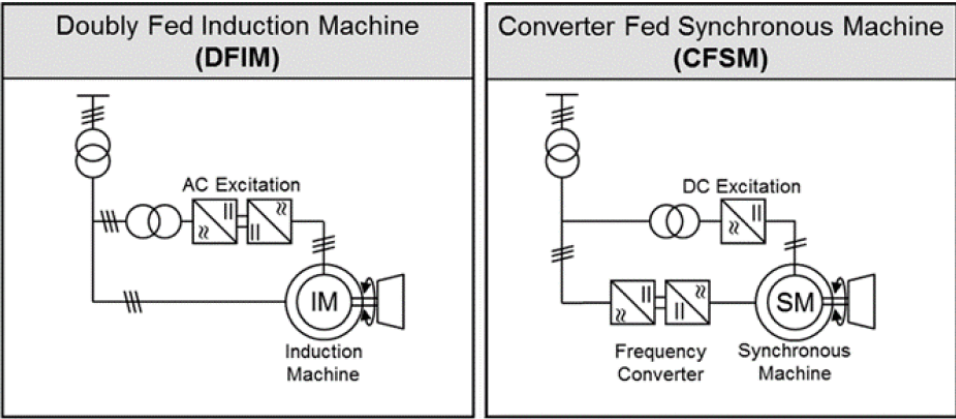


Figure 2.3: Single-line diagram of the DFIM and the CFSM [14].

For the CFSM the back-to-back converter is connected directly to the stator, fully decoupling the synchronous machine from the grid. As a result, the converter must be rated for the full power of the machine. This limits the maximum capacity of the CFSM. Today the maximum viable power for a CFSM is 100 MW, but this is expected to increase as improvements are made to the semiconductor converters [15]. [14] claims that with the modular multi-level converter (MMC), it is possible to improve the converter’s efficiency and increase the rated power up to 500 MW.

2.2.2 Potential Benefits of Variable Speed Hydro Power

Variable speed hydropower provides several potential benefits compared to fixed speed operation. In a pumped hydropower plant, an important aspect is the ability to adjust the active power consumption during pumping mode. In a conventional pumped power plant, the active power can be adjusted in generator mode with the governor, but the pumping power is fixed. The ability to adjust power consumption during pumping mode gives the VSHP improved ability to contribute to frequency regulation. For a variable speed power plant, the active power can be controlled by the converter instead of the governor as in the conventional system. This gives the possibility of faster power dynamics as the electrical machine's kinetic energy can be used to inject power instantly [3]. The increased flexibility can help integrate a higher share

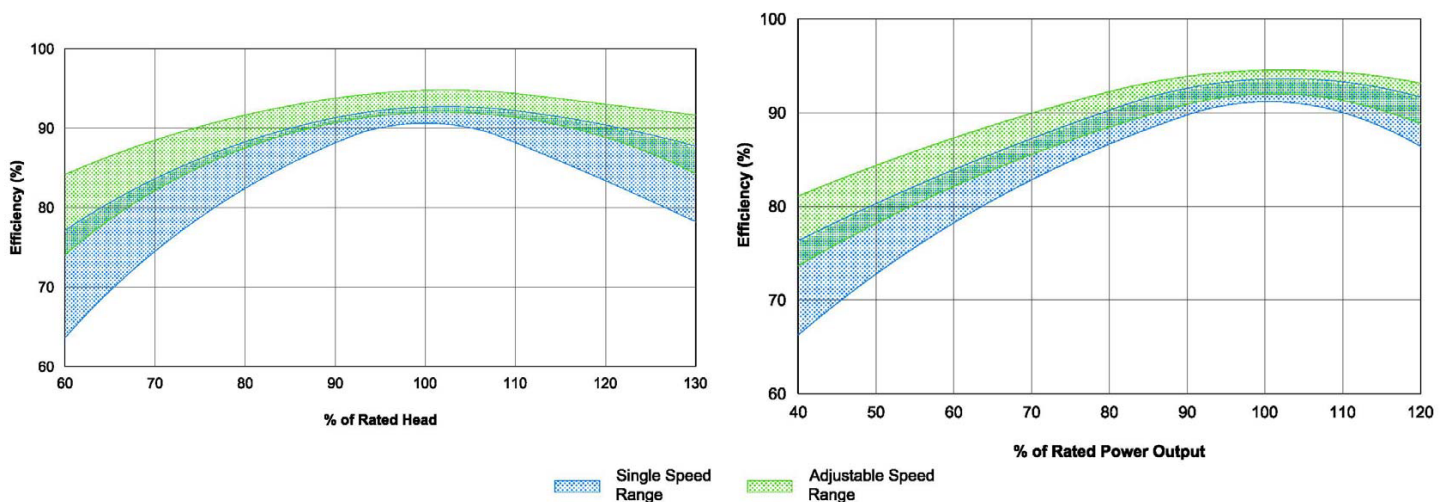


Figure 2.4: Typical efficiency for variations in head and power output for a single speed and variable speed turbine [16].

of intermittent renewable energy to the grid [3]. Another benefit for VSHP is the ability to increase the efficiency over a large span of active power output and head [16]. This is illustrated in Figure 2.4. However, it must also be considered that with VSHP the converters necessary to obtain variable speed will cause additional losses. Consequently, the increase in efficiency of the electrical machine must be larger than the converter's losses to get a net positive effect. The lifetime of VHSP can also be increased by adjusting the speed in correlation with the head and the power output to limit situations where cavitation and vibrations cause wear and tear on the turbine [3].

2.3 Virtual Inertia

2.3.1 Virtual Inertia by Supplementary Control

Several different methods of generating synthetic inertia exists. Some of these are shown in Figure 2.5. In 2.5a, the method using the derivative of the frequency is shown. This method includes a low pass filter to mitigate the issues by differentiating a noisy signal. In addition to this, there is a washout filter (high pass) to ensure the inertia control is only acting in transient periods, leaving the steady-state unaffected [9]. Another way of emulating inertia is to use a

proportional controller based on the the frequency deviation, similarly to ordinary droop control [9, 17]. An example of this is shown in Figure 2.5b. A third way of supplying inertia is to utilise a triggered frequency deviation method, as shown in Figure 2.5c. Here the inertia power can be based on the frequency derivative like in Figure 2.5a or the frequency deviation like in Figure 2.5b. This method is similar to what is called fast frequency response which has been tested by the Norwegian TSO in [18].

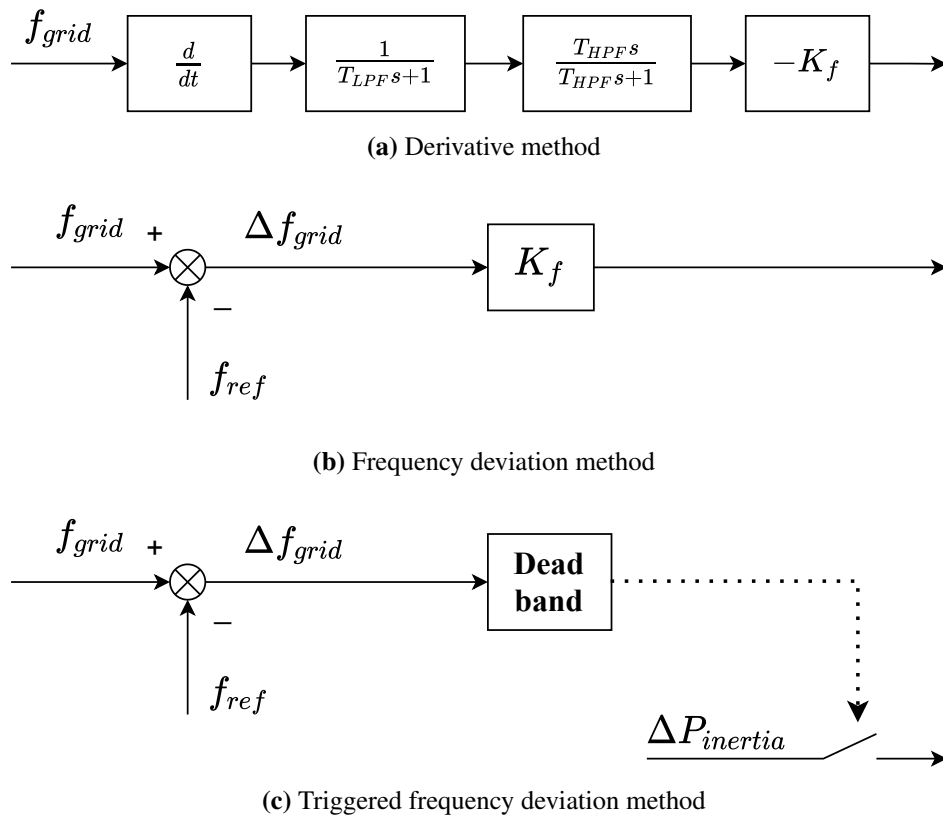


Figure 2.5: Several supplementary inertia control methods [9].

2.3.2 Virtual Synchronous Machine (VSM)

Another way of providing virtual inertia is through the concept of a virtual synchronous machine (VSM). This was first proposed by Beck and Hesse [19] under the name VISMA. The idea is to simulate the synchronous machine in the control system in real-time based on the equations describing the synchronous machine and measurements. These calculations are sent as references to the converter, making the converter emulate the given synchronous machine's behaviour. As the synchronous machine is a virtual machine, it does not necessarily have to represent a realistic machine, meaning that the parameters can be tuned to give the desired response [20]. There are many different ways of implementing a VSM. The various algorithms can be roughly classified into two categories, and these are high-order and low-order, depending on the order of the differential equation used to represent the synchronous machine [21]. The full order equation is of order seven, including the fifth-order electrical equation and second-order mechanical equation [20]. The simplest form of VSM can be said to be frequency droop control. As shown in [22] frequency control droop is equivalent to a VSM model based on the

swing equation if the droop control includes a low-pass filter. The equivalence between the droop control and VSM is expressed in Equation 2.23.

$$T_a = T_f \frac{1}{m_p}, \quad K_D = \frac{1}{m_p} \quad (2.23)$$

Here T_a is the mechanical starting time constant for the generator as defined in Equation 2.4 and T_f is the low-pass filter constant. K_D is the damping torque coefficient and m_p the droop gain. To provide virtual inertia, it is sufficient to implement the swing equation as developed in subsection 2.1.1. A block diagram showing an implementation of the swing equation is presented in Figure 2.6.

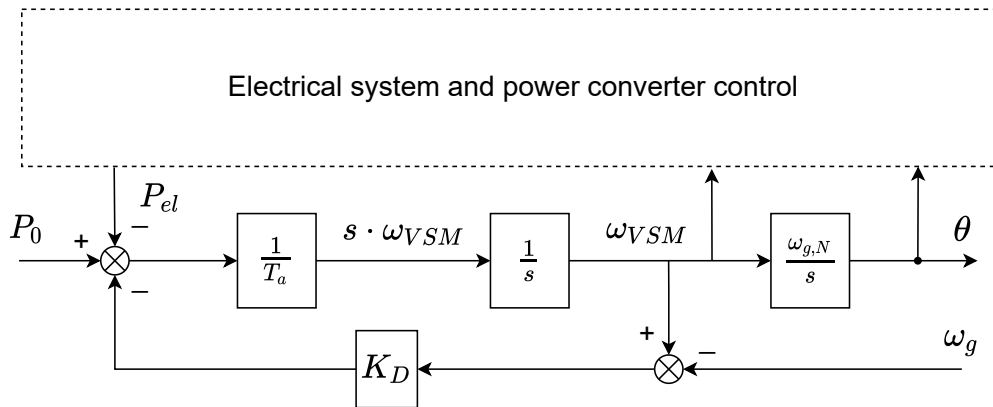


Figure 2.6: Virtual inertia based on the swing equation [22].

2.4 Modelling of the Salient-Pole Synchronous Machine

The salient-pole machine is commonly used for low-speed applications like hydropower. In this subchapter, an introduction to salient-pole machines is given, and the equivalent circuit is established based on the subchapters concerning the salient-pole machine in [23, pp. 571 - 591] and [7, pp. 83 - 89]. This section assumes the reader has basic knowledge of the round-rotor synchronous machine. This description only considers the machine's steady-state operation, for an explanation of the electromagnetic phenomena, see Chapter 4 in [7].

A simplified model of a salient-pole synchronous machine with two poles is shown in Figure 2.7. Contrary to the round-rotor machine the salient-pole machine does not have uniform magnetic permeance along the rotor, as the air gap varies. The two-reaction model is used to model the salient-pole where the vectors for the magnetomotive forces (mmf) can be resolved into two axes. These two axes have constant permeance and are called the direct axis (d -axis) and the quadrature axis (q -axis). As shown in Figure 2.7, the d -axis is aligned with the field pole axis and is centred in the magnetic north pole, while the q -axis is (in this example) lagging 90° . The q -axis can be chosen to lead or lag the d -axis, and both definitions are used in the literature [10, p. 53]. The rotor position in relation to the stator is given by angle ψ and is defined as the difference between axis of phase a and the d -axis.

It can be seen that the armature reaction mmf, \vec{F}_a , will vary based on the position of the rotor as the permeance is dependent on rotor position. Under the assumption of linear magnetic circuits,

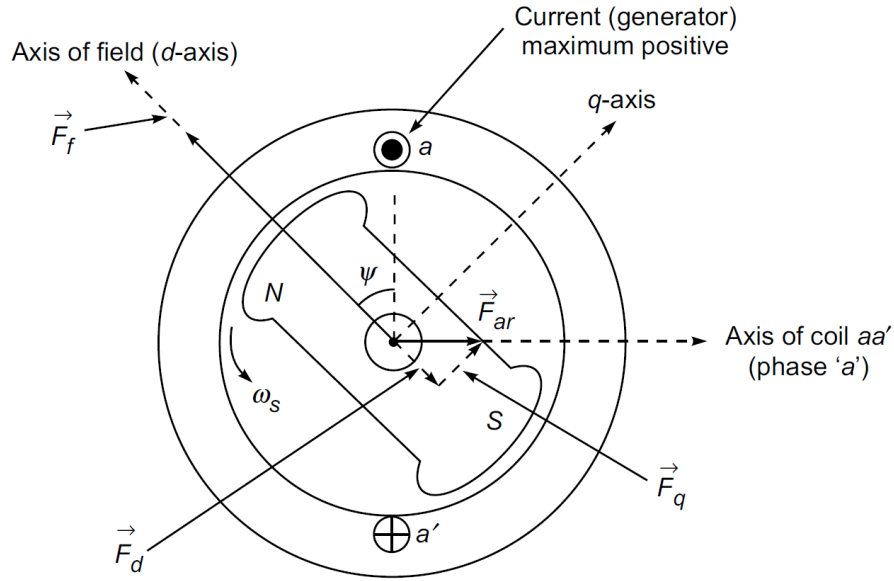


Figure 2.7: Simplified model of a salient-pole synchronous machine [23, p. 576].

the armature reaction can be resolved into d - and q -components, \vec{F}_d and \vec{F}_q . It is then possible to define the armature reaction's flux components, as shown in Equation 2.24a and 2.24b [23, p. 577].

$$\Phi_d = \mathcal{P}_d \mathbf{F}_d = \mathcal{P} K_{ar} \mathbf{I}_d \quad (2.24a)$$

$$\Phi_q = \mathcal{P}_q \mathbf{F}_q = \mathcal{P} K_{ar} \mathbf{I}_q \quad (2.24b)$$

Where \mathcal{P} is the permeance, and K_{ar} is a proportionality constant for the armature winding. \mathbf{I}_d and \mathbf{I}_q are the d - and q -component of the armature current. It should be noted that $\mathcal{P}_d > \mathcal{P}_q$ because the air gap along the q -axis is greater, yielding a greater resistance to the magnetic flux. With the fluxes defined, it is possible to find the emfs induced.

$$\mathbf{E}_d = -j K_e \Phi_d \quad (2.25a)$$

$$\mathbf{E}_q = -j K_e \Phi_q \quad (2.25b)$$

Here, K_e is a proportional constant of the armature winding. One can find the resultant induced emf with Equation 2.26.

$$\mathbf{E}_r = \mathbf{E}_f + \mathbf{E}_d + \mathbf{E}_q \quad (2.26)$$

The next step is to define the reactances for the d - and q -axes.

$$x_d^{ar} = K_e \mathcal{P}_d K_{ar} \quad (2.27a)$$

$$x_q^{ar} = K_e \mathcal{P}_q K_{ar} \quad (2.27b)$$

Combining Equations 2.24, 2.25, 2.26 and 2.27 the following is found.

$$\mathbf{E}_f = \mathbf{E}_r + j x_d^{ar} \mathbf{I}_d + j x_q^{ar} \mathbf{I}_q \quad (2.28)$$

For a realistic synchronous machine with armature resistance, R_a , and leakage reactance, x_l , the resultant air-gap emf is shown in Equation 2.29.

$$\mathbf{E}_r = \mathbf{V}_t + R_a \mathbf{I}_a + jx_l \mathbf{I}_a \quad (2.29)$$

Where $\mathbf{I}_a = \mathbf{I}_d + \mathbf{I}_q$. Equation 2.28 can be used together with Equation 2.29 to find the induced emf in a salient-pole machine as shown below.

$$\mathbf{E}_f = \mathbf{V}_t + R_a \mathbf{I}_a + j(x_d^{ar} + x_l) \mathbf{I}_d + j(x_q^{ar} + x_l) \mathbf{I}_q \quad (2.30)$$

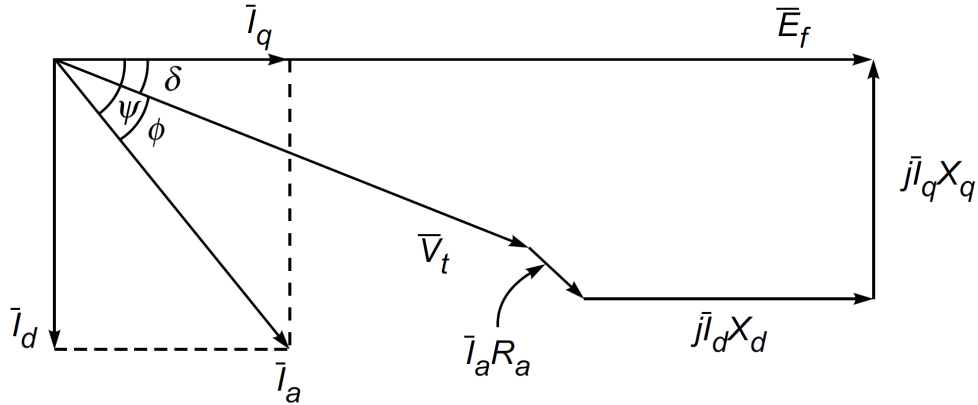


Figure 2.8: Phasor diagram of an overexcited salient-pole machine in generating mode [23, p. 578].

For convenience, the d and q reactances are defined to include the leakage reactance, which gives the following equation.

$$\mathbf{E}_f = \mathbf{V}_t + R_a \mathbf{I}_a + jx_d \mathbf{I}_d + jx_q \mathbf{I}_q \quad (2.31)$$

Equation 2.31 shows the final expression for the salient-pole emf, including d and q reactances. The phasor diagram for this equation is seen in Figure 2.8. To use this equation for practical purposes, one has to first identify the q -axis by determining \mathbf{E}_f . However, to find \mathbf{E}_f , the d - and q -components of the currents have to be known. These can not be found without first having determined the q -axis. For this reason, Equation 2.31 is rewritten to Equation 2.32 [7, p. 86].

$$\mathbf{E}_f = \mathbf{V}_t + R_a \mathbf{I}_a + jx_q \mathbf{I}_a + j(x_d - x_q) \mathbf{I}_d \quad (2.32)$$

This can also be written as

$$\mathbf{E}_f = \mathbf{E}_Q + j(x_d - x_q) \mathbf{I}_d \quad (2.33)$$

Where

$$\mathbf{E}_Q = \mathbf{V}_t + (R_a + jx_q) \mathbf{I}_a \quad (2.34)$$

With this equation it is possible to determine the angle of the q -axis in relation to the measured terminal voltage, \mathbf{V}_t , and the armature current, \mathbf{I}_a , if R_a and x_q are known. As the product $j\mathbf{I}_d(x_d - x_q)$ lies in the same direction as the q -axis and \mathbf{E}_f by definition is oriented along the q -axis, the voltage \mathbf{E}_Q must also be on the q -axis. The complete phasor diagram is shown in Figure 2.9.

Finally, the equivalent circuit diagram for the salient-pole machine is shown in Figure 2.10.

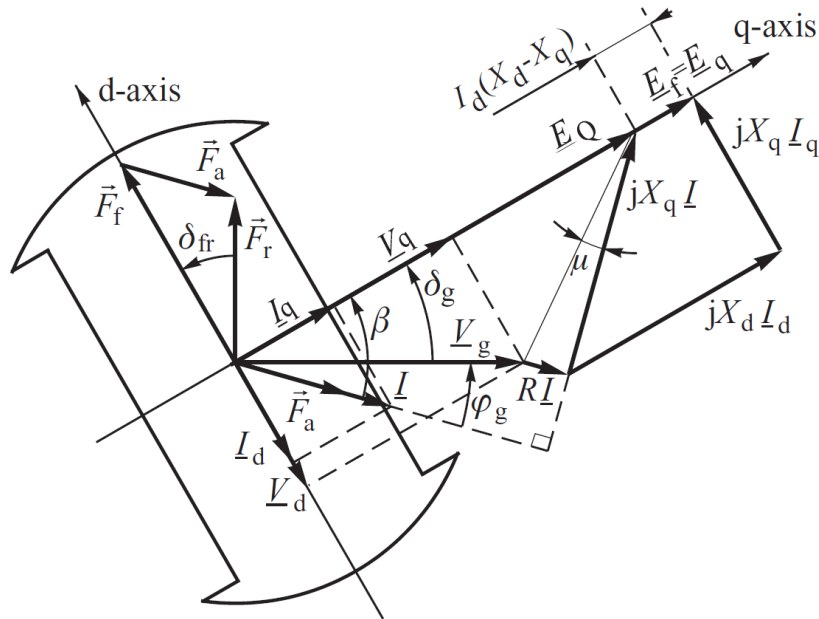


Figure 2.9: Complete phasor diagram for an overexcited salient-pole machine in generator mode [7, p. 86].

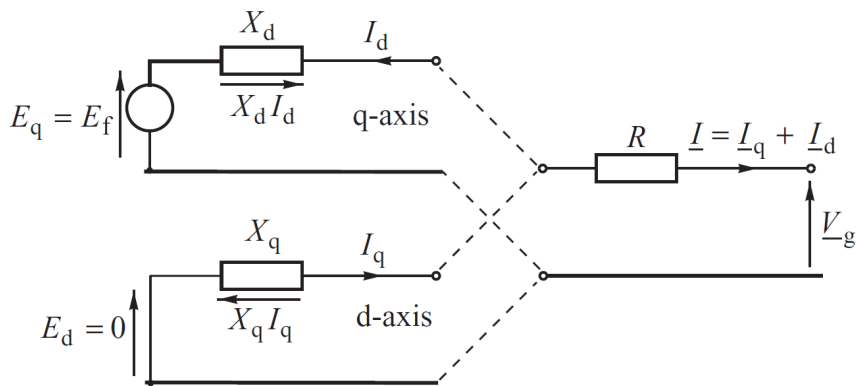


Figure 2.10: The equivalent circuit diagram for the salient-pole machine in steady-state [7, p. 87].

2.5 Parameter Estimation for the Salient-Pole Machine

It is possible to perform different kinds of tests to estimate the parameters of a salient-pole machine. Due to the old age of the Siemens-Schuckert synchronous generator used in the laboratory set-up in this thesis, the traditional short circuit test was deemed too hazardous [24]. August Jaros has attempted to estimate the synchronous machine's parameters in his master thesis [25] with the standstill frequency response. However, the results were inconclusive due to the laboratory measurement equipment was lacking the frequency bandwidth capabilities necessary for such a test. In this subchapter the theory for a test procedure based on load shedding will be explained. This procedure is suitable for estimating the standard parameters of the synchronous generator. The standard parameters that can be estimated with the theory presented here are x_d , x'_d , x''_d , x_q , x''_q , T'_{do} , T''_{do} and T''_{qo} . It is also possible to calculate the

short-circuit time constants T'_d , T''_d and T''_q based on the estimated variables. The only electrical standard parameter not estimated is the leakage reactance, x_l , suitable values for this parameter are discussed in Chapter 6.4.

2.5.1 d -axis Parameters

If the generator is connected to the grid supplying or consuming reactive power and deliver zero active power, the armature current will be in the d -axis with no q -axis component. The unsaturated reactance can be obtained by having the machine in underexcited operation as this will avoid saturating the iron core. With zero active power and negative reactive power (capacitive load), the current will lead the voltage by 90° . As the generator runs in no-load, the load angle will be zero and the terminal voltage will be in phase with the inner voltage. This is shown in the phasor diagram in Figure 2.11, for simplicity the armature resistance has been assumed to be zero in this diagram.

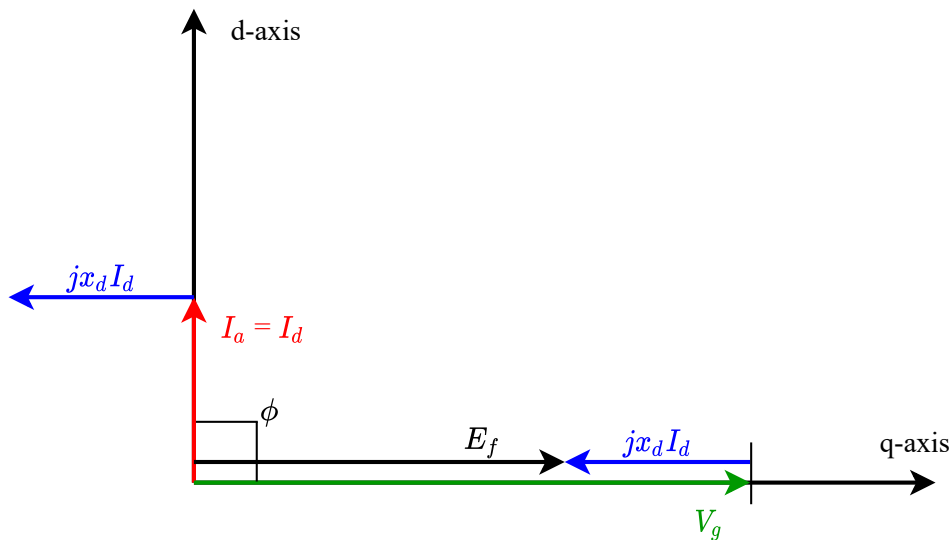


Figure 2.11: Phasor diagram of the initial conditions for d -axis load rejection scenario, underexcited generator.

When having the desired operating condition, the test is performed by disconnecting the generator from the grid and recording the terminal voltage and the field current. The supply of mechanical power must be disconnected simultaneously as the generator, to avoid the governor or speed regulator influencing the resulting terminal voltage. An assumption for the following estimation method to be valid is that the generator's speed remains approximately constant for the period needed to record the subtransient and transient voltages. Typical development of the terminal voltage and the field current during a load shedding event with the initial conditions as explained above is presented in Figure 2.12 and 2.13. With Equations 2.35, 2.36 and 2.37, the d -axis reactances can be estimated [26, 27]. In these equations the constants A, B and C refer to the difference between the initial voltage (before the load is disconnected) and the initial subtransient, transient and steady-state voltage respectively. This can be seen in Figure 2.12. The current i_0 is the initial armature current, assuming that the current has no q -axis component.

$$x_d = \frac{C}{i_0} \tag{2.35}$$

$$x'_d = \frac{B}{i_0} \tag{2.36}$$

$$x''_d = \frac{A}{i_0} \tag{2.37}$$

The transient and subtransient open-circuit time constants, T'_{do} and T''_{do} , can be found by reading the times where the voltage or the field current has fallen 63.8% from its initial value as according to the definition of the time constants.

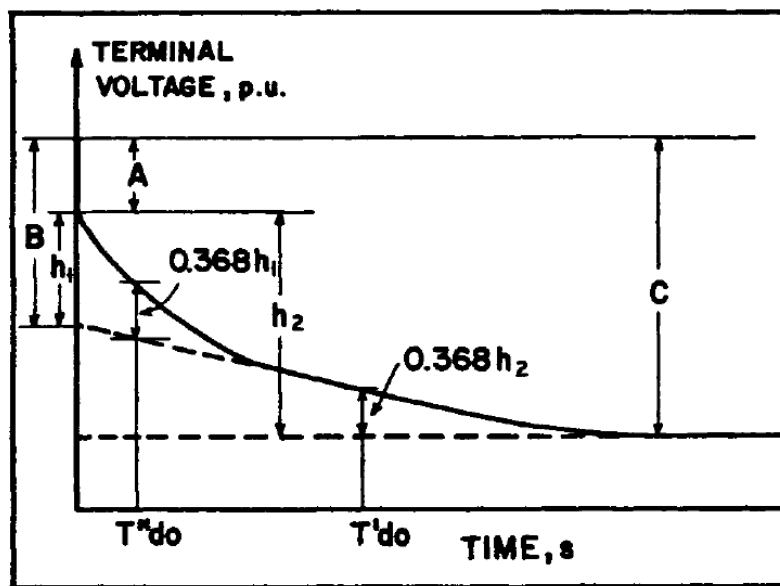


Figure 2.12: Transient development of the terminal voltage after load rejection of purely reactive load, d -axis load rejection scenario [26].

2.5.2 q -axis Parameters

The estimation of the q -axis parameters is a bit more complicated than for the d -axis parameters. Several methods exist to estimate the q -axis parameters utilising load rejection tests. In the following, the q -axis and the arbitrary load rejection test is described.

q -axis Load Rejection Test

One way of estimating the q -axis parameters is to ensure that the armature current is oriented in the q -axis. This can be done by using a rotary encoder to measure the rotor's mechanical position and estimate the power angle δ . Knowing the power angle, it is possible to find a load condition where this angle is equal to the phase angle ϕ [27]. A phasor diagram depicting this scenario is presented in Figure 2.14 if these two angles are identical, the armature current will be oriented in the q -axis.

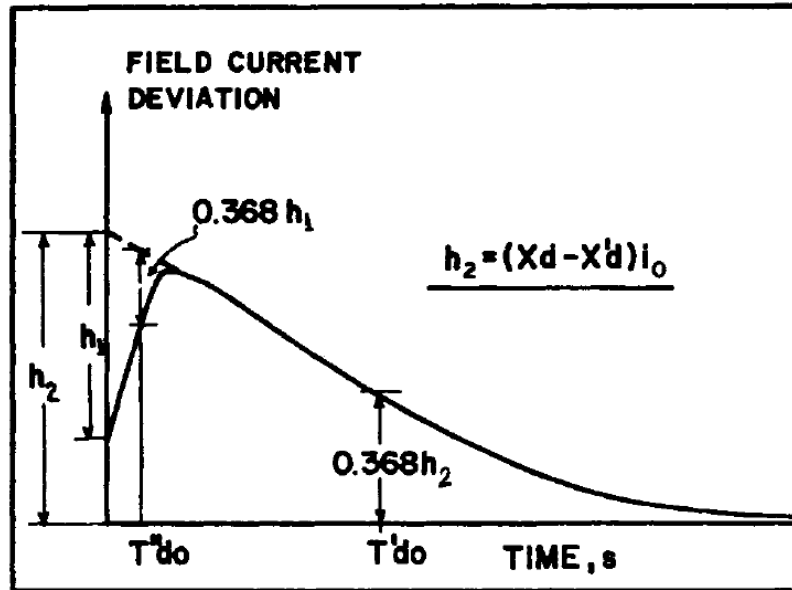


Figure 2.13: Transient development of the field current after load rejection of purely reactive load, d -axis load rejection scenario [26].

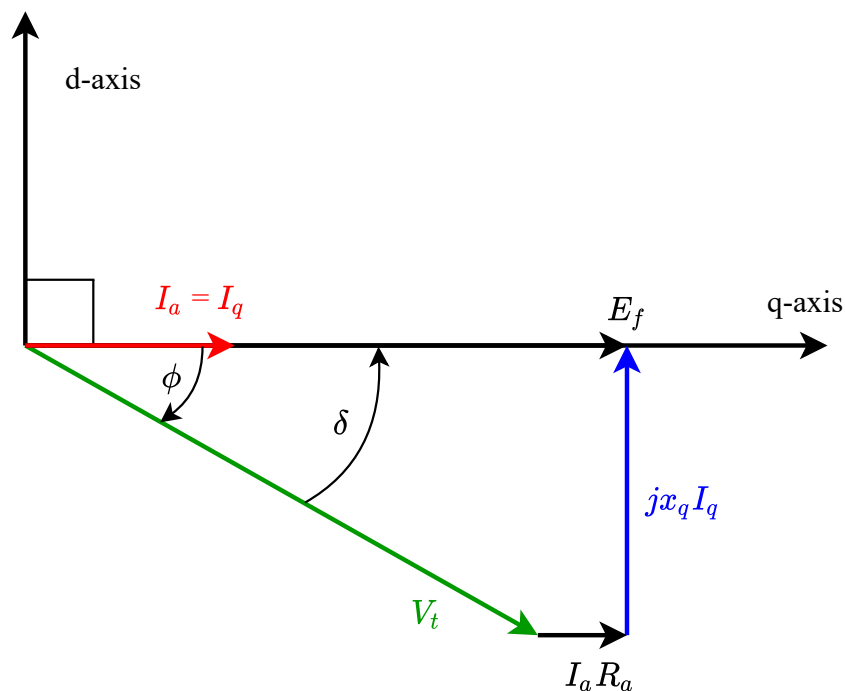


Figure 2.14: Phasor diagram of the initial conditions for q -axis load rejection scenario, underexcited generator.

This test allows for the estimation of the subtransient and steady-state q -axis reactances. Similarly to the d -axis, the subtransient reactance is found by looking at the development of the terminal voltage, as shown in Figure 2.15. The expression for the steady-state q -axis reactance is presented in Equation 2.38, and the subtransient reactance is shown in Equation 2.39 [26]. For the transient period, there is no screening effect in the q -axis for the salient-pole machine

and the transient reactance is equal to the steady-state reactance [7, p. 138].

$$x_q = \frac{\sqrt{A^2 - C^2}}{I_{q0}} \quad (2.38)$$

$$x_q'' = \frac{\sqrt{A^2 - C^2} - \sqrt{B^2 - C^2}}{I_{q0}} \quad (2.39)$$

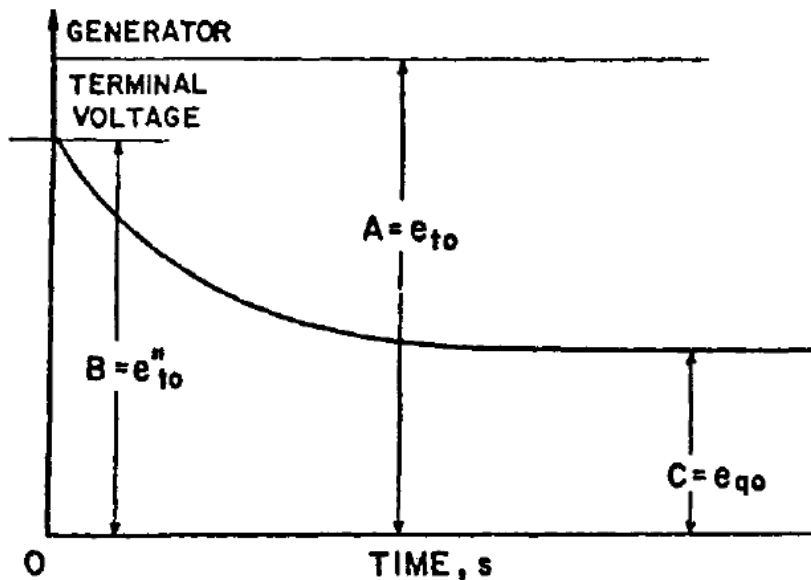


Figure 2.15: Transient development of the field current after load rejection of reactive load, q -axis [26].

No Load Angle Measurement

If a measurement of the load angle is not available, there is another method to obtain the loading condition presented in Figure 2.14. This is done by performing several load rejections while monitoring the field current. The goal is to find the operating point with as small transient deviations in the field current as possible [26]. Theoretically, this operating point will give an armature current in the q -axis. This can be explained by looking at Figure 2.9. If the armature current is aligned with the q -axis, the armature reaction mmf will be perpendicular to the d -axis and not affect the field mmf.

Arbitrary Axis Load Rejection Test

An alternative way to estimate the q -axis parameters is the arbitrary axis load rejection test. With this test, it is possible to estimate the steady-state and subtransient q -axis reactance and the q -axis subtransient open-circuit time constant [27]. Here it is necessary to monitor and record the load angle and the terminal voltage. As for the other tests, the generator is synchronised to the electric grid and suddenly disconnected with an initial load condition. The only criteria for the initial loading in this test is that the current has both d -axis and q -axis components before disconnection [28, as cited in 27].

$$x_q = \frac{(V_t \cdot \sin\delta)_0}{I_{q0}} \quad (2.40)$$

$$x_q'' = x_q - \frac{(V_t \cdot \sin\delta)''_0}{I_{q0}} \quad (2.41)$$

To estimate the parameters, the d -axis voltage curve and the initial q -axis current needs to be recorded. Equations 2.40 and 2.41 are then used to calculate the values for the reactances. A trend line of the subtransient voltage curve is drawn to find the initial subtransient d -axis voltage, and the voltage value is read from where this trend line meets the y-axis. An example of the d -axis voltage during an arbitrary load rejection test is presented in Figure 2.16. It should be noted that the voltage is plotted on a semi-logarithmic graph. In this example, it is also shown how to read the q -axis open-circuit subtransient time constant. The time constant is defined as the time it takes from the generator is disconnected until the d -axis voltage has dropped to a value of 36.8 % of the initial subtransient voltage.

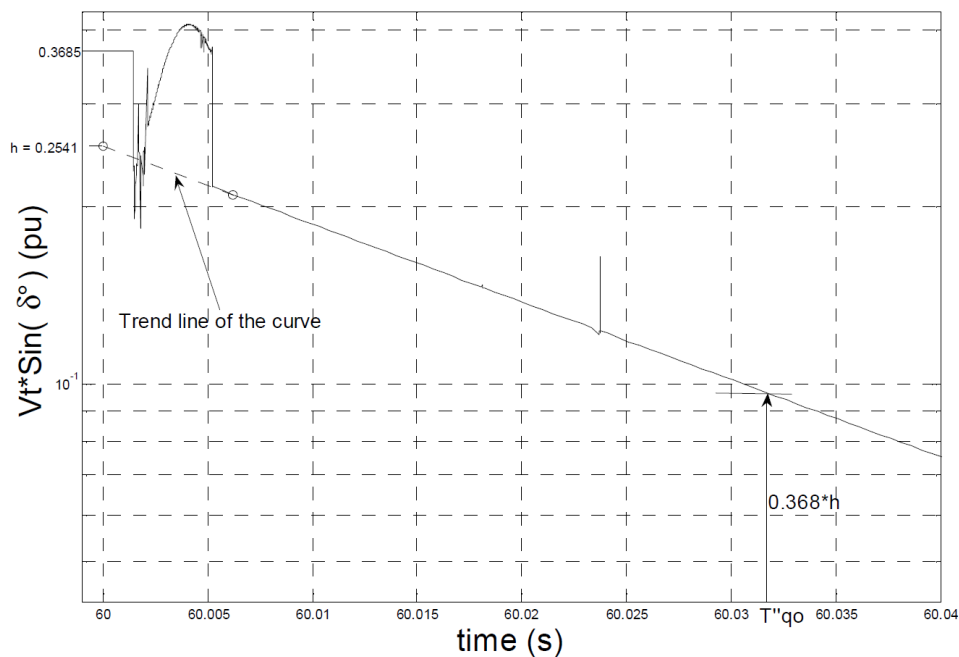


Figure 2.16: An example of the d -axis voltage curve during an arbitrary axis load rejection [27].

Laboratory Set-Up and Equipment

3.1 Description of Laboratory Set-Up for Virtual Inertia Experiments

In the following section, a description of the laboratory set-up used for virtual inertia experiments is given. An overview of the proposed system is shown in Figure 3.1. A converter-fed synchronous machine as described in Chapter 2.2.1 is approximated with one VSC supplied by a DC voltage source. This is done because these experiments focus on the interface between the grid and the converter and the virtual inertia capabilities. The VSC is controlled as a conventional grid-connected PLL-synchronised converter with PQ-control and a supplementary virtual inertia control loop. A one to one ratio transformer is used for galvanic isolation and limits the harmonics produced from the converter. A series inductance is used to represent a line connecting the power plant to the grid, and a parallel ohmic resistance is used as a local load to introduce active power disturbances. The synchronous generator on the right side represents

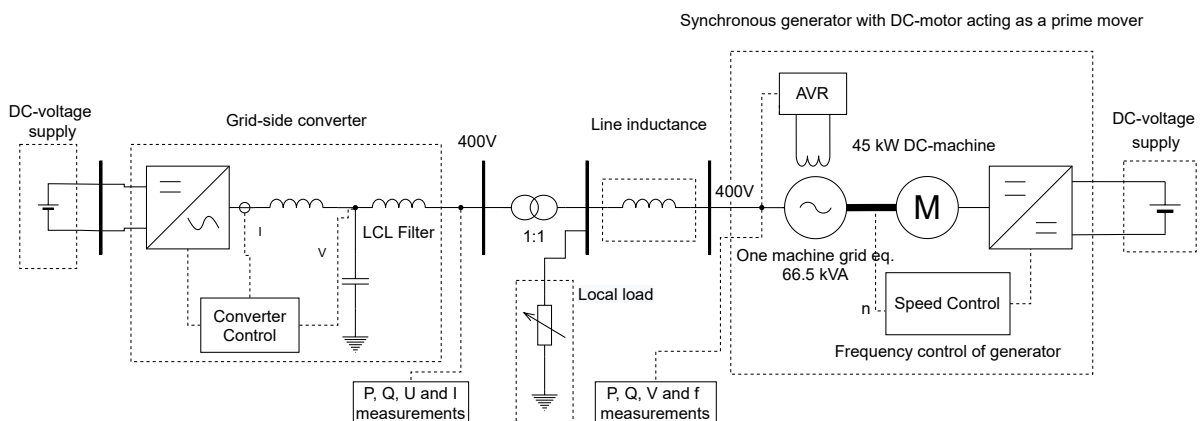


Figure 3.1: Overview of the laboratory set-up used for IE experiments.

a single-machine equivalent of a weak electrical grid. A speed controller is used to act as a governor for this generator. The speed controller has a droop and has been tuned to get a slow response to allow for frequency dynamics when applying load perturbations. The control of the synchronous generator's field current is done with the digital excitation control unit Basler DECS-250N. This unit has an AVR functionality that was utilised for the control of voltage in

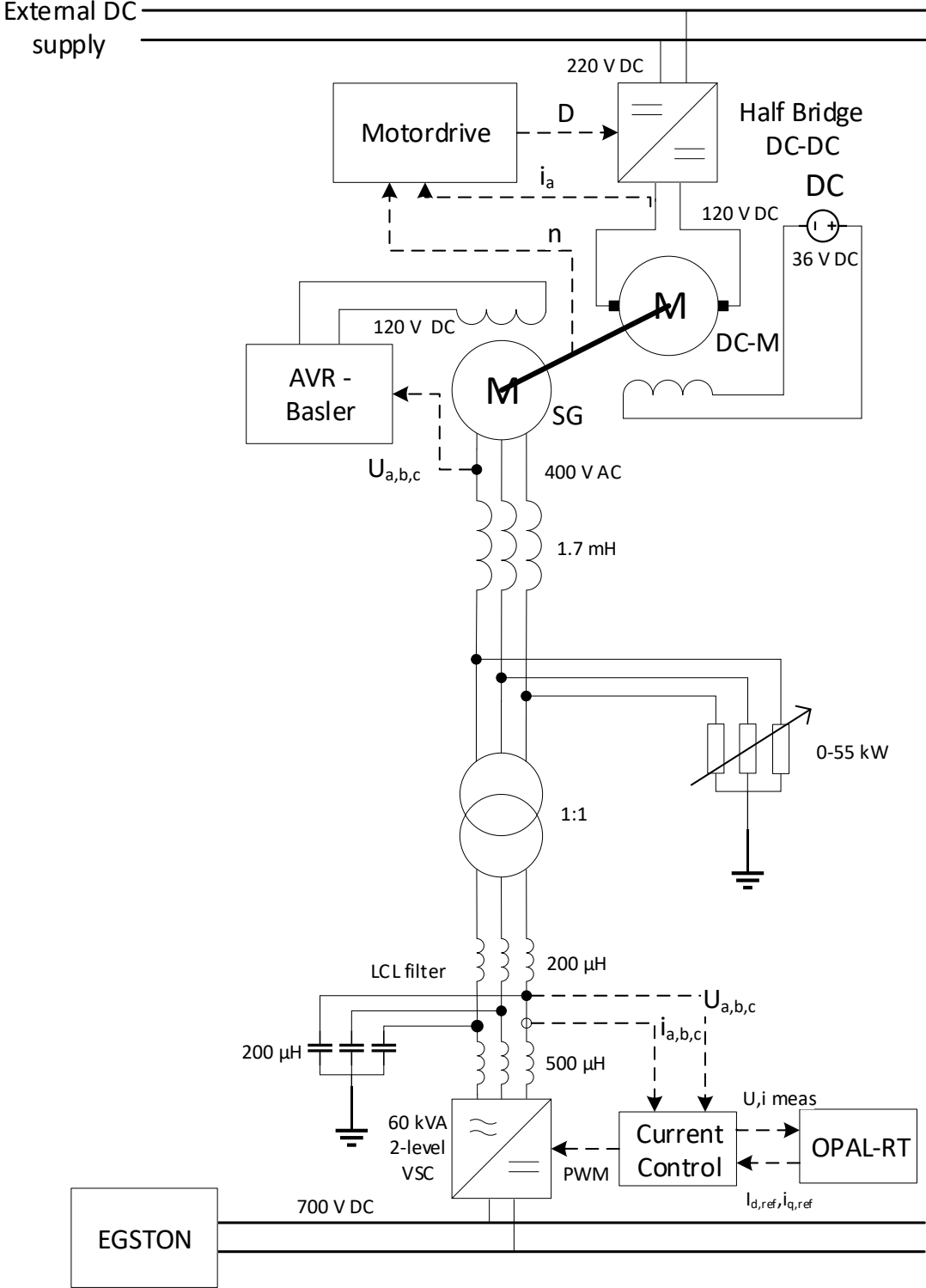


Figure 3.2: Circuit diagram of the laboratory setup

the laboratory set-up. The main components used in the virtual inertia experiments are listed in Table 3.1.

Table 3.1: List of the Main Components for the Virtual Inertia Experiment as Presented in Figure 3.2.

| NTNU No. | Component | Type and Producer |
|-----------------------|--|-------------------|
| A02-0035 | Synchronous generator 75 kVA | Siemens-Schuckert |
| A01-0136 | Separately excited DC-motor 45 kW | Siemens-Schuckert |
| A02-0035 ¹ | DC-motor control system [29, 30] | SINTEF Energy |
| A02-0035 | 40 kW DC-DC half bridge converter | SINTEF/NTNU |
| A02-0035 | Excitation control for synchronous generator | DECS-250N, Basler |
| K02-0137 | 1.7 mH 3 phase inductance | SIEMENS |
| K01-0505 | Water-cooled load resistance 55 kW | NTNU |
| B01-0992 | 400:400 70 kVA D/Y transformer | Lubecke |
| B03-0431 | 60 kVA 2-level VSC [31, 32] | SINTEF Energy |
| B03-0552 | 200 kVA power amplifier | CSU 100, Egston |
| P15-0001 | Real-time simulator | OPAL-RT, OP5600 |

The measurement equipment is listed in Table 3.2. The speed of the generator/motor set is recorded by the rotatory encoder and accessed through the DC-motor control system. The active and reactive power on the generator side is measured with the two-watt meter method on the PicoZed-based processor based on the currents and voltages measured by the LEM sensors. The mixed signal oscilloscope is used for logging of the measurements on the generator side. The active and reactive power on the converter side is measured by the internal control system on the VSC and accessed on the client computer used to together with OPAL-RT real-time simulator. The Fluke multimeter is used as a general-purpose measurement tool during the experiments. The DEIF multi-instrument is installed in the control cabinet for the motor/generator set and has been used to read the generator's initial loading.

Table 3.2: List of Equipment Used for Measurements in the Virtual Inertia Experiments.

| NTNU No. | Component | Type and Producer |
|----------|---------------------------------|---------------------|
| G04-0365 | Mixed signal oscilloscope | MSO 3014, Tektronix |
| A01-0136 | Rotary Encoder | ROD 42, Heidenhain |
| S03-0439 | Multimeter | 175 True RMS, Fluke |
| A01-0136 | Multi-instrument | MIC-2 MKII, DEIF |
| A01-0136 | Current transducer | HAL 200-S, LEM |
| A01-0136 | Voltage transducer | LV 25-600, LEM |
| B03-0431 | 60 kVA 2-level VSC. No.2 | SINTEF Energy |
| A01-0136 | PicoZed-based processor[31, 32] | SINTEF Energy |

A more detailed circuit diagram of the proposed laboratory set-up is shown in Figure 3.2. A third schematic is included in Appendix D.5, Figure D.5 depicting how the laboratory set-

¹The integrated components of the control cabinet for the motor/generator set do not have individual lab. No. The No. for the control cabinet have been used instead.

up is connected in the laboratory. An overview and a single-line schematic of the smart grid laboratory is included in Appendix D.6 and D.7.

3.2 Description of Laboratory Set-Up for Parameter Estimation Experiments

A description of the laboratory set-up used to estimate the synchronous generator's standard electrical parameters is given in the following. A single-line schematic of the laboratory set-up's main components for the parameter estimation experiments is depicted in Figure 3.3. The list of equipment for this set-up is presented in Table 3.3. The same motor/generator set as used for the virtual inertia experiments is utilised here. The Basler AVR has been exchanged with a DC-voltage supply to keep the field voltage constant during the experiments. In the experiments, the generator is initially synchronised to the electrical power grid. The generator's desired loading can be obtained by adjusting the mechanical power input via the DC-motor control system and the excitation voltage. With the initial conditions configured as required, the generator's circuit breaker and the DC-motor drive is suddenly disconnected, and the measurements are performed.

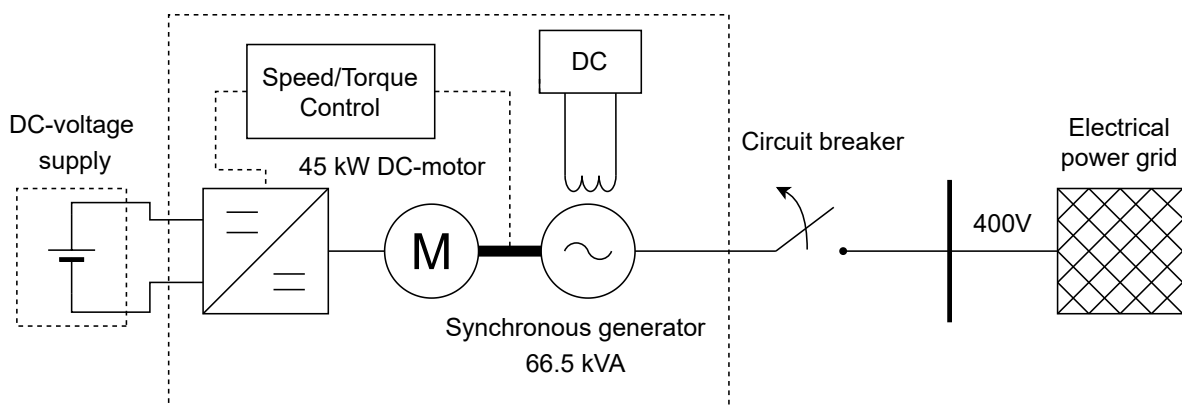


Figure 3.3: Laboratory set-up for the parameter estimation experiments.

Table 3.3: List of the Main Components for the Parameter Estimation Experiments as Presented in Figure 3.3.

| NTNU No. | Component | Producer |
|----------|-----------------------------------|-------------------|
| A02-0035 | Synchronous generator 66.5 kVA | Siemens-Schuckert |
| A01-0136 | Separately excited DC-motor 45 kW | Siemens-Schuckert |
| A02-0035 | DC-motor control system[29, 30] | SINTEF Energy |
| A02-0035 | 40 kW DC-DC half bridge converter | SINTEF/NTNU |
| B02-0729 | 10 A, 200 V DC-rectifier | Elektro-Automatik |

The list of measurement equipment used for measurements in the parameter estimation experiments is presented in Table 3.4. Two oscilloscopes from Tektronix were used for the logging of measurements. The MSO 3014 were used to measure the armature voltages and the field current, and DPO 4054 were used to measure load angle, shaft speed and phase angle. The multi-instrument were used to measure the initial active and reactive power. The initial armature

current was measured with the analogue current meter. A rotary encoder was utilised to measure the shaft's mechanical position, and together with the DC-motor drive and the PicoZed-based processor, the speed and the load angle were calculated respectively. The armature voltages and field current were measured with LEM sensors installed in the synchronous generator's control cabinet and made available through the BNC-ports at the front panel.

Table 3.4: List of Equipment Used for Measurements in the Parameter Estimation Experiments.

| NTNU No. | Component | Type and Producer |
|----------|---------------------------------|---------------------|
| G04-0365 | Mixed signal oscilloscope | MSO 3014, Tektronix |
| G04-0324 | Mixed signal oscilloscope | DPO 4054, Tektronix |
| A01-0136 | Rotary Encoder | ROD 42, Heidenhain |
| A01-0136 | Multi-instrument | MIC-2 MKII, DEIF |
| A01-0136 | Current transducer | HAS 50-S, LEM |
| A01-0136 | Analogue current meter | Hobut |
| A01-0136 | Voltage transducer | LV 25-600, LEM |
| A01-0136 | PicoZed-based processor[31, 32] | SINTEF Energy |

3.3 Description of Equipment

In the following subchapter, a short description of the equipment that is listed in Table 3.1 and 3.3 is given.

3.3.1 Synchronous Generator

A picture of the Siemens-Schuckert motor/generator set is shown in Figure 3.4. The set consists of a 75 kVA salient pole synchronous generator and a 45 kW separately excited DC-motor, further details on the DC-motor is given in subsection 3.3.3. The synchronous generator is seen on the right side of the picture. The machine is connected in star connection with an isolated

Table 3.5: Parameters for the Synchronous Machine.

| Parameter | Value | Origin |
|----------------------|----------|-----------|
| Rated apparent power | 66.5 kVA | Adjusted |
| Rated voltage | 400 V | Chosen |
| Rated current | 96 A | Nameplate |
| Rated speed | 1000 rpm | Nameplate |
| Rated frequency | 50 Hz | Nameplate |
| Rated field current | 11.6 A | Nameplate |
| Rated field Voltage | 120 V | Nameplate |

neutral point. The machine has 6 windings with the possibility to connect the machine in either parallel- or series-connected star connection, and the machine is connected in series giving the rated line-line voltage of 450 V and a rated current of 96 A. The generator is equipped with a full damper cage with damping in both d - and q -axis. The rest of the parameters are shown in

Table 3.5. Even though the rated voltage for the generator is 450 V, it was run with 400 V during the laboratory experiments. This is because the rest of the laboratory set-up is rated for 400 V. The reduced voltage also reduces the nominal power output of the machine to 66.5 kVA. The DC-motor is rated for 45 kW, and the no-load losses at rated speed are about 4.5 kW, making the maximum power output of the synchronous generator about 40.5 kW.



Figure 3.4: Picture of the Siemens-Schuckert motor/generator (45 kW / 75 kVA) set.

3.3.2 Excitation Control for the Synchronous Generator

For the regulation of the field current, a Basler Electric digital excitation control system of type DECS-250N has been utilised. A picture of this unit's control panel is presented in Figure 3.5. The excitation unit has a long list of capabilities and protective functions. The most relevant for this thesis is the possibility for manual control of excitation current and the automatic voltage regulation (AVR). With the generator running at the rated speed and open circuit, a field voltage of 38.5 V and excitation current of 6.14 A gives 400 V line-line armature voltage. The tuning of the AVR is presented in section 4.3.



Figure 3.5: Control panel for the Basler Electric DECS-250N digital excitation control system.

3.3.3 DC-Motor

The DC-motor is connected directly on the same shaft as the synchronous generator. The DC-motor is seen on the left side on Figure 3.4. The nameplate values for the DC-motor is presented in Table 3.6. It can be noted that the rated speed for the DC-motor is 1200 rpm, but the rated speed for the synchronous generator is 1000 rpm, and this gives an electrical frequency of 50 Hz. For this reason, the DC-motor is operated with 1000 rpm as the nominal speed. The control system for the DC-motor is described in Chapter 3.3.4.

Table 3.6: Nameplate Values for the DC-Machine.

| Parameter | Value |
|---------------|----------|
| Rated power | 45kW |
| Rated voltage | 120 V |
| Rated current | 400 A |
| Rated speed | 1200 rpm |

3.3.4 Control System for the DC-Motor

A picture of the DC-control unit interface is shown in Figure 3.6. The user interface can be used to set the references for speed or torque and is also used to set gains of the PI-controllers. There are four BNC analogue output ports on the right side of the unit with a voltage level of 2.5 V. These can be configured to output a range of signals available in the DC-control system, including speed and electrical torque.



Figure 3.6: User interface for the DC-motor control unit (right) and the communication interface for the PicoZed processor card, as described in Chapter 3.4.2.

The DC-machine control system is a modified version of an AC-control system described in [29]. A block diagram describing the control system structure is shown in Figure 3.7. The control system is a classical cascaded speed control with an outer loop regulating the speed and an inner control regulating the armature current. The excitation voltage is kept constant. The Ref. source selector gives the option of choosing between different inputs for the references. These are user interface, CAN bus, analogue signal and optical fibre. In this thesis, the user interface has been used. The torque control selector provides the option to bypass the outer loop and instead regulate directly on the torque.

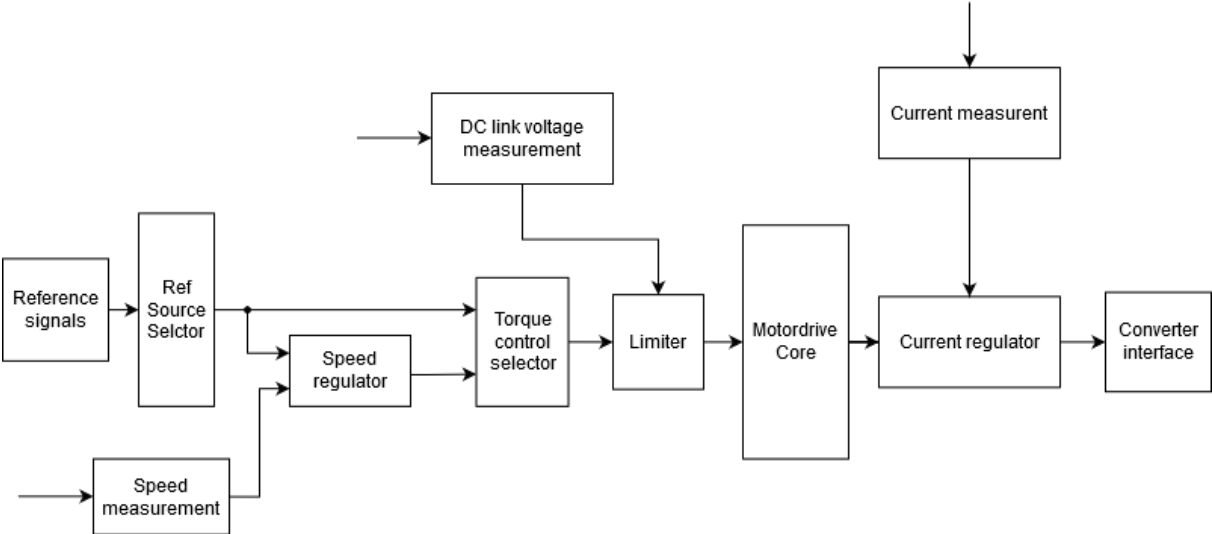


Figure 3.7: Block diagram of the control system for the Siemens-Schuckert DC-motor, based on [29].

The block diagram of the PI-regulator used for the speed control is shown in Figure 3.8. The controller regulates on the difference between the reference value and measured speed. The error is filtered through a low pass filter. The proportional and integral branches have separate gains. Droop functionality is also included. This is an internal droop subtracted from the integral branch and back to the input. This type of droop can make a faster and less noisy response than a conventional external droop loop [29]. The tuning of the speed controller is examined in subsection 4.2.1.

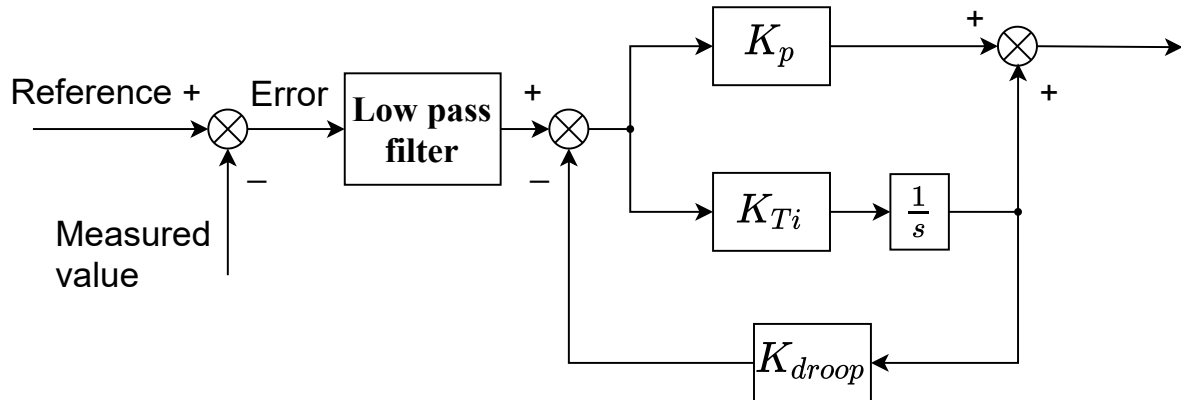


Figure 3.8: Block diagram of the PI-regulator used for speed control in the DC-motor control system, based on [29].

3.3.5 Transformer

The transformer used in this thesis is a 400:400 V three-phase 70 kVA D/y-11 transformer. It is connected in star-connection on the converter side. On the generator side, it is connected in delta-connection.

3.3.6 Water-Cooled Load Resistance

For the local load, the water-cooled load resistance is used. The resistor bank is rated for 55 kW. The resistance value is manually controlled during the experiments with the control panel for the resistor bank.

3.3.7 Line Inductance

A series-connected inductance of 1.7 mH is used to represent a line connecting the converter with the generator.

3.3.8 2-Level Voltage Source Converter (VSC)

The voltage source converter used in the experiments is a 60 kVA 2-level IGBT converter made by SINTEF. A picture of the VSC is included in Appendix D.2, Figure D.2. The converter can be configured in several ways, for example, in a motor drive application. In this thesis, it has been configured as a grid-connected converter and is connected to the grid through an LCL-filter on the output. On the AC side, the voltage is 400V, and on the DC-side a voltage of 700V is supplied by the EGSTON power amplifier. A picture of the power amplifier is presented in Appendix D.3, Figure D.3. Current measurements are performed with LEM - LA205-s current transducers and voltage measurements are performed with LEM - LV25-600 voltage transducers. These measurements are available through the OPAL-RT system. For more details concerning the converter, the reader is referred to [33].

3.3.9 Control system for the VSC

The regulation of the VSC is partly performed on the internal control system described in [29] and partly simulated in real-time on the OPAL-RT. A simplified block diagram for the control system is shown in Figure 3.9. The control system is a conventional PLL-synchronised converter control scheme without grid forming capabilities, which means that the PLL is depended on an established voltage to synchronise with. The relatively slower outer loops with PQ-control and the supplementary inertia control loops are implemented in a Simulink model simulated on the OPAL-RT. The outer loop regulates the active and reactive power with references set by the user in the user interface in Simulink. From the outer loop, references for the d -axis and the q -axis current is sent to the internal control system for the VSC. Here, the faster inner current control loop is implemented on the FPGA card.

For the emulating of virtual inertia, the control loop, as presented in Figure 3.10 was used. This control loop consists of two branches. One branch acts as a frequency droop and adds a signal to the active power reference proportional to the frequency deviation. The droop constant K_w determine how large this effect is. The other branch approximates the derivative of the frequency, as shown in [34]. The approximation is made because the differentiation of noisy signals amplifies the noise. The effect of the df/dt control loop is controlled by the inertia constant K_j . The inertia controller sends a reference to the active power controller called ΔP_j . This reference modify the active power reference based on the frequency dynamics as explained above. With the inertia controller three different control schemes are possible. These are PQ-control without inertia support, droop, df/dt and droop + df/dt .

The control system is based on a template developed by SINTEF and has been adjusted for this thesis with the help of the SINTEF employees Salvatore D'Arco and Raymundo E. Torres-Olguin. The preconfigured tuning of the power controllers and current controllers done by SINTEF was found to be stable, and the only tuning done to this control system in this thesis was done on the supplementary inertia loop. Figure 3.11 shows the workflow of using OPAL-RT to control the converter used in the IE experiments.

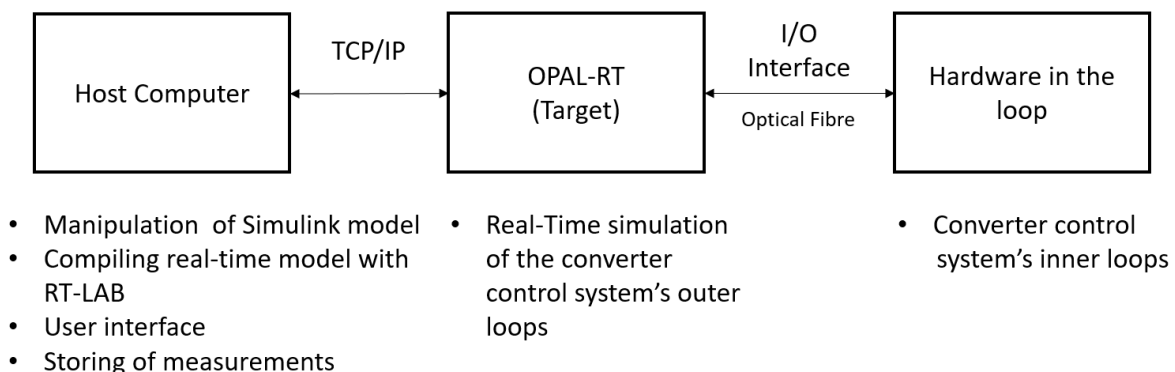


Figure 3.11: Workflow using the OPAL-RT to control the converter, inspired by [35].

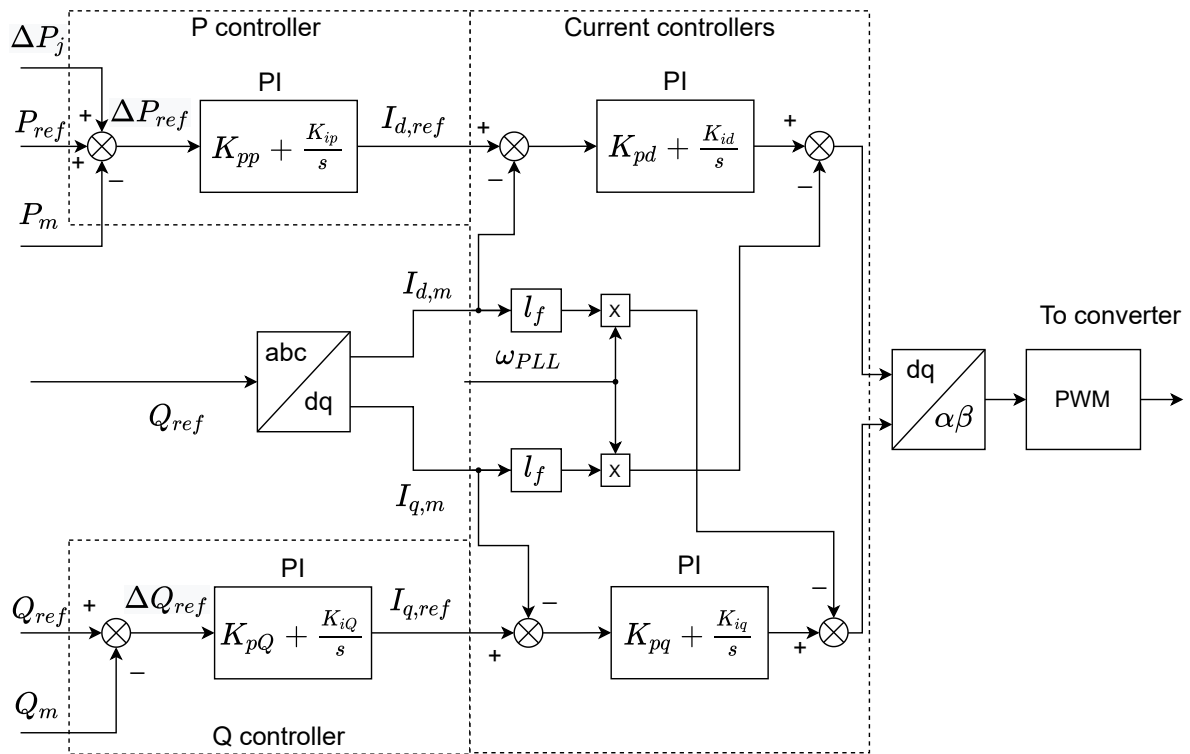


Figure 3.9: Block diagram of the main control loops for the VSC control system.

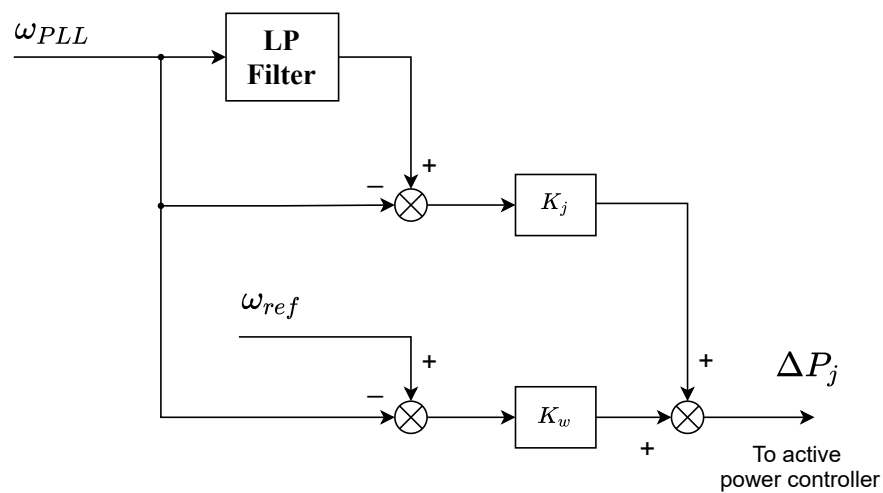


Figure 3.10: Block diagram of the supplementary virtual inertia control loop.

3.4 Description of Measurement Equipment

In the following subchapter the most important instruments listed in Table 3.2 and 3.4 is described.

3.4.1 Tektronix Oscilloscopes

For the logging of measurements, the mixed signal oscilloscope MSO 3014 of the brand Tektronix were used. This oscilloscope has four channels and the possibility of storing plots to USB-drive as comma-separated values (CSV) for analysis. A picture of this oscilloscope is presented in Figure 3.12. The oscilloscope has been set to a 20 long second sweep with 100 000 measurement points, resulting in a sampling period of $2 \cdot 10^{-4}$. Some experiments a 40 second long sweep has been used giving a sampling period of $4 \cdot 10^{-4}$. In some experiments, a second oscilloscope of the type DPO 4054 has been used. This oscilloscope has the same functionality, and identical measurement settings to the MSO 3014 has been used.



Figure 3.12: Picture of the MSO 3014 mixed signal oscilloscope.

3.4.2 PicoZed-Based Processor Board for Synchronous Generator Measurements

In the control cabinet for the motor/generator set, a PicoZed-based processor board is installed. This processor board is described in [31], and the software installed on the processor is based on the synchronous excitation control system described in [32]. The processor board measures the terminal voltages on the synchronous generator and phase currents with the LEM voltage and current transducers (see subsection 3.4.3), and the measurements are then filtered with a first-order filter. The active power is calculated with the two-watt meter method as shown in Equation 3.1 which is an accurate method provided that the sum of currents is equal to zero. [32].

$$P = U_{ac} \cdot I_a + U_{cb} \cdot I_b \quad (3.1)$$

A D/A converter is installed on the card making the measurements available with the four BNC analogue ports on the left side of the DC-motor control unit user interface, as seen in Figure 3.6, with a voltage level of ± 2.5 V. The choice of measurements parameters and conversion ratios are made in the card's software, accessed with USB-connection and a terminal emulator

application called PuTTY. It is also possible to apply an offset on the signal outputted through the D/A converter.

3.4.3 LEM Voltage and Current Transducers

The terminal voltages of the synchronous generator are measured with the LEM LV 25-600 voltage transducer, which is installed in the control cabinet of the synchronous generator. It measures the terminal voltage with a conversion ratio of 10 mV/V and feeds the measurement to the PicoZed processor board and the BNC-ports on the control cabinet's front panel. The BNC-ports can be seen on the picture of the control cabinet shown in Appendix D.1, Figure D.1. The circuit diagram for the voltage measurements is shown in Appendix C.1, Figure C.1.

The synchronous generator's armature currents are similarly measured with the LEM LA 200-S with a conversion ratio of 160 mV/A and feed the measurements to the PicoZed processor board and the BNC ports.

3.4.4 Speed Measurement with Rotary Encoder

The DC-motor's speed measurements are performed with a rotary encoder of type ROD 42 produced by Heidenhain. The encoder is installed directly on the shaft of the generator/motor set and measures mechanical position. This encoder feeds its measurements to the DC-control system, and the speed is calculated. These measurements are made available with a D/A converter in the DC-control system that feeds the signals to the four BNC ports on the control unit's front panel, with a signal of ± 2.5 V.

Preliminary Laboratory Work

4.1 Measurement of Armature Resistance

As a part of the mapping of the synchronous generator's parameters, the armature resistances were measured. The three phases were measured individually between the terminal of the respective phase and the neutral point, and the generator was connected in series-star connection. The measurements were done with a high precision resistance meter called Hioki RM3548 with the NTNU laboratory registration number H01-0128 with the help from Bård Almås at NTNU Service-lab. The measurements were performed with the machine having room temperature. The results of the resistance measurements are shown in Table 4.1.

Table 4.1: Measured Armature Resistance of the Siemens-Schuckert Synchronous Generator, Series-Star Connection.

| V | U | W | Average |
|-----------------|-----------------|-----------------|-----------------|
| 59.1 m Ω | 55.5 m Ω | 56.2 m Ω | 56.9 m Ω |

4.2 Tuning of Speed Controller for the DC-Motor Control System

The initial values for the speed controller is presented in Table 4.2. As the speed controller was tuned to have a fast response, it was necessary to tune the speed controller to be slower. If the speed controller is tuned too aggressively, the synchronous generator will quickly pick up any changes in the electric grid too fast. The tuning of the speed controller is described in the following.

4.2.1 Initial Tuning

For the tuning of the speed controller for the DC-motor, a test was performed where the integral and proportional gains were varied. The DC-machine was in no-load with the synchronous generator being electrically disconnected. A step in the speed reference was performed from 300 to 400 rpm. The low speed was used for the initial tuning because of the noise level created by running the motor at rated speed. The speed is measured by the rotary encoder installed

Table 4.2: Parameter Values for the Speed Controller.

| Parameter | Value |
|------------------------|--------|
| Proportional gain | 20 |
| Integral time constant | 200 ms |
| Filter time constant | 1 ms |
| Droop | 1 % |

on motor/generator set's shaft. The measurements were read with the Tektronix Oscilloscope through the BNC ports on the DC-control unit.

A plot of a selection of the step responses is shown in Figure 4.1a. Here the proportional gain has been varied to see how this affects the speed response. It can be seen that a lower gain gives a larger overshoot and even oscillatory behaviour. This is because the inertia in the motor/generator set acts as a natural integrator [29]. The response starts to oscillate when the gain is reduced to 12. For a gain of 2, an overshoot of 16 % is observed. Step responses with variations of the integration time constant, T_i , is presented in Figure 4.1b. A higher integral time constant yields a lower integration gain. As expected, it can be seen that when the integral time constant is increased the time it takes to remove the speed deviation is also increased.

To get a slower speed response, the proportional gain needs to be reduced while the integral time constant should be increased. The proportional gain should be above 2 to avoid large speed overshoots.

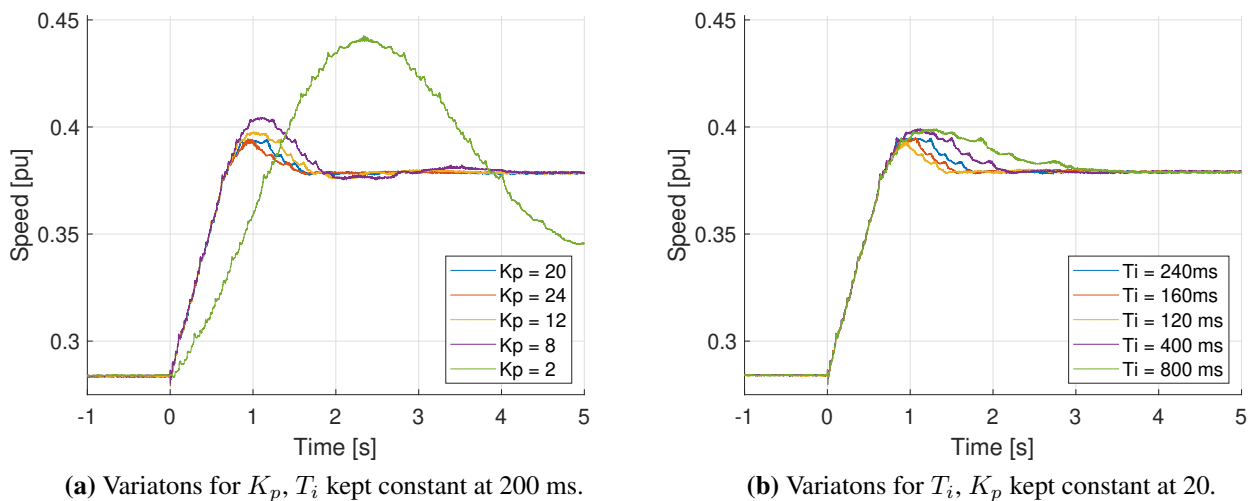


Figure 4.1: Plots of step responses for a step in reference from 300 rpm to 400 rpm with variations for proportional gain K_p and integral time constant T_i .

4.2.2 Tuning with a Step in Electrical Load

The final tuning of the speed controller were done with a second test where the generator was connected to the local water-cooled resistive load (lab No. K01-0505). The armature voltage

was set to an initial value of 400 V line-to-line with manual control of the field current. At time zero seconds, a step in the electrical load was applied from no-load to a resistance value of 11.6Ω . The speed response was recorded, and the gains on the speed controller's proportional and integral branch were varied. The result of this test is plotted in Figure 4.2. With reduced proportional gain and increased integral time constant, a more considerable drop in frequency is found, as expected. It also observed that the frequency nadir occurs at a later time.

The frequency deviations shown in this plot are relatively large, for example, the frequency in the Nordic grid is required to stay within 50 ± 0.1 Hz under normal conditions [5]. A typical frequency nadir occurs after around 5 to 10 seconds after the disturbance [13], the nadirs in this plot occurs between 0.3 to around 2 seconds. Therefore, one of the slower response would be desired. It is also noticed that measured frequency is noisy, and a larger frequency makes the noise relatively smaller. It can be seen that the signals are not perfectly synchronised. The slower the speed controller is tuned, the earlier the frequency drop starts, this is because the oscilloscope was set to automatically trigger on a certain torque level. Slower speed controller also gives a slower torque increase, but this is not seen as an issue in these experiments. For later experiments with frequency dynamics, the signals were synchronised manually to avoid this deviation between different experiments.

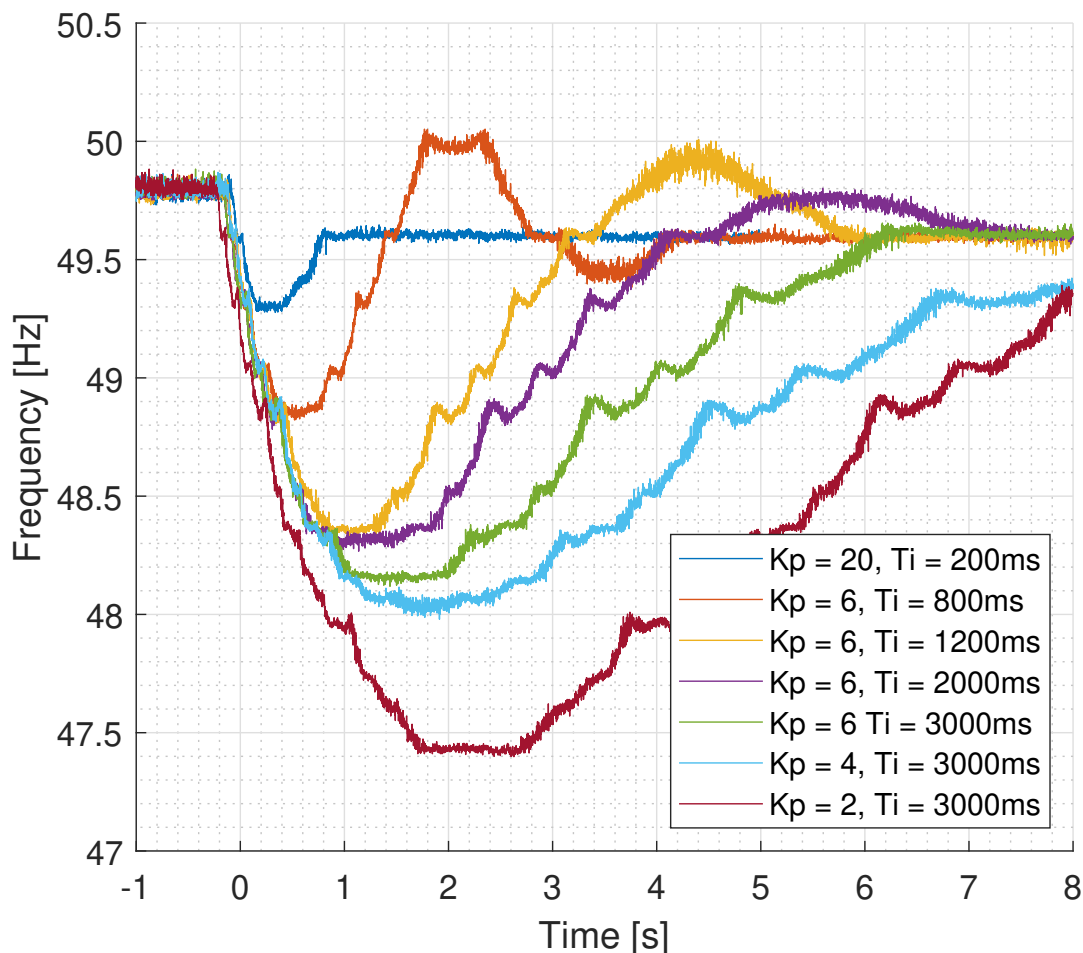


Figure 4.2: Plot of step responses for a step in electrical load from no load to a resistance of 11.6Ω .

The gains chosen for the experiments in this thesis are a proportional gain of 4 and integral times constant of 3000 ms. It is possible to get a slower tuning, but the overshoots are getting larger and more unpractical to work with, as found in the previous subchapter.

4.3 Tuning of Automatic Voltage Regulator (AVR)

The AVR was tested by running the generator running at rated speed with default gains. It was found that the AVR was marginally stable, oscillating between a voltage of 350 - 390 V when the reference of the terminal voltage was set to 400 V. This was not acceptable behaviour, and tuning of the AVR was deemed necessary. The reason the voltage was not oscillating around 400 V but a lower value, was later found to be because of a field limiter that was enabled by default. This limiter was set to reduce the armature voltage when the frequency was under 57.5 Hz. The tuning of the AVR is described in the following.

As the generator's parameters necessary for analytically tuning the AVR were unknown, an attempt was made with the automatic tuning algorithm included with the DECS-250N. Two methods are available to choose from: the pole-zero cancellation method and the pole placement method, a description of these methods can be found in [36] and the self-tuning algorithm is presented in [37]. The tuning was performed with the generator running at rated speed with open terminals and the pole-zero cancellation method was chosen. The gains proposed by the self-tuning algorithm are presented in Table 4.3.

Table 4.3: The Gains for the AVR Proposed by Basler's Automatic Tuning Algorithm.

| K_a | K_p | K_i | K_d |
|-------|-------|-------|-------|
| 0.152 | 5.000 | 11.57 | 0.000 |

To examine the performance of the automatic tuning, a step in voltage reference from 0.95 pu to 1.05 pu was applied with the generator running at rated speed and open-circuit. This method is inspired by [36]. The response with the suggested values is presented in Figure 4.3. The measurement was performed with the PicoZed-Based Processor Board and recorded with the analogue BNC output with the oscilloscope. As observed in Subchapter 4.5, the BNC output of this card has an inaccuracy of 10.2 Volts. To compensate, an offset of 26 bytes was applied. This seems to have resulted in an overcompensating by 0.01 pu as the voltage starts at 0.96 pu and not 0.95 pu.

An initial test was performed with the synchronous generator connected to the converter as described in Chapter 4.4.1 and the system was found to be unstable. The tuning of the AVR was suggested as a reason for this instability. Because of this, a more thorough tuning was performed to analyse the performance of the excitation system. It was decided that the derivative term added unnecessary complexity. Therefore K_d was kept at zero. As a result, the controller structure is reduced to a PI-regulator. The same step in voltage reference was performed as explained above with the gains presented in Table 4.4. K_a was kept constant at the value of 0.152. The case numbers used in Table 4.4 must not be confused with the virtual inertia experiments' case numbers described in Chapter 5.1.

The step responses of case 2 to 4 and case 5 to 7 are presented in Figure 4.4 and Figure 4.5 respectively. Case 1 is not presented here, but can be found in Appendix C.3 Figure C.3. It should be noted that the timescale of Figure 4.4 and 4.5 is not the same as in Figure 4.3. The manually tuned responses are much faster than the one with automatic tuning. Based on the testing with the virtual inertia laboratory set-up described in Subchapter 4.4.2 the chosen gains for the AVR was $K_p = 40$ and $K_i = 8$.

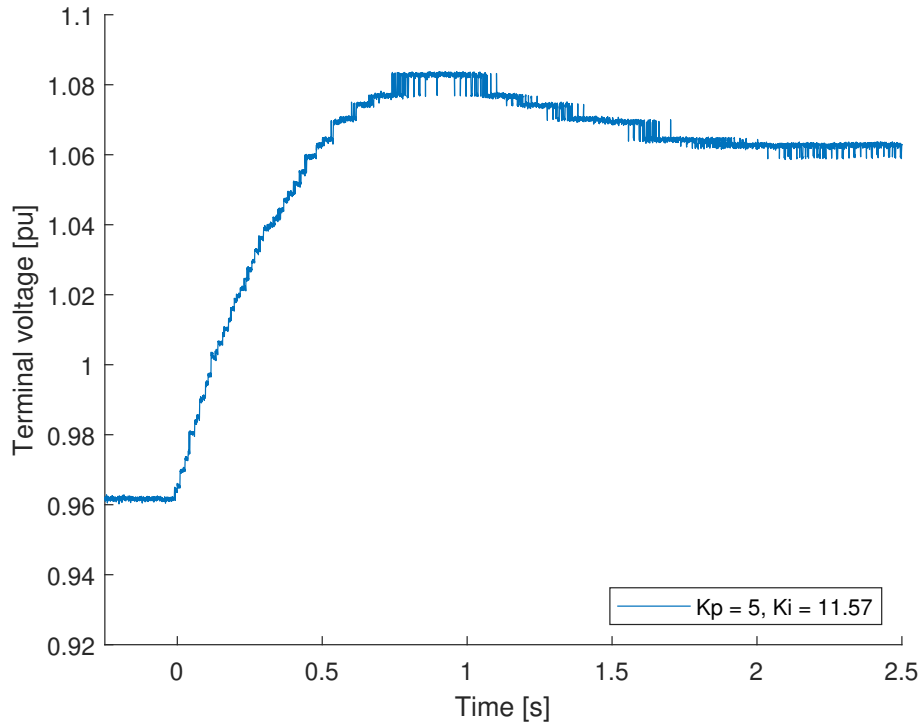


Figure 4.3: Step response for the synchronous generator's terminal voltage for a step in voltage reference from 0.95 pu to 1.1 pu with the gains suggested by Basler Electric automatic tuning algorithm.

Table 4.4: List of Gain Values Tested for Tuning of the AVR.

| Case No. | K_p | K_i |
|----------|-------|-------|
| 1 | 5 | 0 |
| 2 | 40 | 0 |
| 3 | 50 | 0 |
| 4 | 80 | 0 |
| 5 | 32 | 8 |
| 6 | 40 | 8 |
| 7 | 50 | 5 |

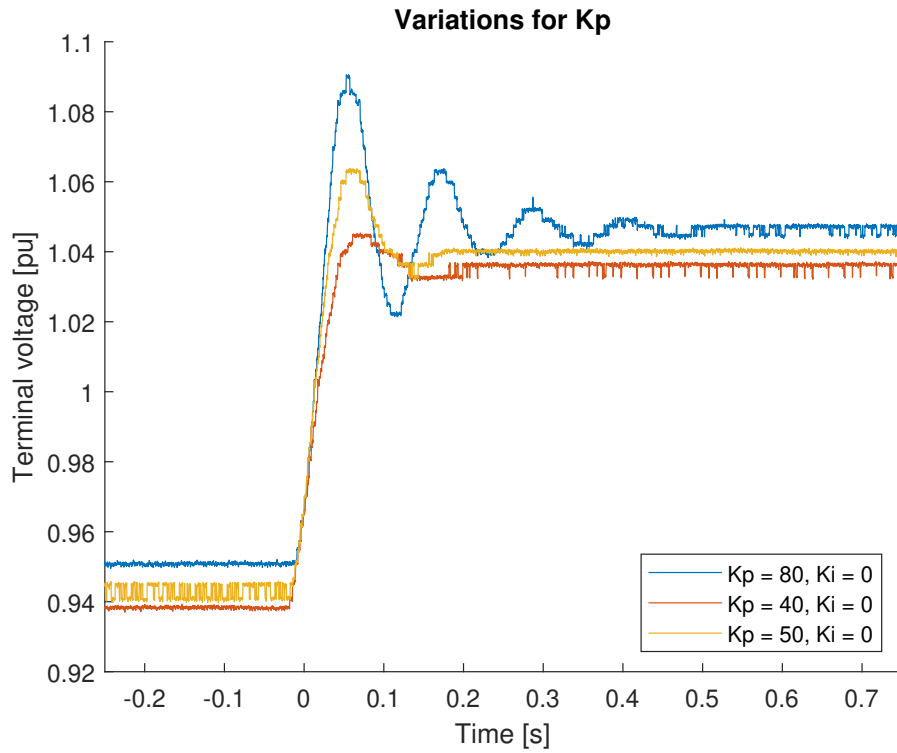


Figure 4.4: Step response for the synchronous generator's terminal voltage for a step in voltage reference from 0.95 pu to 1.1 pu case 2 to 4.

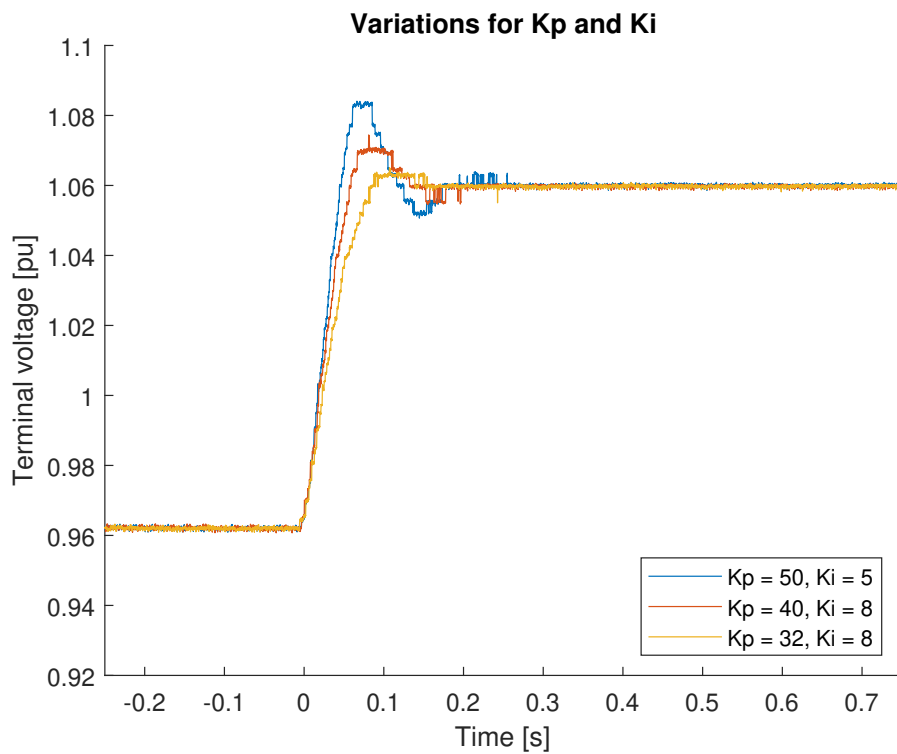


Figure 4.5: Step response for the synchronous generator's terminal voltage for a step in voltage reference from 0.95 pu to 1.1 pu for case 5 to 7.

4.4 Initial Test of the Virtual Inertia Laboratory Set-Up

4.4.1 Test with Automatic Tuning of the AVR

An initial test was performed with the converter synchronised to the Siemens-Schuckert synchronous generator. The setup was connected as shown in Appendix D.5, Figure D.5. First, the generator was accelerated up to the nominal speed, and the voltage was controlled by the AVR with the gains suggested by Basler's automatic tuning algorithm as presented in Chapter 4.3, Table 4.3. When the voltage was established, the converter was synchronised to the grid and connected. Both current control and PQ-control of the converter were tested. The current control showed stable results, but the PQ-control became unstable when a step in the load of about 10 kW was applied. The converter and the synchronous generator started to oscillate against each other. The control parameters for the control system used during this experiment are presented in table Table 4.5. The power and current controllers' parameters are tuned by SINTEF and have been kept unchanged for the experiments performed in this thesis.

Table 4.5: Control System Parameters for Initial Test of Laboratory Experiment.

| Speed Controller | | AVR | | Current Controller | | Power Controller | |
|------------------|----------|----------|----------|--------------------|-------------|------------------|----------|
| K_{pn} | T_{in} | K_{pa} | K_{ia} | K_{pi} | T_{ii} | K_{pp} | T_{ip} |
| 4 | 3 s | 5 | 11.57 | 4 | 500 μ s | 1 | 10 s |

The oscillations could have been the result of several factors. It might be that the PQ-regulator needed tuning. If the outer PQ-controller is faster than the inner current control loop, the inner loop will not manage to follow the outer loop and oscillate between the converter's upper and lower limit. It might also be that the AVR was not tuned properly. If the integrator gain on the voltage regulator is too high, instability might occur.

4.4.2 Test with Manual Tuning of the AVR

After the initial test of the laboratory setup it was attempted to tune the AVR manually, this tuning is presented in Chapter 4.3. The setup was tested again with a pure P-regulator and a PI-regulator with a modest integral gain, these two controller schemes are shown in Table 4.6.

Table 4.6: List of AVR Gain Values Tested for the Initial Virtual Inertia Experiment.

| | K_p | K_i |
|----|-------|-------|
| P | 40 | 0 |
| PI | 40 | 8 |

Several tests were performed with these gains, and it was found that the system was stable for both alternatives. Two examples are shown in Figure 4.6 and 4.7. During these initial tests, the converter was regulated with the PQ-control scheme without any IE. The voltage reference for the AVR was set to 400 V.

In Figure 4.6 a step in the load of 15.8 kW was applied at time 0 s with the pure proportional regulator for the AVR. Figures 1 and 2 show the active power flow out from the generator and the converter, respectively. Before the step in load, the generator is drawing power from the converter. This is due to the set-point for the active power of the converter is higher than baseload. As no reverse power protection is installed for the generator, this operating point is allowed. It can be observed from the figures that the generator is compensating for the whole step in load. Only a small transient is seen on the converter's active power flow before returning to the initial value. This behaviour is as expected for the chosen control scheme for the converter. In Figure 4.8a the terminal voltage of the generator for the same experiment is shown, it can be seen that the voltage has a steady deviation of about 10 volts, this is due to the integrator gain is set to zero. It has been observed that the voltage drops by about 7 volts before it recovers back to the initial value after a short transient.

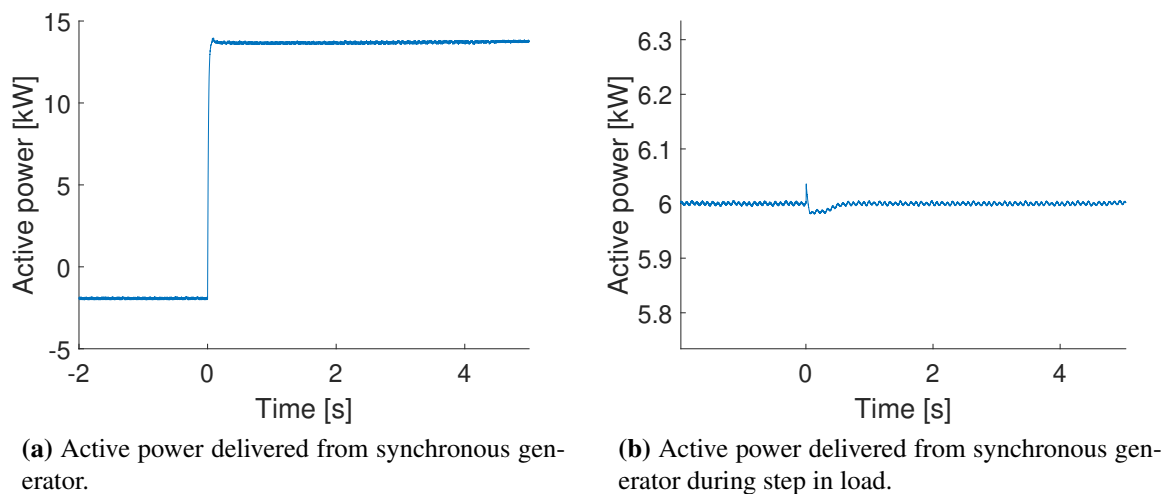


Figure 4.6: Step in load from 39.4 Ω to 7.8 Ω with AVR gains $K_p = 40$ and $K_i = 0$.

Figure 4.7a presents the generator's active power flow for the case with a PI-controlled AVR, and the active power flow from the converter is shown in Figure 4.7b. The terminal voltage for this experiment is presented in Figure 4.8b. With the integral gain set to 8, the AVR remove the steady-state deviation on the terminal voltage. The voltage drop is 5 V, which is 2 V smaller than for the pure P-controller. Similarly as for the P-controller, the voltage returns to the initial value after a short transient. The same step in resistance is applied in this experiment, but the resulting step in active power is higher due to the difference in voltage. The value of the active power step with integral effect is 16.4 kW . A similar response is seen for the active power as for the case with pure P regulator, which is that the generator delivers the whole step in load while the converter is almost unaffected by the step.

The initial tests of the system shows that with the gains for the AVR as presented in Table 4.6 and the gains for the converter as shown in 4.5 the system is stable and can withstand a large step in load without losing stability. As both P- and PI-regulators were shown to be stable, the PI-regulator is used for the virtual inertia experiments. This because the PI-regulator removes the steady-state error on the voltage and maintains the voltage at the rated voltage. The PI-controller also show a smaller voltage deviation during transients.

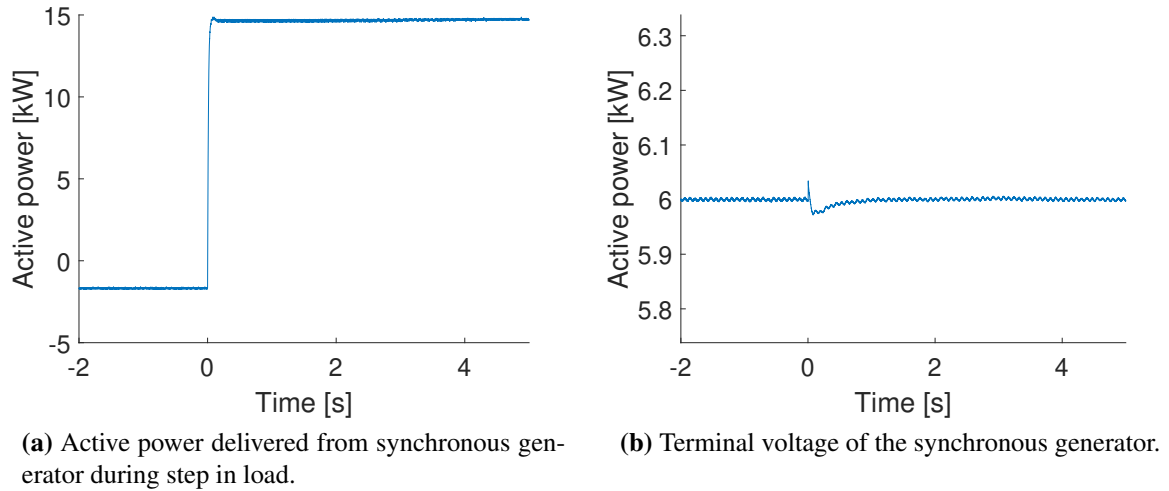


Figure 4.7: Step in load from 39.4Ω to 7.8Ω with AVR gains $K_p = 40$ and $K_i = 8$.

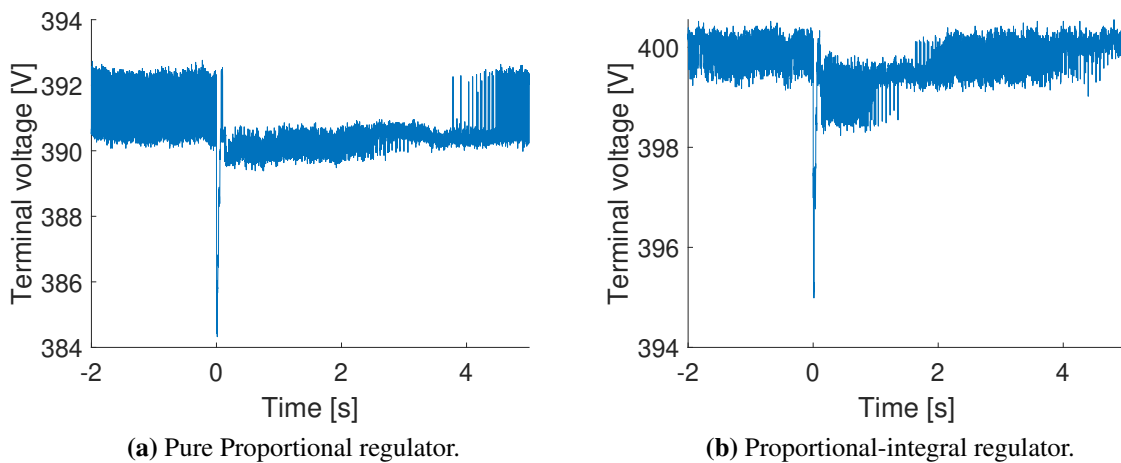


Figure 4.8: Terminal voltages of the generator for a step in load from 39.4Ω to 7.8Ω

4.5 Accuracy of Measurements

In the following subchapter, a short comparison of the different measurement methods available is presented. The measurement of armature voltage, speed, active power and armature current of the synchronous generator is examined. The measurement instruments used in these comparison are listed in Table 4.7.

Table 4.7: List of Equipment Used for Accuracy Examination.

| NTNU No. | Component | Type and Producer |
|----------|--|---------------------|
| G04-0365 | Mixed signal oscilloscope | MSO 3014, Tektronix |
| A01-0136 | Rotary Encoder | ROD 42, Heidenhain |
| S03-0439 | Multimeter | 175 True RMS, Fluke |
| A01-0136 | Multi-instrument | MIC-2 MKII, DEIF |
| A01-0136 | Current transducer | HAL 200-S, LEM |
| A01-0136 | Voltage transducer | LV 25-600, LEM |
| A01-0136 | PicoZed-based processor[31, 32] | SINTEF Energy |
| I06-0516 | Voltage Differential Probes | P5200A, Tektronix |
| A01-0136 | Excitation control for synchronous generator | DECS-250N, Basler |
| A02-0035 | DC-motor control system [29, 30] | SINTEF Energy |

4.5.1 Voltage Measurements

Different methods for measuring voltage were inspected. The different methods were high voltage differential probe, the use of BNC-ports installed on the control cabinet, and the PicoZed processor card read through the PuTTY terminal emulator and the BNC port analogue output. The voltage was measured with the generator running no-load at rated speed. The result of rms voltage measurement with the different methods is presented in Table 4.8. Of these different methods, the multi-instrument is deemed the most accurate. Average rms value measured with the oscilloscope for the three phases is calculated to be 389.2 V. The percentage difference between this method and the multi-instrument is found to be 2.79%. A plot of the three-phase voltage as measured with the oscilloscope is included in Appendix C.2, Figure C.2. For the PicoZed processor card a voltage difference of 10.2 V is found between the digital value read with the software and the analogue value read with BNC-port and the oscilloscope.

Table 4.8: rms Armature Voltage of the Synchronous Generator Measured with Different Measurement Equipment.

| Multi-instrument | Diff. probe | L1-L2 | L1-L2 | L1-L2 | Proc. Card | Proc. Card BNC |
|------------------|-------------|--------|--------|--------|------------|----------------|
| 400.4 V | 397.2V | 388.8V | 390.8V | 388.1V | 399V | 388.8V |

4.5.2 Speed Measurements

The speed measurement was examined by running the generator/motor set in no-load with a speed reference of 1000 rpm. The shaft's mechanical position was measured with the rotary encoder, and the speed was calculated by the DC-motor drive. Measured speed was read with

the motor drive's display and with the oscilloscope through the D/A converter on the motor drive made available through the BNC port. The result is shown Table 4.9.

Table 4.9: Speed Measurements through the DC-motor Drive.

| Proc. Card | Proc. Card BNC |
|------------|----------------|
| 0.999 pu | 0.972 pu |

It is found that the speed value read with the oscilloscope through the D/A converter is less than the value read on display. If the value read on DC-motor drive display is assumed to be correct the speed as recorded by the oscilloscope has an inaccuracy of about 2.7 %.

4.5.3 Active Power Measurements

The active power output of the generator was measured with the different methods. For this test, the active power measurement available in the Basler DECS-250N, the multi-instrument, the PicoZed processor card and the Picozed processor card through the D/A converter and BNC ports were used. The test was done with an average measured phase resistance of 8.6 Ω , and a line-line voltage of 400.1 V as measured with the multimeter. With these values, an active power of 18.61 kW would be expected. The result from the different measurement equipment is presented in Table 4.10. It should be noted that the resistance measurement is also uncertain. The water-cooled resistances have an old control panel with old contactors. The measured value of the resistance varies with roughly $\pm 1 \Omega$ when the contactors are turned on and off and the resistance was measured with room temperatures. The active power, measured with the oscilloscope and the D/A converter is 3.5 % lower than the value read digitally with the software. The difference between multi-instrument and the oscilloscope is 6.3 %.

Table 4.10: Active Power Measurements with Different Measurement Equipment.

| Basler | Multi-instrument | Proc. Card | Proc. Card BNC |
|----------|------------------|------------|----------------|
| 18.96 kW | 18.99 kW | 18.45 kW | 17.8 kW |

4.5.4 Current Measurements

The current measurement was tested with the same conditions as for the active power measurements. With an average line-line voltage of 400.1 V as measured with the multimeter and resistance of 8.6 Ω the phase current of 26.86, A is expected. The measured currents with the multi-instrument and BNC ports are shown in Table 4.11. As for the active power measurements, it should be noted that the resistance measurement is not accurate. The difference between the average current measured with the multi-instrument and the average current measured with the oscilloscope is 2.15 %.

Table 4.11: Current Measurements with Different Measurement Equipment.

| Basler | Multi-instrument | BNC L1 | BNC L2 | BNC L3 | BNC average |
|---------|------------------|---------|---------|--------|-------------|
| 27.46 A | 27.51 A | 26.86 A | 26.90 A | 27.00 | A 26.92 A |

4.5.5 Summary of the Measurements Accuracy Evaluation

It is not possible to conclude which measuring equipment is the most accurate from these tests, but it is possible to get a rough idea of the accuracy that can be expected. It is found that the different measurement methods differ by a few per cent in their measurements of voltage, current, active power and speed. The measurements done with the oscilloscope, and the BNC-ports on the control cabinet's front panel are generally 2-3 % lower than what is found with the DEIF multi-instrument. The most significant difference is found to be on the active power measurement with multi-instrument and analogue output of the PicoZed processor card. Here the analogue output of PicoZed processor as measured with the oscilloscope is 6.3% lower than the DEIF multi-instrument. The measurement accuracy of the different equipment available was not investigated further, but as the oscilloscope generally was a few per cent lower than the other instruments, it was suspected that the oscilloscope needed recalibration. The built-in automatic calibration tool was used, but no change was recorded.

Results and Discussion - Virtual Inertia Experiments

5.1 Case Description

A series of experiments were performed, these are all listed in Table 5.1. This table presents the initial loading conditions for the generator and converter, the control parameters for the virtual inertia controller and the disturbance applied in the experiment. The generator is denoted with the subscript g and the converter is denoted with the subscript c . The constants K_w and K_j are the droop and df/dt gains, respectively, as explained in Chapter 3.3.9. A selection of these experiments are presented and discussed in the following chapter

The cases 1 to 18 aims to investigate the difference between the three control alternatives for the converter. The initial load condition for the converter and the generator has also been varied to see how the initial loading affects the converters' performance. These load conditions are listed in the following.

- Shared active power between the generator and converter, and zero reactive power from the converter
- Shared active power between the generator and converter, and negative reactive power from the converter
- Shared active power between the generator and converter, and positive reactive power from the converter
- Generator running no-load and zero reactive power
- Generator running no-load and overexcited
- Generator running no-load and underexcited

Case 19 is a repetition of case 10 but with a larger step in load. Case 20 is identical with 19, except for the step going from high to low load. The initial reactive power loading of cases 13-15 are missing because of a misstep in the laboratory experiments which resulted in the reactive

power measurements for these cases not being recorded.

Cases 21 to 27 test how the droop and df/dt gains affect the performance. Here the initial load condition is kept constant. However, it can be noted that the initial active power varies due to frequency droop on the converter being changed. Case 28 is a repetition of case 27, as case 27 was unstable. The instability did not improve on the second attempt.

Cases 29 to 44 are performed to find the stability limit for the virtual inertia controller. These experiments are performed with the same initial values as cases 7 to 9, except for the droop and df/dt constants being varied

Cases 45 to 47 investigate how a drop in DC-Voltage influence the system.

Table 5.1: Case Description for the Virtual Inertia Experiments.

| Case | Ctrl. Method | Initial Load Condition | | Param. | Disturbance |
|------|---------------|---|---|------------------------|-----------------------|
| 1 | PQ | $P_c = 5.0 \text{ kW}$ $P_g = 8.2 \text{ kW}$ | $Q_c = 0.0 \text{ kVAr}$ $Q_g = 1.3 \text{ kVAr}$ | $K_w = 0$ $K_j = 0$ | Step up of 13.3 kW |
| 2 | Droop | $P_c = 5.6 \text{ kW}$ $P_g = 7.6 \text{ kW}$ | $Q_c = 0.0 \text{ kVAr}$ $Q_g = 1.3 \text{ kVAr}$ | $K_w = 5$ $K_j = 0$ | Step up of 13.3 kW |
| 3 | Droop + df/dt | $P_c = 5.6 \text{ kW}$ $P_g = 7.6 \text{ kW}$ | $Q_c = 0.0 \text{ kVAr}$ $Q_g = 1.3 \text{ kVAr}$ | $K_w = 5$ $K_j = 5$ | Step up of 13.3 kW |
| 4 | PQ | $P_c = 5.0 \text{ kW}$ $P_g = 8.2 \text{ kW}$ | $Q_c = 8.0 \text{ kVAr}$ $Q_g = -8.2 \text{ kVAr}$ | $K_w = 0$ $K_j = 0$ | Step up of 13.3 kW |
| 5 | Droop | $P_c = 5.6 \text{ kW}$ $P_g = 7.6 \text{ kW}$ | $Q_c = 8.0 \text{ kVAr}$ $Q_g = -8.2 \text{ kVAr}$ | $K_w = 5$ $K_j = 0$ | Step up of 13.3 kW |
| 6 | Droop + df/dt | $P_c = 5.6 \text{ kW}$ $P_g = 7.6 \text{ kW}$ | $Q_c = 8.0 \text{ kVAr}$ $Q_g = -8.2 \text{ kVAr}$ | $K_w = 5$ $K_j = 5$ | Step up of 13.3 kW |
| 7 | PQ | $P_c = 5.0 \text{ kW}$ $P_g = 8.2 \text{ kW}$ | $Q_c = -8.0 \text{ kVAr}$ $Q_g = 6.7 \text{ kVAr}$ | $K_w = 0$ $K_j = 0$ | Step up of 13.3 kW |
| 8 | Droop | $P_c = 5.6 \text{ kW}$ $P_g = 7.6 \text{ kW}$ | $Q_c = -8.0 \text{ kVAr}$ $Q_g = 6.7 \text{ kVAr}$ | $K_w = 5$ $K_j = 0$ | Step up of 13.3 kW |
| 9 | Droop + df/dt | $P_c = 5.6 \text{ kW}$ $P_g = 7.6 \text{ kW}$ | $Q_c = -8.0 \text{ kVAr}$ $Q_g = 6.7 \text{ kVAr}$ | $K_w = 5$ $K_j = 5$ | Step up of 13.3 kW |
| 10 | PQ | $P_c = 14.2 \text{ kW}$ $P_g = 0.0 \text{ kW}$ | $Q_c = 1.3 \text{ kVAr}$ $Q_g = 0.0 \text{ kVAr}$ | $K_w = 0$ $K_j = 0$ | Step up of 13.3 kW |
| 11 | Droop | $P_c = 14.2 \text{ kW}$ $P_g = 0.0 \text{ kW}$ | $Q_c = 1.3 \text{ kVAr}$ $Q_g = 0.0 \text{ kVAr}$ | $K_w = 5$ $K_j = 0$ | Step up of 13.3 kW |
| 12 | Droop + df/dt | $P_c = 14.2 \text{ kW}$ $P_g = 0.0 \text{ kW}$ | $Q_c = 1.3 \text{ kVAr}$ $Q_g = 0.0 \text{ kVAr}$ | $K_w = 5$ $K_j = 5$ | Step up of 13.3 kW |
| 13 | PQ | $P_c = 14.2 \text{ kW}$ $P_g = 0.0 \text{ kW}$ | $Q_c = 12.3 \text{ kVAr}$ $Q_g = \text{—}$ | $K_w = 0$ $K_j = 0$ | Step up of 13.3 kW |
| 14 | Droop | $P_c = 14.2 \text{ kW}$ $P_g = 0.0 \text{ kW}$ | $Q_c = -11.7 \text{ kVAr}$ $Q_g = \text{—}$ | $K_w = 5$ $K_j = 0$ | Step up of 13.3 kW |
| 15 | Droop + df/dt | $P_c = 14.2 \text{ kW}$ $P_g = 0.0 \text{ kW}$ | $Q_c = -11.7 \text{ kVAr}$ $Q_g = \text{—}$ | $K_w = 5$ $K_j = 5$ | Step up of 13.3 kW |

Table 5.1: *Continued from previous page*

| Case | Ctrl. Method | Initial Load Condition | | Ctrl. | Disturbance |
|------|---------------|---|---|--------------------------|------------------------------|
| 16 | PQ | $P_c = 14.2 \text{ kW}$ $P_g = 0.0 \text{ kW}$ | $Q_c = 9.9 \text{ kVAr}$ $Q_g = -11 \text{ kVAr}$ | $K_w = 0$ $K_j = 0$ | Step up of 13.3 kW |
| 17 | Droop | $P_c = 14.2 \text{ kW}$ $P_g = 0.0 \text{ kW}$ | $Q_c = 9.9 \text{ kVAr}$ $Q_g = -11 \text{ kVAr}$ | $K_w = 5$ $K_j = 0$ | Step up of 13.3 kW |
| 18 | Droop + df/dt | $P_c = 14.2 \text{ kW}$ $P_g = 0.0 \text{ kW}$ | $Q_c = 9.9 \text{ kVAr}$ $Q_g = -11 \text{ kVAr}$ | $K_w = 5$ $K_j = 5$ | Step up of 13.3 kW |
| 19 | PQ | $P_c = 14.2 \text{ kW}$ $P_g = 0.0 \text{ kW}$ | $Q_c = -1.3 \text{ kVAr}$ $Q_g = 0.0 \text{ kVAr}$ | $K_w = 0$ $K_j = 0$ | Step up of 27.2 kW |
| 20 | PQ | $P_c = 14.2 \text{ kW}$ $P_g = 0.0 \text{ kW}$ | $Q_c = -1.3 \text{ kVAr}$ $Q_g = 0.0 \text{ kVAr}$ | $K_w = 0$ $K_j = 0$ | Step down of 27.2 kW |
| 21 | df/dt | $P_c = 5.0 \text{ kW}$ $P_g = 8.2 \text{ kW}$ | $Q_c = -8.0 \text{ kVAr}$ $Q_g = 6.7 \text{ kVAr}$ | $K_w = 0$ $K_j = 5$ | Step up of 13.3 kW |
| 22 | Droop | $P_c = 5.0 \text{ kW}$ $P_g = 8.2 \text{ kW}$ | $Q_c = -8.0 \text{ kVAr}$ $Q_g = 6.7 \text{ kVAr}$ | $K_w = 1$ $K_j = 0$ | Step up of 13.3 kW |
| 23 | df/dt | $P_c = 5.0 \text{ kW}$ $P_g = 8.2 \text{ kW}$ | $Q_c = -8.0 \text{ kVAr}$ $Q_g = 6.7 \text{ kVAr}$ | $K_w = 0$ $K_j = 1$ | Step up of 13.3 kW |
| 24 | Droop + df/dt | $P_c = 5.0 \text{ kW}$ $P_g = 8.2 \text{ kW}$ | $Q_c = -8.0 \text{ kVAr}$ $Q_g = 6.7 \text{ kVAr}$ | $K_w = 1$ $K_j = 1$ | Step up of 13.3 kW |
| 25 | Droop | $P_c = 6.1 \text{ kW}$ $P_g = 7.1 \text{ kW}$ | $Q_c = -8.0 \text{ kVAr}$ $Q_g = 6.7 \text{ kVAr}$ | $K_w = 10$ $K_j = 0$ | Step up of 13.3 kW |
| 26 | df/dt | $P_c = 5.0 \text{ kW}$ $P_g = 8.2 \text{ kW}$ | $Q_c = -8.0 \text{ kVAr}$ $Q_g = 6.7 \text{ kVAr}$ | $K_w = 0$ $K_j = 10$ | Step up of 13.3 kW |
| 27 | Droop + df/dt | $P_c = 6.1 \text{ kW}$ $P_g = 7.1 \text{ kW}$ | $Q_c = -8.0 \text{ kVAr}$ $Q_g = 6.7 \text{ kVAr}$ | $K_w = 10$ $K_j = 10$ | Step up of 13.3 kW |
| 28 | Droop + df/dt | $P_c = 6.1 \text{ kW}$ $P_g = 7.1 \text{ kW}$ | $Q_c = -8.0 \text{ kVAr}$ $Q_g = 6.7 \text{ kVAr}$ | $K_w = 10$ $K_j = 10$ | No disturbance (unstable) |
| 29 | Droop + df/dt | $P_c = 5.7 \text{ kW}$ $P_g = 7.5 \text{ kW}$ | $Q_c = -8.0 \text{ kVAr}$ $Q_g = 6.7 \text{ kVAr}$ | $K_w = 6$ $K_j = 6$ | Step up of 13.3 kW |
| 30 | Droop + df/dt | $P_c = 5.6 \text{ kW}$ $P_g = 7.6 \text{ kW}$ | $Q_c = -8.0 \text{ kVAr}$ $Q_g = 6.7 \text{ kVAr}$ | $K_w = 5$ $K_j = 6$ | Step up of 13.3 kW |
| 31 | Droop + df/dt | $P_c = 5.6 \text{ kW}$ $P_g = 7.6 \text{ kW}$ | $Q_c = -8.0 \text{ kVAr}$ $Q_g = 6.7 \text{ kVAr}$ | $K_w = 5$ $K_j = 7$ | Step up of 13.3 kW |
| 32 | Droop + df/dt | $P_c = 5.6 \text{ kW}$ $P_g = 7.6 \text{ kW}$ | $Q_c = -8.0 \text{ kVAr}$ $Q_g = 6.7 \text{ kVAr}$ | $K_w = 5$ $K_j = 8$ | Step up of 13.3 kW |
| 33 | Droop + df/dt | $P_c = 5.6 \text{ kW}$ $P_g = 7.6 \text{ kW}$ | $Q_c = -8.0 \text{ kVAr}$ $Q_g = 6.7 \text{ kVAr}$ | $K_w = 5$ $K_j = 9$ | Step up of 13.3 kW |
| 34 | Droop + df/dt | $P_c = 5.6 \text{ kW}$ $P_g = 7.6 \text{ kW}$ | $Q_c = -8.0 \text{ kVAr}$ $Q_g = 6.7 \text{ kVAr}$ | $K_w = 5$ $K_j = 10$ | Step up of 13.3 kW |
| 35 | Droop + df/dt | $P_c = 5.6 \text{ kW}$ $P_g = 7.6 \text{ kW}$ | $Q_c = -8.0 \text{ kVAr}$ $Q_g = 6.7 \text{ kVAr}$ | $K_w = 5$ $K_j = 11$ | Step up of 13.3 kW |
| 36 | Droop + df/dt | $P_c = 5.6 \text{ kW}$ $P_g = 7.6 \text{ kW}$ | $Q_c = -8.0 \text{ kVAr}$ $Q_g = 6.7 \text{ kVAr}$ | $K_w = 5$ $K_j = 12$ | No disturbance (unstable) |
| 37 | Droop + df/dt | $P_c = 5.7 \text{ kW}$ $P_g = 7.5 \text{ kW}$ | $Q_c = -8.0 \text{ kVAr}$ $Q_g = 6.7 \text{ kVAr}$ | $K_w = 6$ $K_j = 5$ | Step up of 13.3 kW |

Table 5.1: *Continued from previous page*

| Case | Ctrl. Method | Initial Load Condition | | Ctrl. | Disturbance |
|------|---------------|------------------------------------|---------------------------------------|-------------------------|----------------------------------|
| 38 | Droop + df/dt | $P_c = 5.8$ kW $P_g = 7.4$ kW | $Q_c = -8.0$ kVAr $Q_g = 6.7$ kVAr | $K_w = 7$ $K_j = 5$ | Step up of 13.3 kW |
| 39 | Droop + df/dt | $P_c = 5.8$ kW $P_g = 7.4$ kW | $Q_c = -8.0$ kVAr $Q_g = 6.7$ kVAr | $K_w = 8$ $K_j = 5$ | Step up of 13.3 kW |
| 40 | Droop + df/dt | $P_c = 5.9$ kW $P_g = 7.3$ kW | $Q_c = -8.0$ kVAr $Q_g = 6.7$ kVAr | $K_w = 9$ $K_j = 5$ | Step up of 13.3 kW |
| 41 | Droop + df/dt | $P_c = 6.1$ kW $P_g = 7.1$ kW | $Q_c = -8.0$ kVAr $Q_g = 6.7$ kVAr | $K_w = 10$ $K_j = 5$ | Step up of 13.3 kW |
| 42 | Droop + df/dt | $P_c = 6.2$ kW $P_g = 6.9$ kW | $Q_c = -8.0$ kVAr $Q_g = 6.7$ kVAr | $K_w = 11$ $K_j = 5$ | Step up of 13.3 kW |
| 43 | Droop + df/dt | $P_c = 7.7$ kW $P_g = 19.27$ kW | $Q_c = -8.0$ kVAr $Q_g = 6.7$ kVAr | $K_w = 11$ $K_j = 5$ | Step down of 13.3 kW |
| 44 | Droop + df/dt | $P_c = 25.4$ kW $P_g = 2.3$ kW | $Q_c = -8.0$ kVAr $Q_g = 6.9$ kVAr | $K_w = 11$ $K_j = 5$ | Step down of 13.3 kW |
| 45 | Droop + df/dt | $P_c = 5.6$ kW $P_g = 7.6$ kW | $Q_c = -8.0$ kVAr $Q_g = 6.7$ kVAr | $K_w = 5$ $K_j = 5$ | DC Voltage step down to 650 V |
| 46 | Droop + df/dt | $P_c = 5.6$ kW $P_g = 7.6$ kW | $Q_c = -8.0$ kVAr $Q_g = 6.7$ kVAr | $K_w = 5$ $K_j = 5$ | DC Voltage step down to 600 V |
| 47 | Droop + df/dt | $P_c = 5.6$ kW $P_g = 7.6$ kW | $Q_c = -8.0$ kVAr $Q_g = 6.7$ kVAr | $K_w = 5$ $K_j = 5$ | DC Voltage step down to 550 V |

5.2 Comparison of the Different Converter Control Schemes

An experiment was performed to show the performance of three different control schemes for the converter. These were PQ-control, droop and droop + df/dt. For this experiment, the system was connected as shown in Appendix D.5, Figure D.5. The control system parameters used for these experiments are presented in Table 5.2. The speed controller gains for the DC-motor were selected based on the tuning results presented in Chapter 4.2.1. The AVR settings were based on the result from the initial test of the laboratory set-up, as discussed in Chapter 4.4.1. The converter was set to deliver 5 kW active power and to draw 8 kVAr reactive power. These cases correspond to cases 7 to 9 in Table 5.1. A step in the electrical load from 11.6 Ω to 5.7 Ω was applied at time 0 s. Everything in these experiments was kept constant except for the three different control schemes to get a valid comparison.

Table 5.2: Control System Parameters of Laboratory Experiment.

| Speed Cont. | | AVR | | Current Cont. | | Power Cont. | | Inertial Cont. | |
|-------------|----------|----------|----------|---------------|-------------|-------------|----------|----------------|-------|
| K_{pn} | T_{in} | K_{pa} | K_{ia} | K_{pi} | T_{ii} | K_{pp} | T_{ip} | K_w | K_j |
| 4 | 3 s | 40 | 8 | 4 | 500 μ s | 1 | 10 s | 5 | 5 |

Figure 5.1 shows the synchronous generator's speed during the step in load for the different controller schemes. It is assumed that the frequency is directly proportional to the speed and the speed is accordingly presented as a frequency in this plot. The PQ-controlled system can be seen as a base case without any inertia support. For this case, the frequency nadir is found

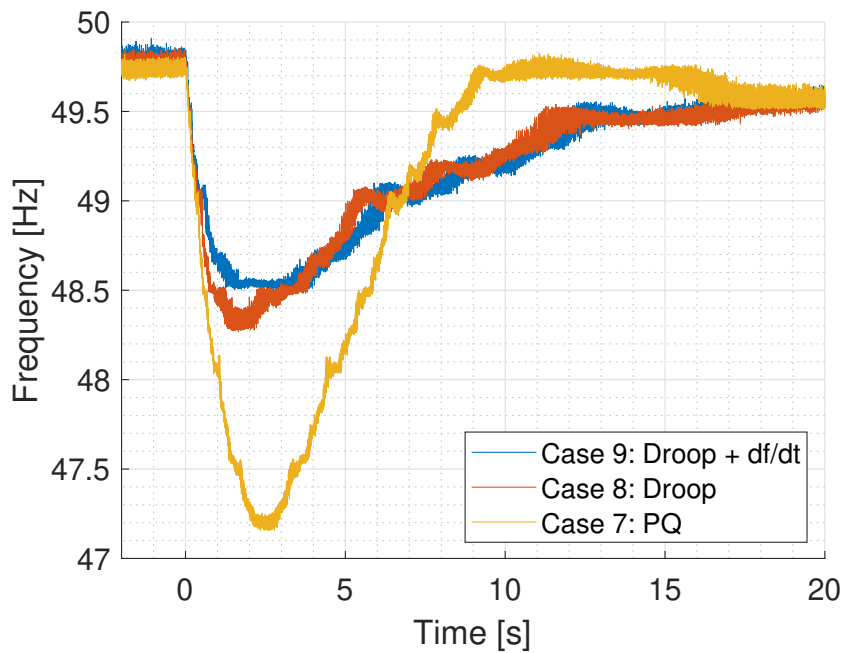


Figure 5.1: Frequency for the three different control schemes.

to be 47.2 Hz at 2.46 seconds after the step. With the droop enabled in the control system, the nadir is reduced with 42.3 % to 48.3 Hz after 1.7 s. When both droop and df/dt is enabled, the frequency nadir is reduced by 50.0 % compared to the base case, resulting in a nadir of 48.5 Hz. For the case with droop and df/dt, the speed stays at the bottom point from 1.5 s until 3.5 s it is therefore, harder to estimate the time that frequency nadir occurs, but it is assessed that the nadir occurs at 2.6 s as this is the middle point of the flat area. The frequency nadirs are summarised in Table 5.3. These results indicate that the df/dt term contributes less to the frequency support than the droop term. This is discussed further in Chapter 5.3.

Table 5.3: Frequency Nadir for the Different Control Schemes.

| Case | Freq. nadir | Time | % reduction |
|--------------------|-------------|-------|-------------|
| PQ | 47.2 Hz | 2.5 s | 0 % |
| PQ + Droop | 48.3 Hz | 1.7 s | 42.3 % |
| PQ + Droop + df/dt | 48.5 Hz | 2.5 s | 50.0 % |

It can be observed that the initial ROCOF seems to be unaffected by the added inertia loops in the control system. A close up of the initial frequency drop is presented in Appendix A.1, Figure A.1. It is found that up to around 400 ms the frequencies for the three different cases fall with the same rate. After this, they start to diverge, and df/dt method flattens out the fastest. Even though there is a distinct difference in the frequency nadirs for the three methods, the settling time to the new steady-state is almost identical. The new steady-state is established after about 19 seconds with 49.6 Hz. Because the speed controller has a droop, this is lower than the initial value of 49.8 Hz. The base case is slightly underdamped and has a small overshoot up to 49.75 Hz while the droop and the droop plus df/dt is overdamped.

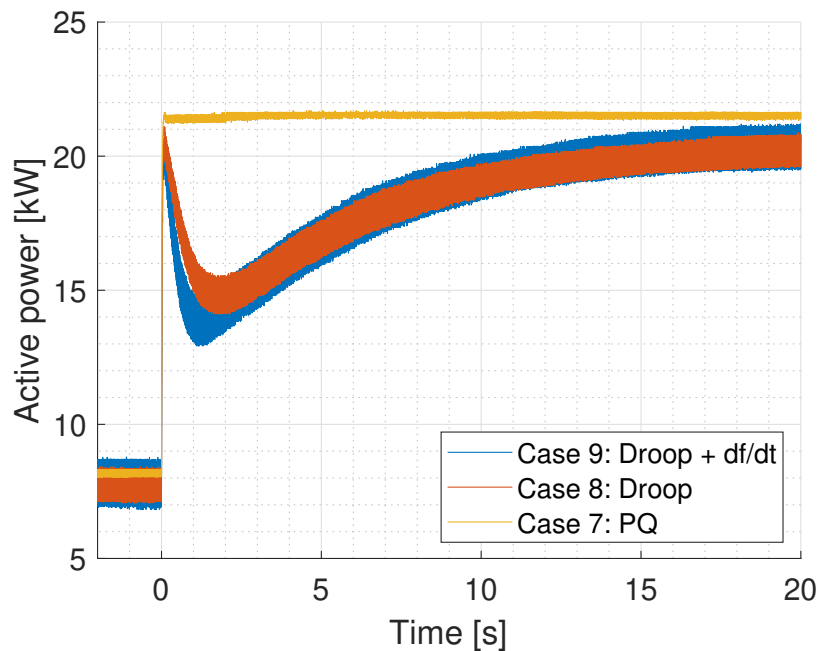


Figure 5.2: Active power delivered from the generator for the three different control schemes.

In Figure 5.2 the active power flow out from the generator is shown, while the flow from the converter is shown in Figure 5.3. For the base case, it is seen that generator deliver the whole step in active power. The new value for the active power flow is reached after 68 ms with 21.4 kW. This is better seen in the close-up of the power from the generator that is presented in Appendix A.2, Figure A.2. The peak active power delivery for the generator for the droop and the df/dt IE is almost as high as for the base case with peak values of respectively 21.1 kW and 20.9 kW. This is because of delay in the converter related to filtering of signals and time constants in regulators, and converter modulation makes the generator react faster than the converter.

This delay is reflected in the converter's active power shown in Figure 5.3. Here the converter with df/dt IE reaches the peak power delivery after 1.29 s with a value of 13.3 kW and the droop reaches peak power after 1.89 s with the value 12.39 kW. One can observe that the power delivered from the converter is the inverse of the generator's power. As the power from the converter increases, the power from the generator decreases. This is expected as the generator and converter are the only sources of active power in the system and if losses are neglected, the sum of these should equal to the active power delivered to the load. It is also observed that the initial value for the converter power output is higher for droop and df/dt IE with a value of 5.6 kW as opposed to the base case with 5 kW. This is due to the droop in the virtual inertia controller.

After reaching the peak, the converter's power output decreases to a new steady-state that should be higher than the initial steady-state due to frequency and power droop in the system. After 20 seconds the converter has still not reached its new steady-state. The active power from the converter beyond the 20 second time scale is shown in Appendix A.3, Figure A.3. It is found that for the droop the steady-state is reached after about 35 seconds with the value 6.2 kW. The

df/dt IE measurement is ended at 27 s before the steady-state is reached, but it is assumed to be similar for the droop as the droop constants in these two methods are identical.

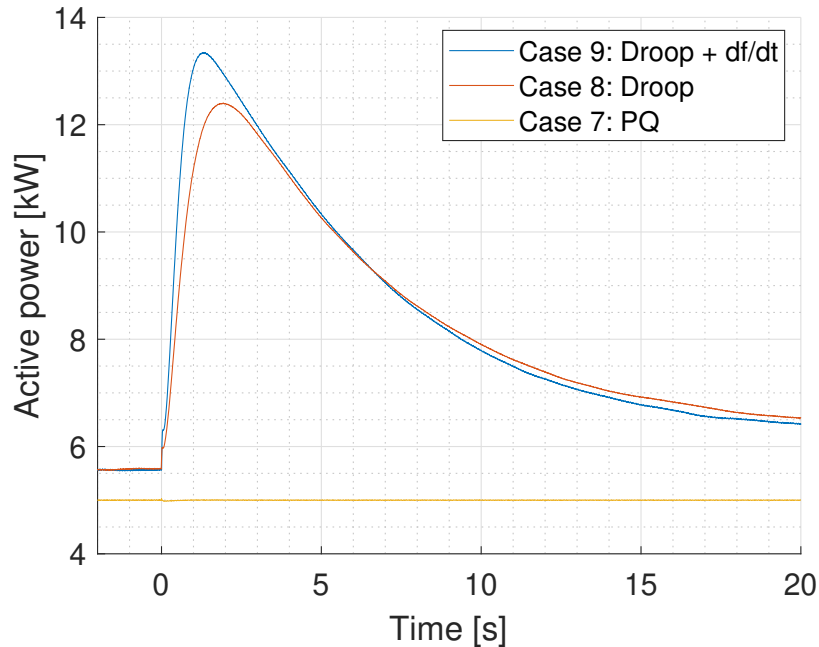


Figure 5.3: Active power delivered from the converter for the three different control schemes.

The measurements of the active power for the generator has a band. When zoomed in it can be seen that this is an oscillation with a frequency of roughly 50 Hz. The oscillations' amplitude is smallest for the base case with an amplitude of about 0.15 kW and largest for the df/dt IE with an amplitude of about 0.90 kW. These oscillations are discussed in Chapter 5.8.

It is found that both droop and the df/dt effectively help reduce the frequency nadir by injecting more active power into the grid. As a result, the converter has to be oversized or run at an operation point below rated power to deliver artificial inertia support. E.g., the converter injects a maximum of 7.7 extra kW in the case with df/dt IE. It is no problem in this case, as the converter is running at low load. If the converter is operating near rated power, the potential of the providing inertia would be limited by the rating of the converter.

5.3 Comparison of Droop Constant and df/dt Constant

To better understand the contribution of the droop and the df/dt branches in the virtual controller, the frequency response has been plotted for droop and df/dt separately. This is shown in Figure 5.4. This experiment is similar to the one described in Chapter 5.2 and the same step of 13.3 kW has been applied with identical initial loading of the system. The cases in this example correspond to the cases 7, 8 and 21 in Table 5.1. The case with pure df/dt control shows a frequency nadir of 47.85 Hz at the time 3.2 seconds after the step. It can be seen that the droop control reduces the frequency nadir more than the df/dt. The droop control reduces the time of the frequency nadir and gives an overdamped response. On the other hand, the df/dt in-

creases the time of the nadir and results in an underdamped response with an overshoot. When the two branches are used together with similar gains, it is found that these effects cancel each other out and the time of the frequency nadir stays approximately constant. This can be seen by comparing PQ control with droop + df/dt in Table 5.3.

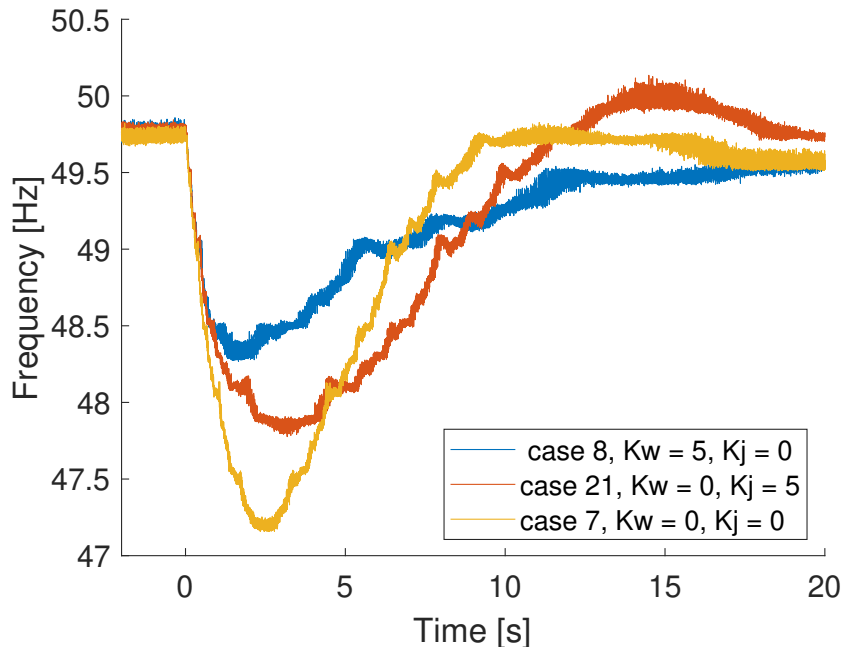


Figure 5.4: Frequency during a step in load with different droop gains.

5.4 Stability Limit for the Virtual Inertia Loop

To find the stability limits for the virtual inertia loop, an experiment was performed where the droop and the df/dt constants were increased from the base case with 5 in each branch. The droop and the df/dt were tested individually, meaning that one of them was kept at the initial value of 5 while the other was increased with 1 for each test. These experiments correspond to case number 30 to 42 in Table 5.1. Figure 5.5 and 5.6 show the electric frequency during a step in the load of 13.3 kW. In Figure 5.5, the droop constant was increased, and the df/dt constant was increased in Figure 5.6. For easier readability, some of the cases have been omitted in these plots. The remaining cases can be found in Appendix A.4, Figure A.4 and A.5.

It was found that increasing the gains gives an increased total harmonic distortion (THD) in the current from the converter. The THD for selected cases is presented in Table 5.4 and 5.4. The THD was estimated by looking at the current in phase A before the step in load was applied. The fast Fourier transform analysis tool in the Simscape Specialised Power System library in Simulink was used to calculate the THD. A picture of the FFT analysis on case 35, which had the highest THD of all the cases presented here, is included in Appendix A.5, Figure A.6.

Figure 5.5 shows that increasing the droop gain above 5 provides improved frequency support, but the benefit is diminishing. These results are summarised in Table 5.4. Increasing the droop constant, K_w , to 7 the reduction in frequency nadir is increased to 57.7 %. With the droop

constant is increased to 9, the frequency nadir is reduced by 69.2 %. Further increasing the droop constant yields no more improvement. The improved frequency response comes with the cost of increased THD on the current.

Table 5.4: Frequency Nadir and THD on Current From Converter for Different Droop Gains.

| Case | K_w | Freq. nadir | Time | % reduction | THD |
|------|-------|-------------|-------|-------------|---------|
| 7 | 0 | 47.2 Hz | 2.5 s | 0 % | 2.20 % |
| 9 | 5 | 48.5 Hz | 2.5 s | 50.0 % | 4.36 % |
| 38 | 7 | 48.7 Hz | 2.3 s | 57.7 % | 5.88 % |
| 40 | 9 | 49.0 Hz | 2.2 s | 69.2 % | 10.56 % |
| 42 | 11 | 49.0 Hz | 2.2 s | 69.2 % | 17.98 % |

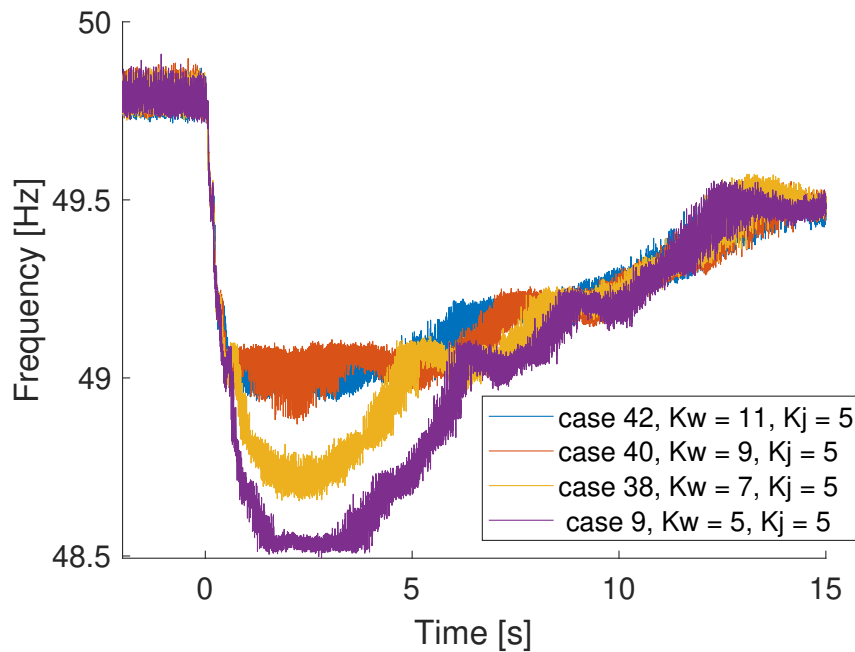


Figure 5.5: Frequency during a step in load with different droop gains.

Table 5.5: Frequency Nadir and THD on Current From Converter for Different df/dt Gains.

| Case | K_j | Freq. nadir | Time | % reduction | THD |
|------|-------|-------------|-------|-------------|---------|
| 7 | 0 | 47.2 Hz | 2.5 s | 0 % | 2.20 % |
| 9 | 5 | 48.5 Hz | 2.5 s | 50.0 % | 4.36 % |
| 31 | 7 | 48.6 Hz | 2.7 s | 53.8 % | 6.26 % |
| 33 | 9 | 48.6 Hz | 2.9 s | 53.8 % | 10.86 % |
| 35 | 11 | 48.7 Hz | 3.1 s | 57.7 % | 19.58 % |

The results from the testing of increased df/dt constant is presented in Figure 5.6 and is summarised in Table 5.5. As for the droop constant, improved frequency response is shown when

the df/dt constant is increased but at the cost of increasing THD. The results are also diminishing here. The THD increases much more than what is gained by on the frequency response. This experiment was also performed with a df/dt gain of 12, resulting in a current so deformed that it was deemed unstable. This current can be seen in Appendix A.6, Figure A.7.

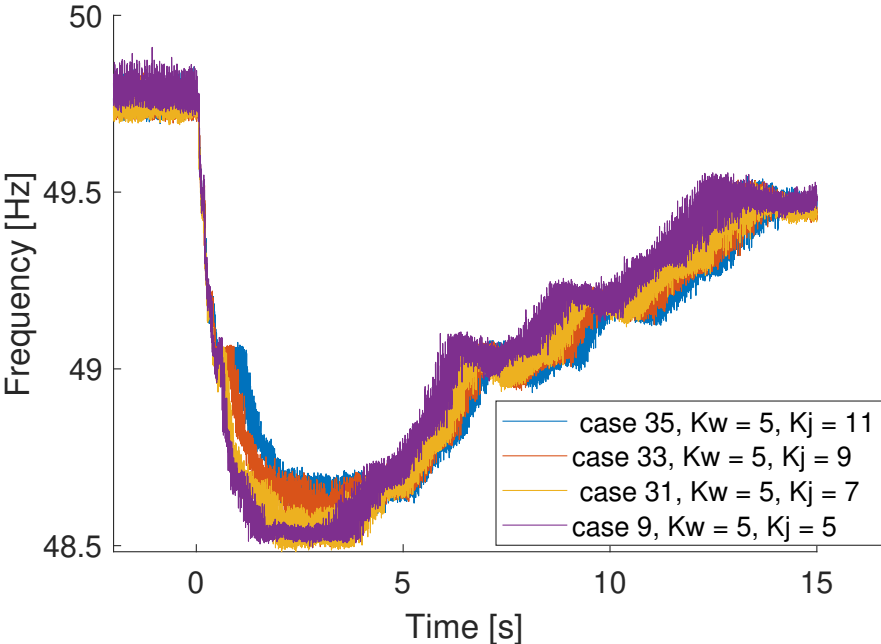


Figure 5.6: Frequency during a step in load with different df/dt gains.

It is found that the stability limit for the droop is a gain of 11 if the df/dt gain is set at 5. Similarly, the limit for the df/dt is a gain of 11 when the droop gain is set at 5. It is also found that increasing the gains results in a higher THD on the output current.

5.5 Comparison of Different Initial Load Scenarios

To investigate how the initial load situation affects the system's frequency response, a series of experiments were performed where the active and reactive load sharing between the converter and generator was varied. These cases correspond to cases 1 - 18 in Table 5.1, but only a selection is presented here. In Figure 5.7, the frequency is shown for a situation where the active load is shared between the generator and converter, and the reactive power from the converter is varied between -8, 0 and +8 kVAr. The initial active power from the generator is 7.6 kW and 5.6 kW from the converter. In Figure 5.8, the generator runs no-load, and the converter has an initial active power delivery of 14.2 kW. In both cases, a step of 13.3 kW is applied at time 0 s. For the cases here, the converter is controlled with droop control. The same experiments were performed with PQ and droop + df/dt control, but is not discussed further as the results are similar to those of the droop control experiments. The active power from the generator and converter for these cases are presented in Appendix A.7, Figures A.8, A.9, A.10 and A.11.

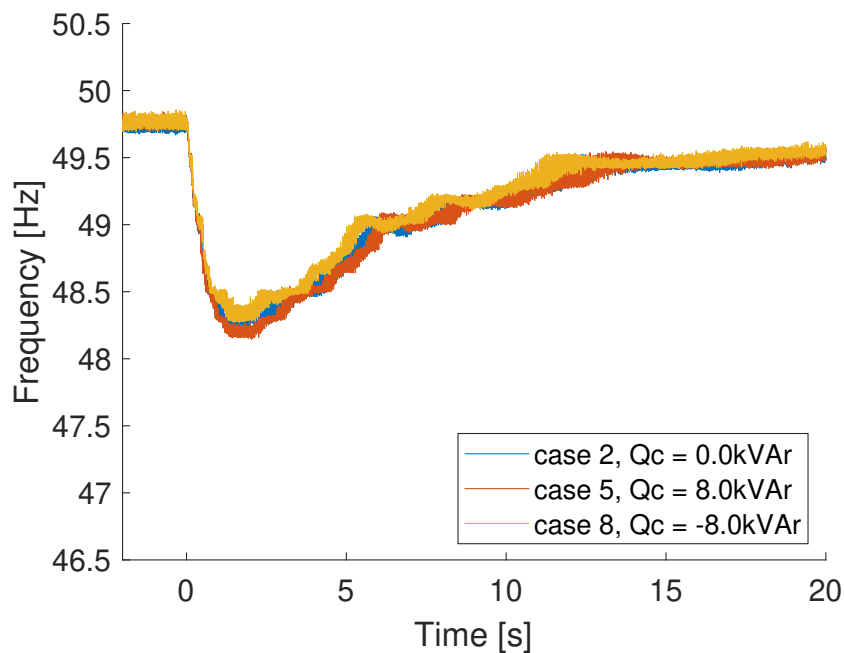


Figure 5.7: Frequency during a step in load with positive, negative and zero reactive power flow out from the converter. The active power load is shared between the generator and converter.

Figure 5.7 shows that the frequency differences between the different reactive power loading are small but noticeable. Positive reactive power from the converter gives a frequency nadir of 48.20 Hz, zero active power gives a frequency nadir of 48.27 Hz and negative reactive power results in a minimum frequency of 48.34 Hz. This is reflected in the active power delivered from the converter as shown in Appendix A.7, Figure A.9. Here the maximum active power delivered is highest for the case 5 with a peak power output of 13.12 kW, while case 8 has the lowest with 12.39 kW, and case 2 in between with a peak power output of 12.74 kW. Other than some difference in magnitude, the curves follow the same trend.

For the cases with the generator in no-load, a similar result is found. The lowest frequency tran-

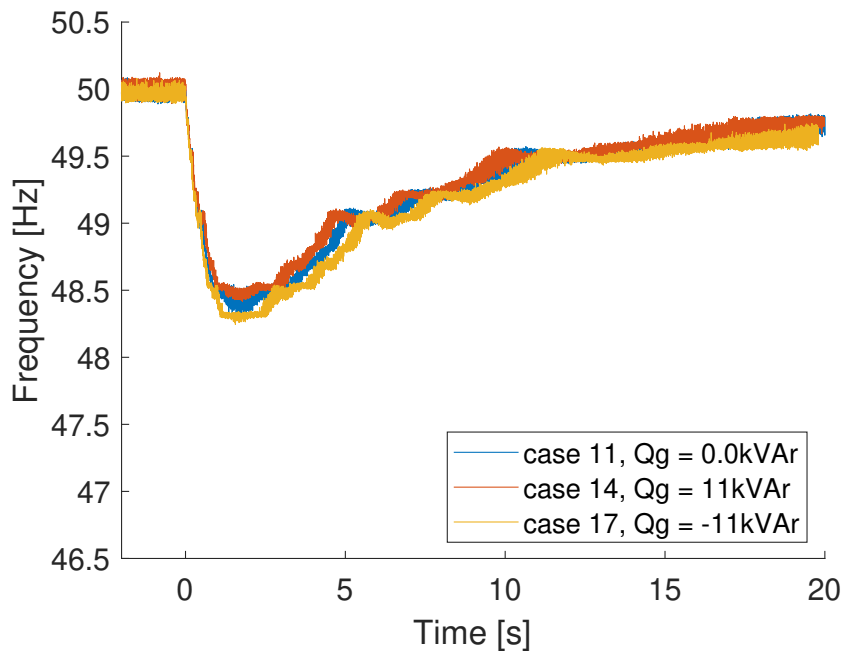


Figure 5.8: Frequency during a step in load with positive, negative and zero reactive power flow out from the generator. The generator is running no-load.

sient is found for case 17, where the reactive power delivered from the generator is negative. This gives a positive reactive power flow from the converter. Here the frequency nadir is found to be 48.31 Hz. For case 11, the frequency nadir is read to be 48.40 Hz Hz, while it is 48.47 Hz for case 14. It is also found that the active power is quite similar between the different reactive power flows. For case 11 the converter's peak active power is found to be 21.42 kW, for case 14 it is 20.97 kW and for case 17 it is 21.95 kW.

It is observed that the frequency drop during the load step is slightly increased when the converter is delivering reactive power. This is seen both for the case with shared active power and for the case with generator running in no-load. A possible reason for this might be that the extra reactive power added by the converter increases the voltage during the transient period relatively to the case when the converter is consuming reactive power. When the voltage over the resistance is higher, the step in active power is also higher, which results in a higher frequency deviation.

5.6 Comparison of Load Increase and Load Rejection

A large majority of the cases that was performed has been with a step up in load. This was because it was attempted to change as little as possible between each experiment, preferably only one variable, to make each experiment comparable. If the load is increased, the frequency will fall and vice versa. This experiment investigates the hypothesis that a load increase and decrease of the same magnitude would give the same frequency response, only in different directions. In Figure 5.9, a plot is presented for case 42 and case 43. For case 42 the system started at low load and stepped up to a higher load, in case 43 the initial conditions are at that high load, and the same step is applied in the opposite direction. As expected, it is observed

Table 5.6: Initial and Peak Frequency for Case 42 and Case 43.

| Case | Initial Frequency | Peak Frequency | Δf |
|------|-------------------|----------------|------------|
| 42 | 49.78 Hz | 49.00 Hz | 0.78 Hz |
| 43 | 49.73 Hz | 50.51 Hz | 0.78 Hz |

that the frequency dynamics are symmetrical for the two cases. The initial frequencies and peak frequencies were recorded and is presented in Table 5.6. It is found that the Δf frequencies are identical within the measurement accuracy of these experiments. The reason that the initial frequencies differ is due to the speed droop on the generator.

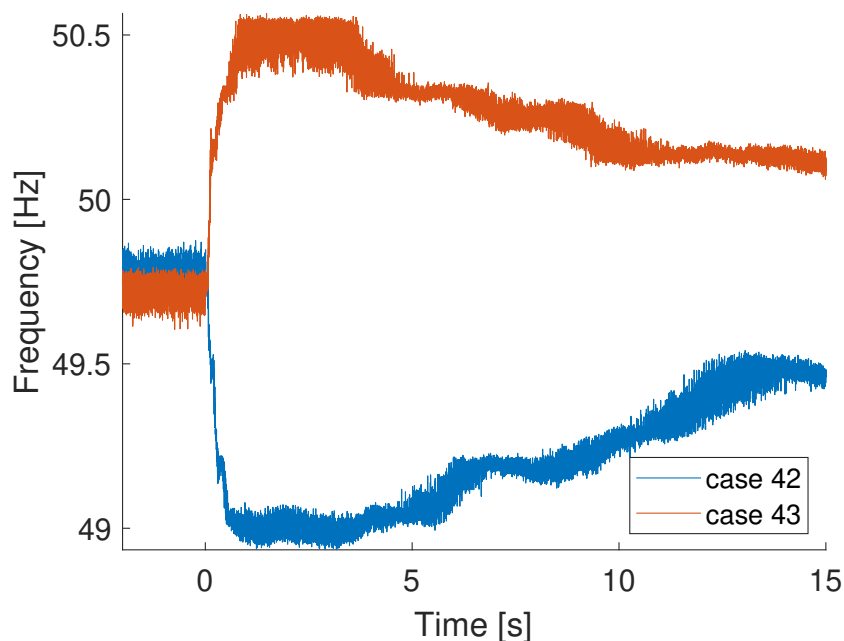


Figure 5.9: Frequency during a step up, and step down of a load of 13.3 kW.

5.7 Drop in DC-Voltage

Three experiments were performed to see how a drop in voltage on the DC-side of the converter would affect the system. The converter supplied 5.6 kW and drew 8.0 kVAr, while the DC-voltage reference changed from 700 V to 650, 600 and 550 V in the different runs. This is shown in Figure 5.10a. Even though the voltage was changed in a step, the voltage drop is dropping like a ramp. This is because the capacitors need time to charge out. In Figure 5.10b, the active power from the converter is shown during this drop in DC-voltage. It can be seen that active power is unaffected from the drop in DC-voltage.

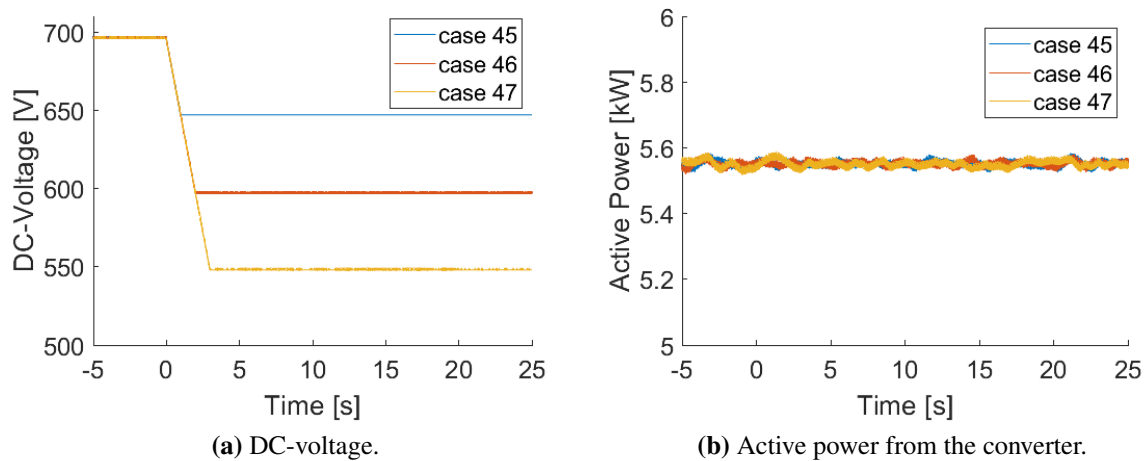


Figure 5.10: Active power from the converter and voltage during a drop in voltage on the DC-side of the converter.

5.8 Active Power Oscillations

In many of the experiments, the active power measurements for the generator oscillates. An example of this is shown in 5.11. The oscillation frequency is found to be 48.78Hz. The frequency for the voltage in this experiment was 49.13 Hz in this example. Thus, it is assumed that these oscillations occur at the electric fundamental frequency.

These measurements are done with the processor card presented in Chapter 3.4.2, which utilises the two-wattmeter method. The two-wattmeter method is valid as long as the sum of currents is equal to zero, in other words as long as no current is flowing in the neutral conductor. The generator is connected in star with a floating neutral point, and the grid side of the transformer is delta connected, meaning that there is no neutral current in this circuit. Hence, the criteria for the two-watt meter method is fulfilled.

It was initially found that experiments running without the converter were much less oscillatory than the experiments with the converter. Therefore, it was first assumed that the active power oscillations resulted from the interaction between the generator and the converter. It was later discovered that the longer the system had been running, the more oscillatory the measurements were. Of practical reasons, the experiments with the converter were performed continuously

back-to-back and the run time of most of these experiments were therefore relatively long.

It was suspected that the oscillations resulted from thermal conditions in the control cabinet for the motor/generator set. This cabinet is quite packed with components, and the DC-motor drive has relatively large losses. As a result, the control cabinet gets hot when operating for longer periods of time. After a discussion with research scientist Kjell Ljøkelsøy, it was concluded that the temperature rise most likely causes DC-offsets in the LEM sensors. This explanation fits well with the frequency of the oscillation. If one of the measured voltages or currents has a dc-offset compared to the other, this will result in an oscillation with the same frequency as the system's fundamental frequency.

To get curves that are easier to read these oscillations could have been filtered out in post-processing using a notch filter that filters out the oscillations' frequency. This was not attempted due to time restrictions, but it should work in theory without significantly affecting the end result.

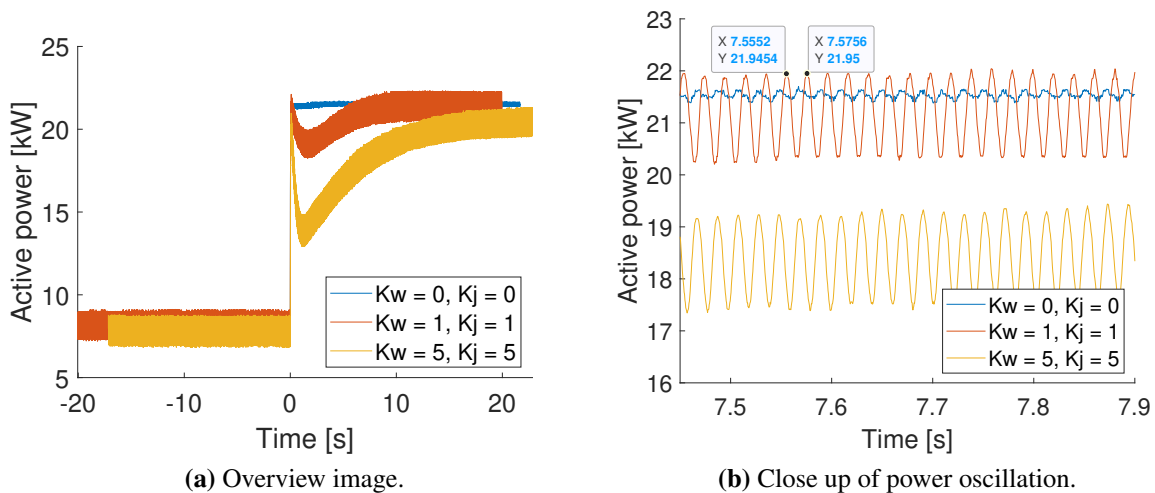


Figure 5.11: Active power for three different cases of droop and df/dt gains.

Results and Discussion - Parameter Estimation Experiments

6.1 Base Values for the Per-Unit Calculations

For the calculation of parameters in the per-unit system, the base values have to be defined. The per-unit system chosen here is the "power system base quantities" as defined in [7, pp. 598 - 599]. The base values are presented in Table 6.1. The base voltage is chosen to be reduced nominal voltage of 400 V line to line as explained in 3.3.1. Similarly, the apparent power base is selected to be the adjusted nominal power for the generator with the reduced nominal voltage. The base current is the nominal current as given by the nameplate. [7] does not define the base values for the field voltage and current. For these, the base values have been selected to be the voltage and current that yields 400 V terminal voltage in open circuit at rated speed. The impedance base is calculated with the base voltage and apparent power.

Table 6.1: Base Values for the Estimation of Parameters.

| S_b | V_b | I_b | $V_{f,b}$ | $I_{f,b}$ | Z_b |
|----------|-------|-------|-----------|-----------|----------------|
| 66.5 kVA | 400 V | 96 A | 38.5 V | 6.14 A | 2.406 Ω |

6.2 d -axis Parameter Test

A load shedding test was performed to estimate the standard parameters of the d -axis of the Siemens-Schuckert synchronous generator. This was done by synchronising the generator to the electrical power grid, and establishing an initial loading of the generator such that the current could be assumed to be purely in the d -axis as explained in Chapter 2.5.1. This can be done in two ways, ensuring that the generator's active power is zero while supplying or drawing reactive power. To avoid saturation of the generator, the experiment was performed in under-excited operation. The initial load condition for the generator is presented in Table 6.2. Here the initial active power, reactive power, terminal voltage, armature current and field voltage is shown. With the given initial loading, the generator was disconnected from the grid. The DC-motor was also disconnected, simultaneously, to avoid the generator to accelerate and the speed

control to interfere with the voltage dynamics.

During this experiment, the DC-motor on the generator/motor-set was regulated by the speed controller with droop. The mechanical input to the generator was then controlled similarly to a governor in a power plant where adjusting the speed controller's setpoint would yield a new operating point. However, the minimum resolution of the speed controller was 1 rpm which resulted in steps of about 4 kW. The initial active power output is given to be approximately equal to zero in Table 6.2. This is because the speed regulation varied the DC motor's output depending on the slightly fluctuating grid frequency. The active power was varying between 0 kW and - 4 kW before the load shedding.

Table 6.2: Initial Loading of the Synchronous Generator for the d -axis Test, Underexcited Operation.

| P | Q | V_t | I_a | V_f |
|----------------|-----------|-------|-------|--------|
| ≈ 0 kW | - 57 kVAr | 400 V | 84 A | 13.7 V |

At time zero the generator was disconnected from the grid and dc-motor was shut off. This was done manually by pressing the off-button on the dc-motor drive and the switch for the generator's breaker simultaneously. The generator was immediately changed from the initial loading to an open circuit no-load situation. A plot of the instantaneous values of the terminal voltages during this event is presented in Appendix B.1, Figure B.1. It can be seen that the terminal voltage fell after it was disconnected from the grid. This is because generator was running in underexcited operation. From the instantaneous terminal voltages the voltage peaks were found for each phase. These peaks were then plotted to find the three-phase voltage envelope. This envelope is shown in Figure 6.1.

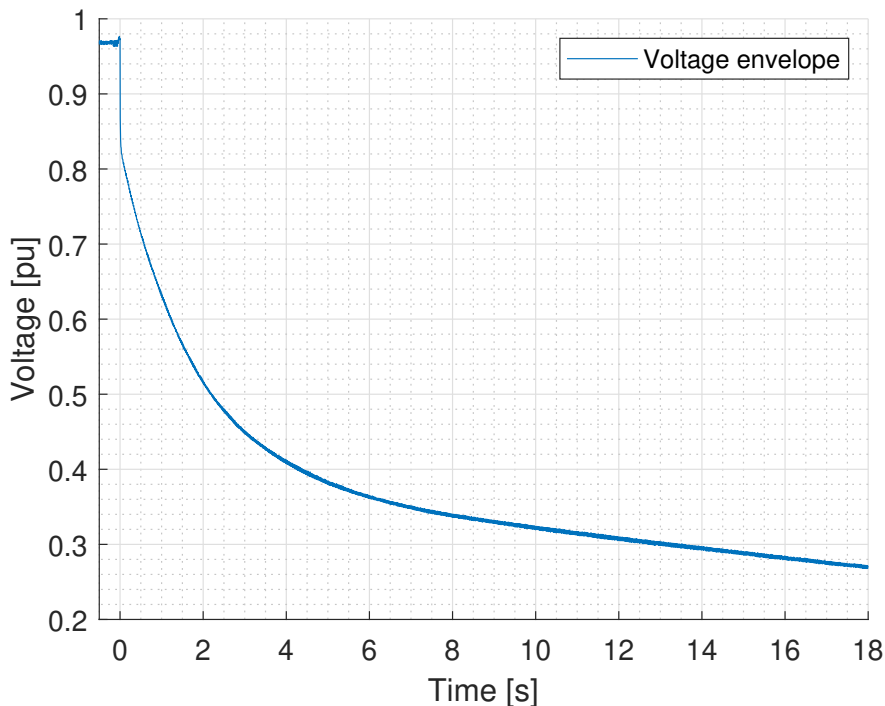


Figure 6.1: The envelope of the voltage during d -axis load rejection.

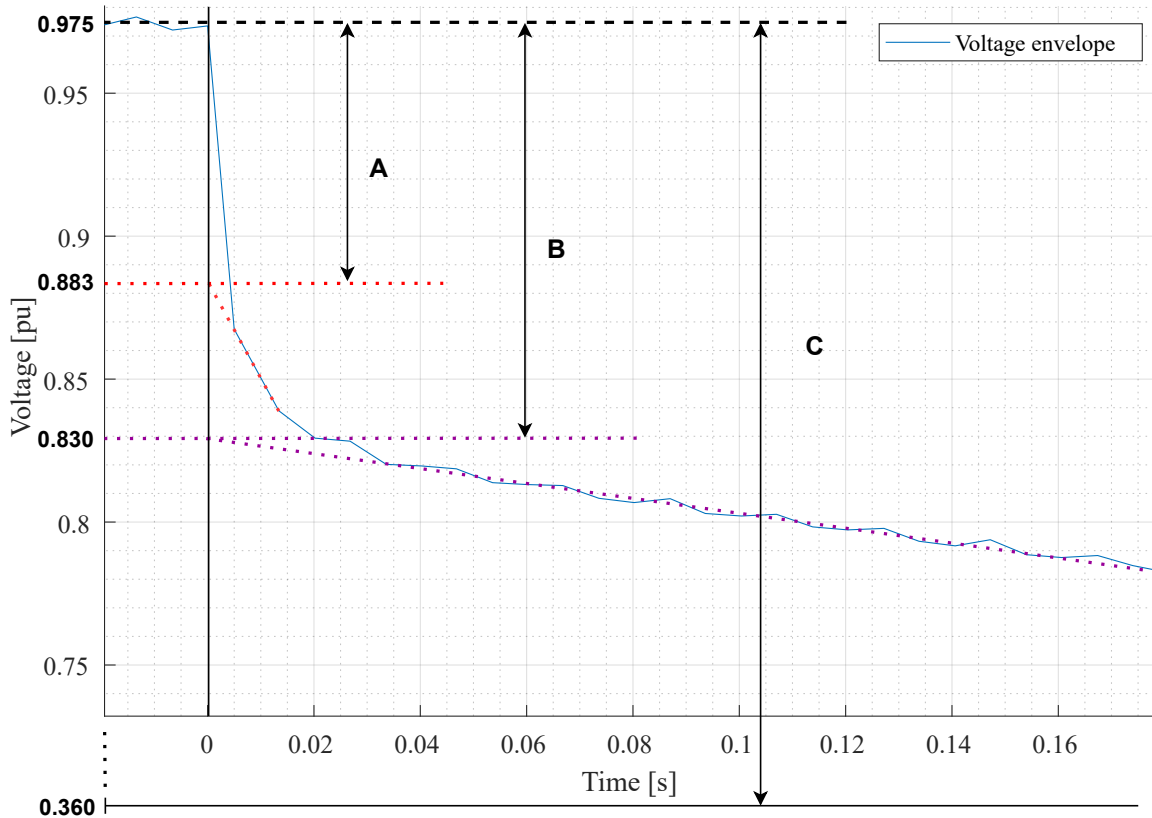


Figure 6.2: Close-up of the voltage envelope during load shedding.

In Figure 6.2, an amplification of the voltage envelope is shown for the first 0.18 seconds of the transient course. In this figure, two trend lines have been drawn. The purple trend line corresponds to the transient voltage, and the red line corresponds to the subtransient voltage. These lines have been chosen to be linear in the same way as performed in [27]. One could also find the trend lines by performing a regression analysis with a higher degree polynomial, but it was deemed that the trend lines were short enough that the readings would not be impacted significantly by choosing straight lines. By reading the values for where these trend lines meet the y-axis, it is possible to calculate the three constants A , B and C . With these constants and Equations 6.1 - 6.3 the steady-state, transient and subtransient d -axis reactances were estimated. This method is based on [26] and [27], and is also described in Chapter 2.5.1. As the active power is approximately equal to zero, the load angle is also zero, this causes the terminal voltage to be in phase with the q -axis, and the current can be assumed to be placed in the d -axis as shown in Chapter 2.5.1, Figure 2.11. Therefore, the current used in these calculations is the armature current given in Table 6.2. The base values are given in Chapter 6.1, Table 6.1.

$$x_d = \frac{C}{i_{d0}} = \frac{0.975 - 0.360}{0.875} = 0.7029 \text{ pu} \quad (6.1)$$

$$x'_d = \frac{B}{i_{d0}} = \frac{0.975 - 0.830}{0.875} = 0.1657 \text{ pu} \quad (6.2)$$

$$x_d'' = \frac{A}{i_{d0}} = \frac{0.975 - 0.883}{0.875} = 0.1051 \text{ pu} \quad (6.3)$$

To estimate the d -axis subtransient and transient open-circuit time constants, the field current development was used. The complete field current transient is presented in Appendix B.1, Figure B.2. A zoomed-in version is presented in Figure 6.3. A linear trend line was chosen to find the peak transient field current, and the value is found to be 0.79 pu. With the definition of the time constant, the transient open-circuit time constant, T_{do}' , is found to be 1.8 s. The subtransient time constant was estimated in a similar way. This is shown in Figure 6.4. The subtransient open-circuit time constant, T_{do}'' , is evaluated to be 0.011 s.

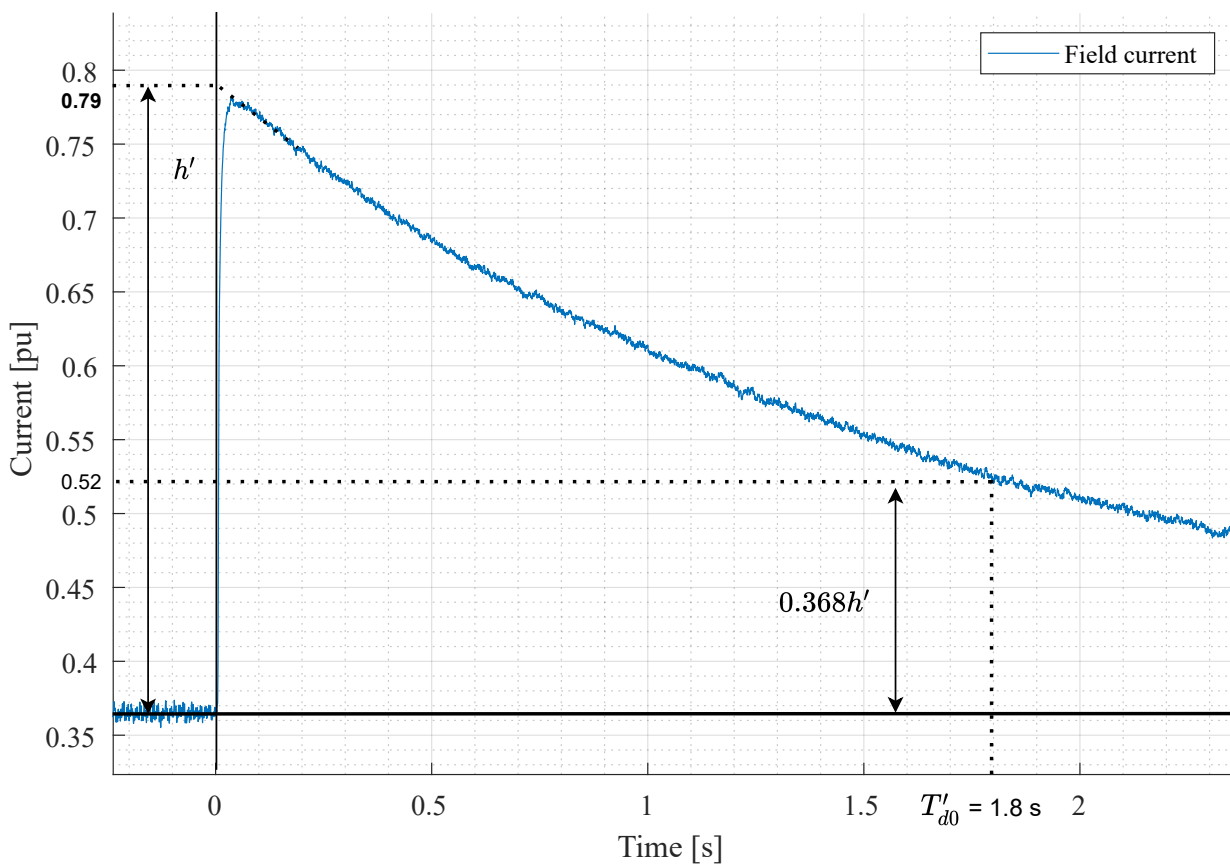


Figure 6.3: Amplification of the field current for the estimation of T_{do}' .

The tests performed here does not allow for the determination of the short-circuit time constants, but these can be calculated with the known relationship between the open and short-circuit time constants. This is done in Equation 6.4 and 6.5, which are derived in [7, p. 139].

$$T_d'' \approx T_{do}'' \frac{x_d''}{x_d'} = 0.011 \cdot \frac{0.1051}{0.1657} = 0.007 \text{ s} \quad (6.4)$$

$$T_d' \approx T_{do}' \frac{x_d'}{x_d} = 1.8 \cdot \frac{0.1657}{0.7029} = 0.424 \text{ s} \quad (6.5)$$

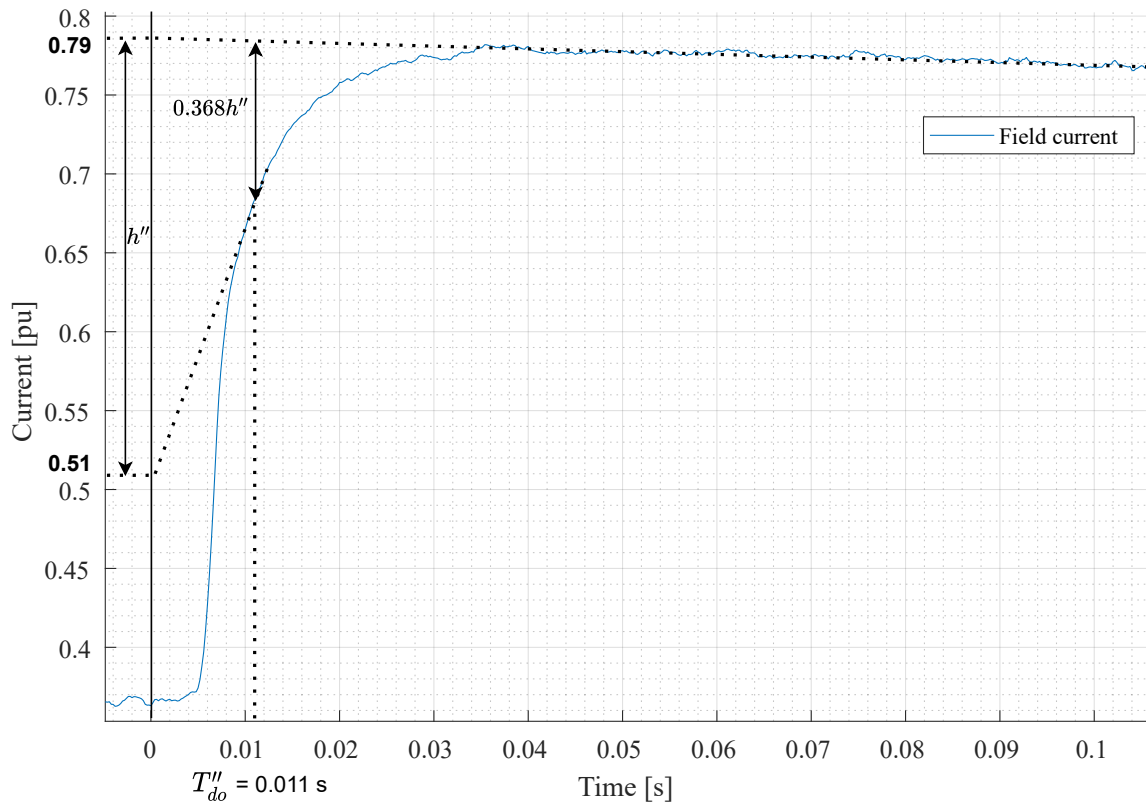


Figure 6.4: Amplification of the field current for the estimation of T''_{do} .

An assumption for this method to be valid is that the generator's speed is constant. This because the armature voltage is proportional to both the field current and the generator's speed. This assumption was obviously not true, but as a check of how fair this assumption was, the generator's speed was recorded. The plot of the speed shown in Appendix B.1, Figure B.3. The largest time constant in the d -axis is 1.8 seconds, for this reason, the speed at 1.8 s and the initial speed is presented in Table 6.3. It is found that the reduction during this period is 3.44 %. As the mechanical time constant is much higher than the electrical time constants, this approximation is deemed viable, but the speed reduction will slightly impact the results. In general, this method is more accurate for machines with large mechanical inertia and less accurate for machines with less inertia.

Table 6.3: Speed Reduction of the Generator During d -axis Load Rejection.

| Initial speed | Speed at 1.8 s | Percentage reduction |
|---------------|----------------|----------------------|
| 997.8 rpm | 963.5 rpm | 3.44 % |

6.3 q -axis Parameter Tests

To estimate the q -axis standard parameters for the synchronous generator, two tests were performed. These are the q -axis load rejection test and the arbitrary axis load rejection test. The results from these tests are presented in the following subchapter.

6.3.1 q -axis Load Rejection Test

The q -axis load rejection test was performed with an initial load condition such that the armature current was aligned with the q -axis. In this experiment, the DC-motor was controlled with torque-control as this gave a more precise control over the active power than the speed regulation. The generator was synchronised to the electric power grid, and the active and reactive power output was adjusted such that the load angle, δ , was approximately the same as the phase angle. This ensured that current was aligned with the q -axis as shown in the phasor diagram presented in Chapter 2.5.2, Figure 2.14. The initial loading of the generator is presented in Table 6.4. The generator was operated in underexcited mode to make the current lead the terminal voltage.

Table 6.4: Initial Loading of the Synchronous Generator for the q -axis Test, Under-Excited Generator.

| P | Q | V_t | I_a | V_f | δ | ϕ |
|---------|------------|-------|-------|--------|----------|--------|
| 40.4 kW | - 8.5 kVAr | 400 V | 60 A | 38.8 V | 12.0° | 11.7° |

When the generator's initial loading was established, the generator and the DC-motor were disconnected simultaneously. This was done at time zero seconds. The terminal voltage was recorded, and the field current was recorded. The complete three-phase instantaneous voltage can be found in Appendix B.2.1, Figure B.4. The voltage envelope was plotted from the three-phase voltage and is presented in Figure 6.5.

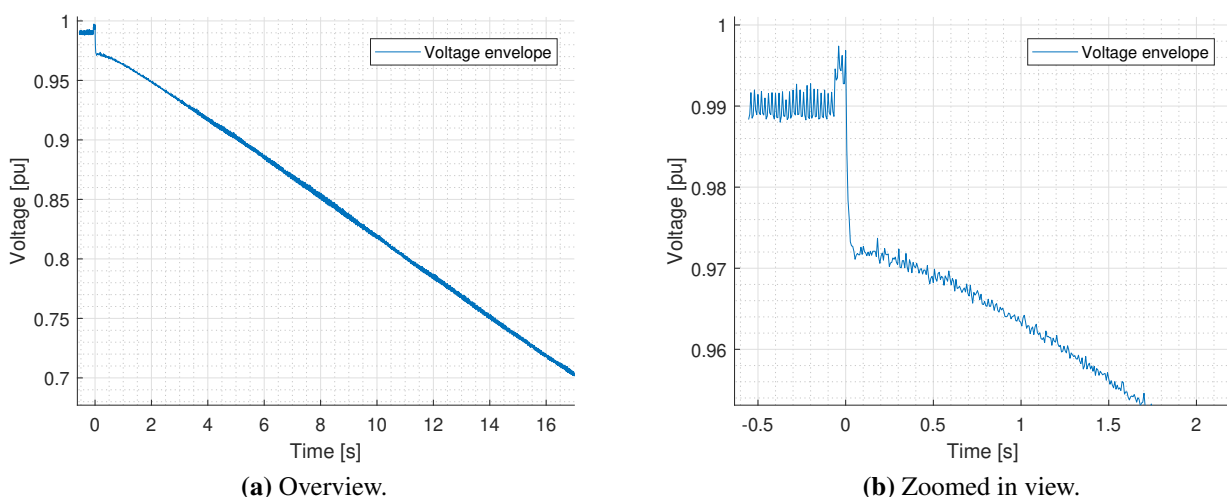


Figure 6.5: Voltage envelope of the terminal voltage during q -axis load rejection.

As the field voltage had to be kept very close to 1 pu to obtain the desired loading of the generator, the voltage dynamics after the load rejection was minimal compared to the d -axis

test and the arbitrary axis test. The initial voltage drop was less than 0.02 pu. With the small transient in terminal voltage, the generator's deceleration dominates the voltage development in this test. It would have been better to run this experiment with a larger load angle and phase angle. In this case, the generator was running at maximum active power, and it was not possible to increase the load angle by increasing the active power output. Another way to increase the load angle is to reduce the field voltage. This would also increase the generator's reactive power consumption and increase the phase angle. Due to the small voltage drop, this test was deemed inconclusive to estimate parameters for the q -axis. As the arbitrary load rejection test gave better results (see Chapter 6.3.2) further attempts with the q -axis load rejection test was not performed.

6.3.2 Arbitrary Axis Load Rejection Test

In the arbitrary axis load rejection test, the only condition is that the current consist of both q - and d -axis components. In this experiment, the generator's initial loading was inspired by the arbitrary axis test performed in [27], and a similar ratio between the reactive power and active power was chosen. The initial load is presented in Table 6.5.

Table 6.5: Initial Loading of the Synchronous Generator for the Arbitrary Axis Load Rejection Test, Overexcited Generator.

| P | Q | V_t | I_a | V_f | δ | ϕ |
|---------|-----------|-------|-------|--------|----------|--------|
| 30.5 kW | 18.6 kVAr | 400 V | 52 A | 48.6 V | 8.6° | -31.4° |

When the desired load condition was obtained the generator, and the DC-motor were simultaneously disconnected, with the same procedure as the other parameter estimation tests. The simultaneous voltages of the three phases and the load angle was recorded during this event. The instantaneous voltage for the three phases is shown in Appendix B.2.2, Figure B.5. The voltage was projected onto the d -axis by multiplying the voltage with $\sin(\delta)$, and the three-phase voltage envelope was found. The d -axis armature voltage envelope is plotted in Figure 6.6b

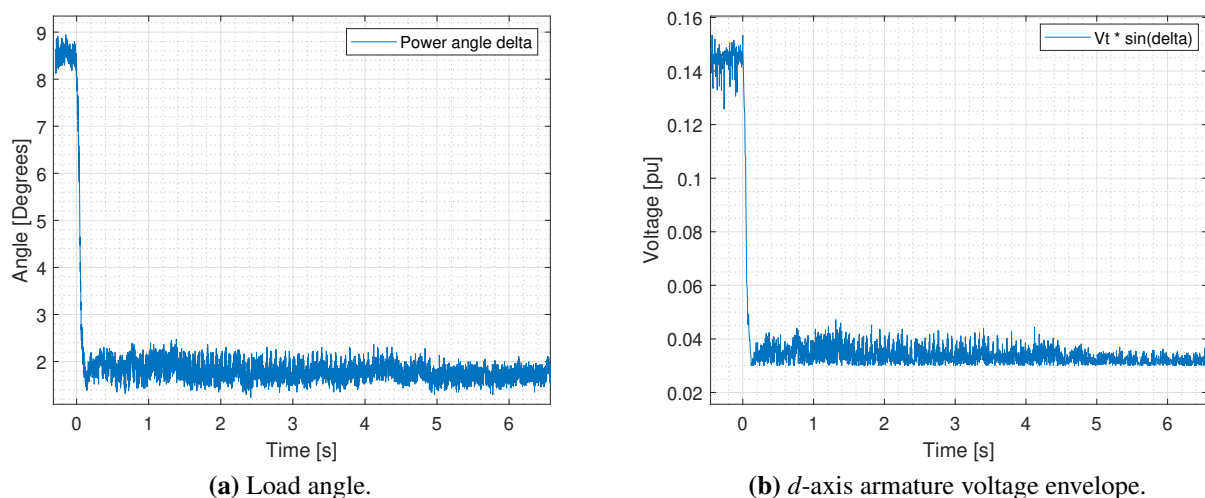


Figure 6.6: Results from the arbitrary axis parameter test.

and the load angle is plotted in Figure 6.6a. It should be noted that the voltages and the load angle were recorded with two different oscilloscopes, and the synchronising of these signals were done manually.

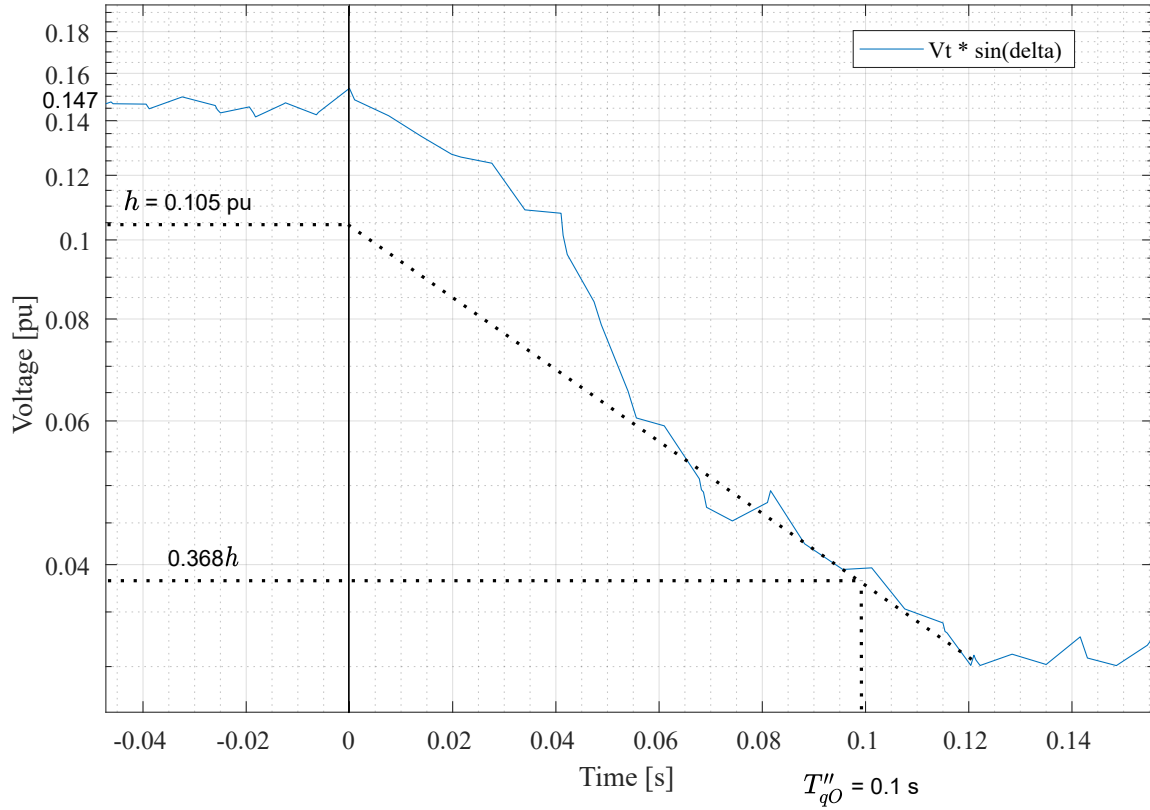


Figure 6.7: Amplification of the d -axis armature voltage envelope plotted on a semilogarithmic scale.

An amplified version of the voltage envelope is shown in Figure 6.7. This figure is plotted on a semilogarithmic scale as done in [27]. The initial d -axis voltage was found from the voltage envelope, and a trend line was drawn based on the subtransient d -axis voltage to find the initial subtransient value. The steady state and subtransient reactances are found with Equation 6.6 and 6.7. The initial q component of the armature current was found by multiplying the initial armature current with the cosine of the sum of the phase angle and the load angle.

$$x_q = \frac{(V_t \cdot \sin \delta)_0}{I_{q0}} = \frac{0.147}{0.4150} = 0.3542 pu \quad (6.6)$$

$$x_q'' = x_q - \frac{(V_t \cdot \sin \delta)_0''}{I_{q0}} = 0.3542 - \frac{0.105}{0.4150} = 0.1012 pu \quad (6.7)$$

The subtransient open-circuit time constant for the q -axis, T_{q0}'' , is read from Figure 6.7. This time constant corresponds to when the subtransient d -axis has fallen to 36.8 % of the initial subtransient voltage and is found to be 0.1 s. The short-circuit subtransient q -axis time constant is calculated by the formula given in Equation 6.8 [27].

$$T_q'' \approx T_{q0}'' \frac{x_q''}{x_q} = 0.1 \cdot \frac{0.1012}{0.3542} = 0.029 s \quad (6.8)$$

6.4 Summary and Discussion of Parameter Estimation Results

The results of the parameter estimation are summarised in Table 6.6. The d -axis parameters was estimated with the d -axis load rejection test presented in Chapter 6.2, and the q -axis parameters was estimated with the arbitrary axis load rejection test presented in Chapter 6.3.2. In this table, the measured armature resistance is also included, for details concerning the resistance see Chapter 4.1. For comparison, the classical synchronous reactance as defined for the round-rotor machine in [38, pp. 578-579] was calculated. The calculation was based on the open circuit characteristics (OCC) and the short circuit characteristics (SCC) as measured by [25]. The curves for the OCC and SCC is included in Appendix B.3, Figure B.6. The synchronous reactance, x_s , is based on the air-gap line and is, therefore, the unsaturated reactance. Armature resistance is not accounted for. The unsaturated value was calculated because the d -axis reactance was estimated for an unsaturated load condition. The x_d and x_s are therefore comparable and x_s can be used as a sanity check for the parameter estimation.

Table 6.6: Summary of the Electrical Parameters for the Siemens-Schuckert Synchronous Machine. Per-unit values calculated with the base values presented in Chapter 6.1.

| Parameter | Estimated Value | Values in SI-units |
|------------|-----------------|--------------------|
| R_a | 0.0236 pu | 56.9 m Ω |
| x_s | 0.7303 pu | 1.757 Ω |
| x_d | 0.7029 pu | 1.691 Ω |
| x'_d | 0.1657 pu | 0.399 Ω |
| x''_d | 0.1051 pu | 0.253 Ω |
| x_q | 0.3542 pu | 0.852 Ω |
| x''_q | 0.1012 pu | 0.243 Ω |
| T'_d | 0.42 s | 0.42 s |
| T'_{do} | 1.80 s | 1.80 s |
| T''_d | 0.007 s | 0.007 s |
| T''_{do} | 0.011 s | 0.011 s |
| T''_q | 0.029 s | 0.029 s |
| T''_{qo} | 0.10 s | 0.10 s |

It is seen that the d -axis reactance is 3.75 % lower than the calculated x_s . Some of this difference might be due to the inaccuracy in the voltage measurements. As found in Chapter 4.5, the difference of the measured rms voltage between the oscilloscope and the multi-instrument was found to be 2.79 %. This inaccuracy will directly impact the calculated values of the reactances, as the estimated reactances are proportional to the measured armature voltages. Another source of error is that the value of the steady-state armature voltage for rated speed has been assumed to be proportional to the field voltage, this is true for a generator in steady-state and open circuit (when $E_q = V_t$) [7, p. 140]. However, this assumes non-saturated operation. From the OCC-curve, some saturation effect occurs for a phase voltage of 230 V. Other error sources can be the measurement of current, and that the values were read manually from the graphs with trend lines.

There is no alternative estimation of the q -axis reactances to compare the results with. It is suspected that the q -axis parameters have been estimated with less accuracy than the d -axis parameters because the arbitrary axis test depends on the load angle measurement, which has a higher amount of noise than the voltage measurements. However, it is observed that the subtransient q -axis reactance is approximately the same as the estimated subtransient d -axis reactance. This is as according to theory for a generator with full damper windings [7, p. 137]. This gives a reassurance to the accuracy of the arbitrary axis test. One source of error that could have been avoided in the arbitrary axis test is that the load angle and the voltages could have been recorded on the same oscilloscope to assure that the signals are correctly synchronised.

The only electrical standard parameter not estimated is the leakage reactance. According to Kothari [23, p. 502] and Fitzgerald [39, p. 256], the typical values for the leakage reactance is from 0.1 - 0.2 pu for the round-rotor machine. However, both authors also present the typical synchronous reactances in the same context in the range of 1 - 2 pu. Therefore, it is suspected that the given range for typical leakage reactance is strongly correlated to the given range for the synchronous reactance. [24] confirm that the typical values for leakage reactance for the salient-pole generator are in the range of 0.1 - 0.15 % of the synchronous reactance. Another thing to consider is that the leakage reactance must be smaller than the subtransient reactance. This can be seen from equation 6.9 [7, p. 136].

$$x_d'' = x_l + \frac{1}{\frac{1}{x_a} + \frac{1}{x_D} + \frac{1}{x_f}} \quad (6.9)$$

Where x_a is the armature reaction reactance, x_D is the reactance corresponding to flux path around damper winding, and x_f is the reactance corresponding to the flux path around the field winding.

The scope of this work was to estimate the standard electrical parameters. Saturation effects were not considered. However, for the saturation in the d -axis, the regular OCC can be used. The q -axis saturation curve is more complicated to find, but there exist methods that are not discussed here, for example, in [40].

6.5 Comparison of Simulated Load Rejection Tests with Laboratory Results

6.5.1 Simulation Model

A simulation model was made to compare with the laboratory results. An overview of the model is presented in Figure 6.8. The model consists of a synchronous machine, voltage and load angle measurements, a breaker and a stiff grid. The standard parameter pu synchronous machine in the Simscape specialised power system library was used. The generator have been implemented with the nominal values matching the base value as presented in Chapter 6.1, Table 6.1. The electrical parameters in the d - and q -axis and measured armature resistance as presented in Table 6.6 was used. Based on the discussion on the leakage reactance presented in Chapter 6.4, the leakage reactance was assumed to be 0.1 pu. The inertia for the motor/generator set was estimated in [25] to be 36.5 kgm². With the apparent power base of 66.5 kVA and a rated speed of 1000 rpm, the inertia constant can be calculated with Equation 6.10. The friction factor was

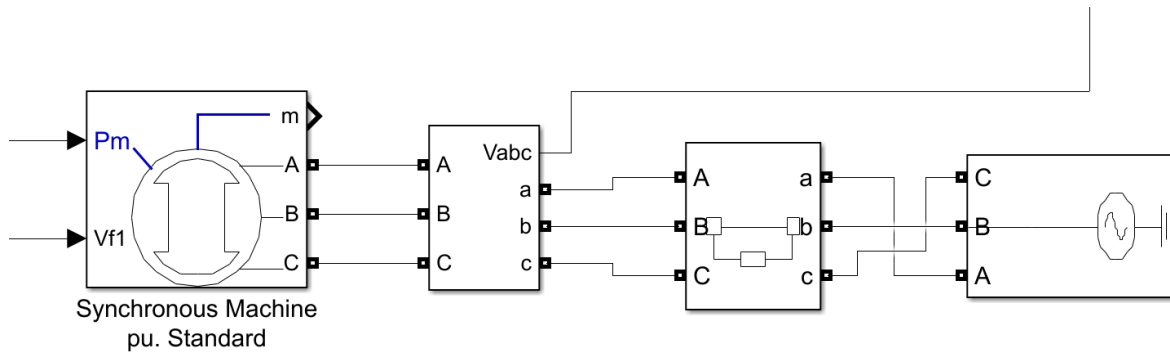


Figure 6.8: Model used for simulating of load rejection tests.

selected to give a similar deceleration as was found in the laboratory tests. This resulted in a friction factor of 0.1050. This is higher than what is seen in the laboratory. The no-load losses of the motor/generator set is approximately 4.5 kW giving a friction factor for $4.5/66.5 = 0.068$. This might indicate that the inertia estimated in [25] is too high. However, the generator's mechanical constants are not in the scope of this analysis and no further investigation on the inertia and friction constants were performed. Saturation has not been considered in the following simulations. Two simulation scenarios were performed. These are based on the d -axis and the arbitrary axis load rejection tests. In the simulations, the initial loading conditions were similar to the initial loading in the laboratory experiment. This was done to get comparable results.

$$H = \frac{0.5J\omega_{sm}^2}{S_n} = 3.01 \text{ s} \quad (6.10)$$

6.5.2 d -axis Load Rejection Simulation

Two simulations were performed with a similar initial load as the d -axis load rejection test described in Chapter 6.2. The initial conditions for the simulations are shown in Table 6.7. The initial conditions for the laboratory experiment are also included for easier comparison. One simulation was performed with identical field voltage as in the laboratory experiment. This gave higher reactive power consumption by the generator compared to what was found in the lab.

The main reason for this is suspected to be because the saturation effects are not simulated in the model. The field voltage base in the laboratory is given from the saturated voltage curve while the field voltage base in the simulation is selected with the air gap line. The field voltage base is selected automatically by MATLAB in the simulation model and can not be changed. As a result, the simulation model's field voltage are not directly comparable with the laboratory field voltage.

Table 6.7: Initial Conditions for the Simulated d -axis Test.

| Scenario | P | Q | V_t | V_f |
|----------|----------------|------------|-------|----------|
| Lab | ≈ 0 pu | - 0.857 pu | 1 pu | 0.356 pu |
| Sim 1 | 0 pu | - 0.914 pu | 1 pu | 0.356 pu |
| Sim 2 | 0 pu | - 0.876 pu | 1 pu | 0.383 pu |

The results of the simulations are plotted in Figure 6.9. It is seen that initial voltages differ between the simulation and the laboratory result. This is mainly due to the inaccuracy in the voltage measurement, as shown in Chapter 4.5.1. The voltage envelope from the first simulation with identical field voltage to the laboratory test (in pu) falls faster than the laboratory result. This is expected due to the inconsistent field voltages bases, which makes the initial reactive power consumption higher in the simulation. Meaning that the simulated model is more underexcited than the test performed in the laboratory. The second simulation where the reactive power output was matched is slightly higher than the laboratory result initially and converges with laboratory result after a few seconds. Ideally, the simulated result should be 2-3 % higher than the laboratory result due to the inaccuracy in the voltage measurement. It should also be noted that the second simulation should have had slightly higher field voltage to match the reactive power perfectly.

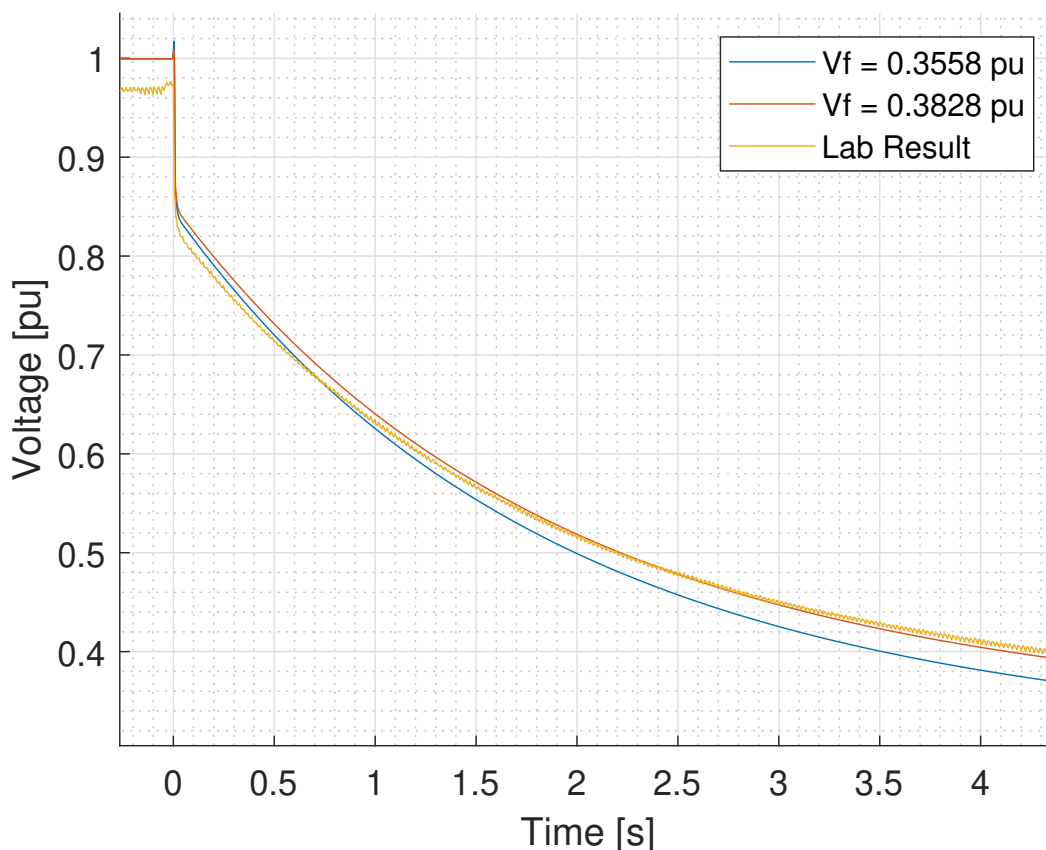


Figure 6.9: Simulated armature voltage envelope from the simulated d -axis load rejection test plotted together with the laboratory results.

The voltage level has been recorded at the times of the estimated open-circuit d -axis time constants. This is presented in Table 6.8. It is found that the simulated voltages are within a few per cent of the voltage recorded in the laboratory. This is within the known sources of errors such as voltage measurement inaccuracy and inconsistent field voltage bases. Some inaccuracy should also be expected of measurement of the initial active and reactive power from the laboratory.

Table 6.8: Voltage Comparison for the d -axis Simulation.

| | 0.11 s | 1.80 s |
|-------|----------|----------|
| Lab | 0.800 pu | 0.533 pu |
| Sim 1 | 0.814 pu | 0.520 pu |
| Sim 2 | 0.822 pu | 0.539 pu |

6.5.3 Arbitrary Axis Load Rejection Simulation

Similarly to the d -axis load rejection simulation, two simulations were performed based on the initial conditions from the arbitrary axis load rejection test described in Chapter 6.3.2. The initial load conditions for the simulations are presented in Table 6.9. The first simulation was performed with identical field voltages (in pu) and the other with reduced field voltage to compensate for saturation effects.

Table 6.9: Initial Conditions for the Simulated Arbitrary Axis Test.

| Scenario | P | Q | V_t | V_f | δ |
|----------|----------|----------|-------|----------|-------------|
| Lab | 0.459 pu | 0.280 pu | 1 pu | 1.262 pu | 8.6° |
| Sim 1 | 0.455 pu | 0.311 pu | 1 pu | 1.262 pu | 7.8° |
| Sim 2 | 0.458 pu | 0.220 pu | 1 pu | 1.200 pu | 8.2° |

Figure 6.10 shows the d -axis armature voltage envelope for the two simulations, and the laboratory results plotted together. The transient on the simulated voltages right after the load rejection is because the simulation model struggles to converge in the transition between the initial load conditions to the open circuit. However, even when ignoring the transient, the simulated voltages and the actual voltage are differing in the first 0.05 seconds. The reason for this is not known, but the noise on the measured power angle and the manual synchronising of the power angle and the voltages might be part of the explanation. The simulated voltages fit well with the trend line drawn in Figure 6.7.

It is observed that the simulated voltages continue out of the plot, while the measured voltage stabilises at around 0.03 pu. This is because the measured power angle has some noise and is not calibrated perfectly such that it does not go to an absolute zero value. On the other hand, the simulated power angle will become perfectly zero. This gives a relatively large difference on a semilogarithmic graph. The d -axis voltage levels were read at the time of the q -axis open-circuit subtransient time constant and are presented in the left column in Table 6.10. It is seen that these values are practically the same, especially for the first simulation with identical field voltage as for the laboratory experiment.

The simulated and measured armature voltage is presented in 6.11. Also here the large transient is observed right after opening the breaker, this transient can be ignored. It is seen that the simulated armature voltage is quite higher than the voltage envelope found based on the laboratory result. This is as expected as the generator is operating in the saturated region during this experiment. The armature voltage read at 3 s is presented in Table 6.10.

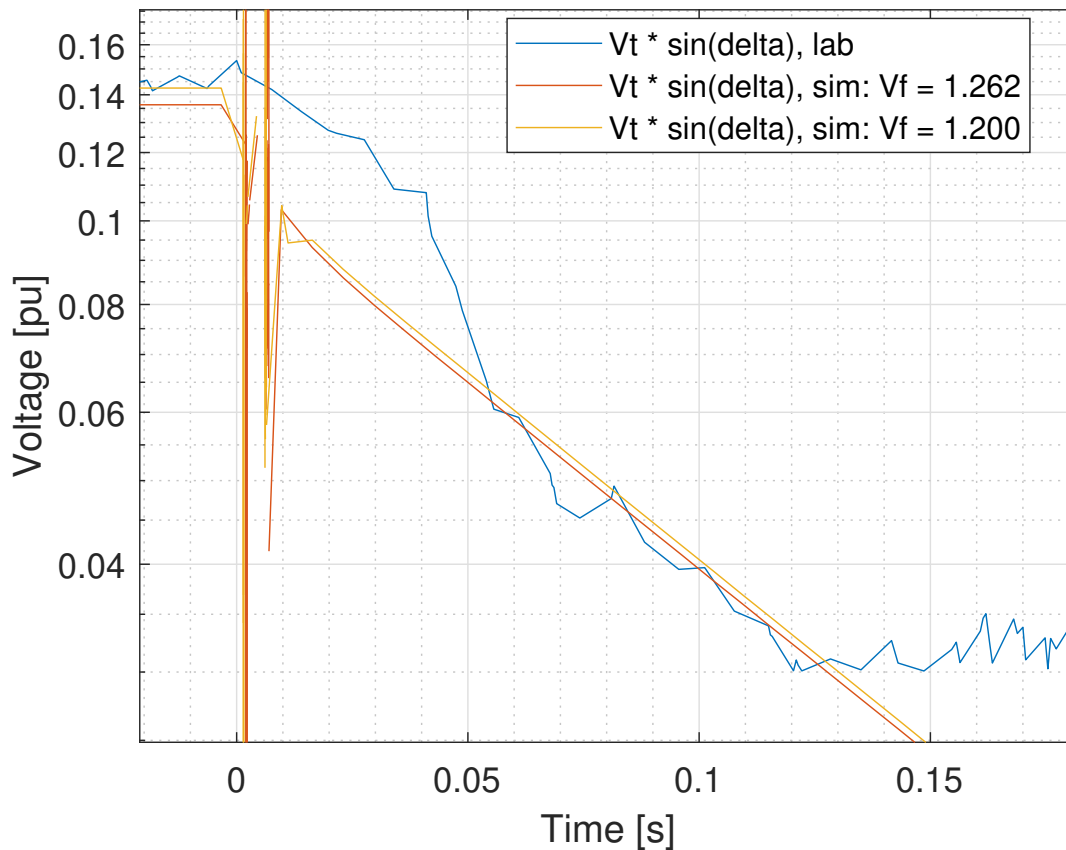


Figure 6.10: *d*-axis armature voltage envelope for the simulated arbitrary load rejection test, plotted together with the laboratory result.

If for simplicity the field current is assumed to be directly proportional to the field voltage the field current is in the first simulation equal to 1.262 pu. This corresponds to a field current of 7.75 A (this assumption truly only holds for steady-state operation). The difference between the air gap line and the saturated voltage can be found for this field current using the OOC and the air gap line as presented in Appendix B.3, Figure B.6. The difference between the air gap line and the saturated voltage at this field current were found to be 11.4 %.

The difference between the simulated voltage and the laboratory is less than expected from the OCC curve, with a percentage difference of 5.45 %. However, there are several sources of errors in these examples. The initial conditions do not match completely, and the measured voltage has an inaccuracy of 2 - 3 %. It should also be noted that the OCC curve used here can be

Table 6.10: Voltage Comparison for the Arbitrary Axis Simulation.

| | $V_t \sin(\delta)$ 0.1 s | V_t 3 s |
|-------|-----------------------------|--------------|
| Lab | 0.0396 pu | 1.10 pu |
| Sim 1 | 0.0395 pu | 1.16 pu |
| Sim 2 | 0.0405 pu | 1.11 pu |

regarded as the d -axis saturation curve, while the q -axis saturation curve is unknown. However, it is suspected that the saturation in the q -axis is lower than the d -axis as the q -axis flux path has less iron than the d -axis.

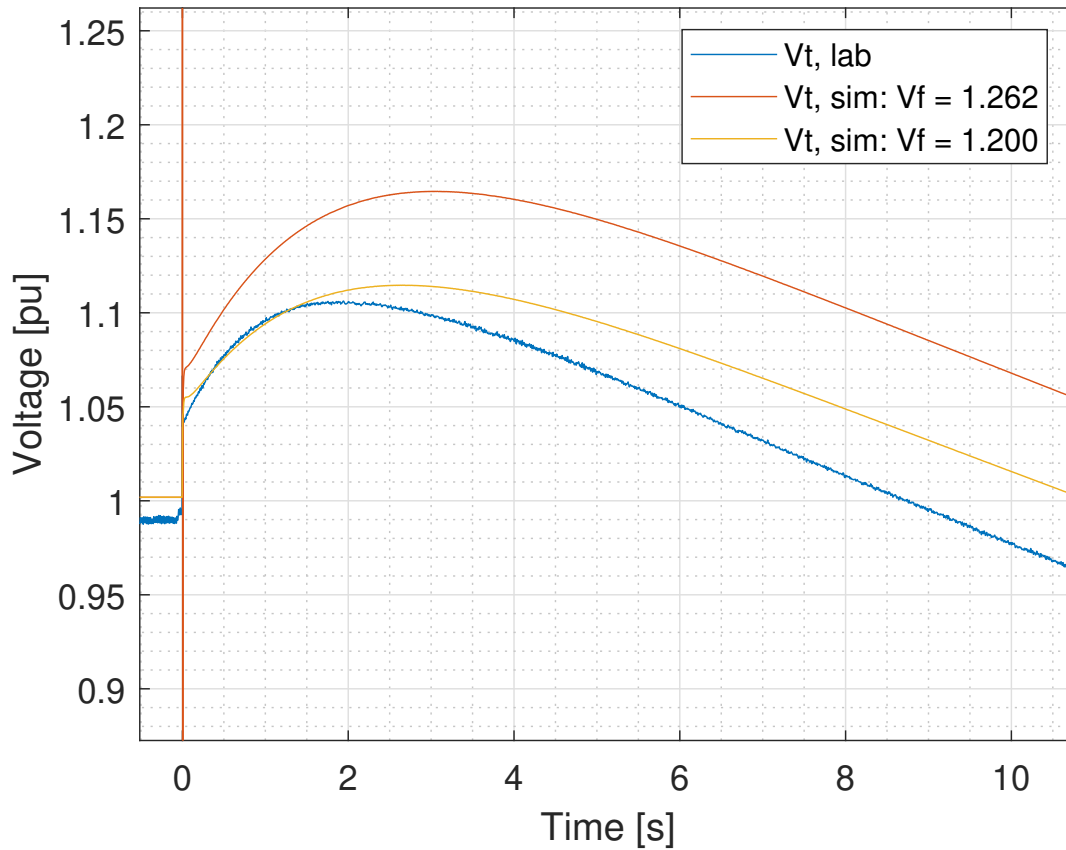


Figure 6.11: Simulated armature voltage envelope, plotted together with the laboratory result.

Conclusion and Further Work

7.1 Conclusion

This thesis has studied the virtual inertia support from a converter-fed power plant. A laboratory model with a simplified converter-interfaced power plant connected to a weak grid represented by a synchronous generator has been established. After proper tuning of the AVR the laboratory set-up worked as intended. A series of cases were performed to test the inertia emulation capabilities of the converter.

For the case with PQ + droop, the reduction in frequency nadir was found to 42.3 % compared the base case with no virtual inertia support. When df/dt IE was added, this was increased to 50 % reduction in frequency nadir. The converter is supporting the frequency by quickly injecting extra active power. For the case with both df/dt and droop enabled the power injection had a peak value 13.3 kW 1.3 seconds after the disturbance, from a baseload of 5.6 kW.

It is possible to further increase the inertia support by increasing the gains at the cost of higher harmonics from the converter. Gains for the droop and inertia constant over 5 showed a diminishing effect, and the THD increased more than the inertia support was improved. Stability margins were identified. With both the droop and inertia gains increased to 10, the converter became unstable, and the current output was oscillating between the upper and lower limits of the converter. It is found that when keeping either the droop or the inertia gain at the initial value of 5, the other constant can be raised to 11 before the system approaches instability. This gives increased frequency support but at the cost of increased harmonics on the output current. Thus, the tuning of the converter's inertia loop is a trade-off between the THD of the current and the frequency support.

Several experiments were performed testing whether the initial load conditions affected the converter's frequency support. It was found that initial load conditions had little effect on the frequency support. A slight difference was found correlating the to the reactive power output of the converter. It is suspected that the difference in reactive power flow changes the voltage over the local load. This will, in turn, change the active power for a given step in resistance.

Three load shedding tests were performed to estimate the standard electrical parameters of the synchronous machine. The d-axis load shedding test showed promising results and estimated

values for the d-axis parameters x_d , x'_d , x''_d , T'_{do} and T''_{do} were found. The short circuit time constants T'_d and T''_d was calculated with the known relationship between the open and short circuit time constants. It is suspected that the parameters are estimated within a few percentages of the real values.

The q-axis load shedding test gave inconclusive results due to the initial field voltage being almost 1 pu, resulting in barely any dynamics in the armature voltage after the load shedding. The arbitrary load axis test gave better result and values for the q-axis parameters x_q , x''_q and T''_{qo} were estimated. Similarly, as for the d-axis, the short circuit time constant was calculated based on the known relationship between the open and short circuit time constants. It is suspected that the estimated q-axis parameters are more uncertain than the d-axis parameters because the estimation depended on a noisy measurement of the load angle. The estimated parameters is summarised in Table 7.1. The only standard electrical parameter not estimated in this thesis is the leakage reactance x_l . A good guess for this parameter is 10 - 15 % of x_d , and it must be smaller than the smallest subtransient reactance.

Table 7.1: Summary of the Estimated Electrical Parameters for the Siemens-Schuckert Synchronous Machine. The Impedance Base is 2.406 Ω .

| Parameter | Estimated Value |
|------------|-----------------|
| R_a | 0.0236 pu |
| x_d | 0.7029 pu |
| x'_d | 0.1657 pu |
| x''_d | 0.1051 pu |
| x_q | 0.3542 pu |
| x''_q | 0.1012 pu |
| T'_d | 0.42 s |
| T'_{do} | 1.80 s |
| T''_d | 0.007 s |
| T''_{do} | 0.011 s |
| T''_q | 0.029 s |
| T''_{qo} | 0.10 s |

A simulation model of the load shedding tests was established as a sanity check for the estimated values. The simulated d-axis test showed a resulting voltage curve off by a few percentages compared to the laboratory result. The simulation for the arbitrary test was not as precise as the d-axis test. This was as expected as the arbitrary test was performed with a saturated generator, and the simulation model was not accounting for the machine's saturation. The simulated armature voltage was differing by 5.45 % from the voltage recorded in the lab.

7.2 Further Work

In the following, some suggestions for further work are presented.

- The VSHP power plant was in the experiments performed in this thesis approximated with a single VSC supplied by a DC-voltage source. The laboratory set-up could be expanded with another motor/generator set to represent the power plant and a back-to-back VSC. This set-up could also include a real-time simulation model of a hydropower plant to include dynamics related to the hydraulics and the turbine.
- In this thesis, grid forming capabilities were not required, meaning that the converter is not able to perform a black start or sustain islanding. More complex methods for creating virtual inertia can be examined, for example, virtual synchronous machine algorithms with grid forming capabilities. This can be done with the laboratory set-up established in this thesis, or with the expanded set-up as suggested above.
- Previous master student Gallefoss [41] have established a simulation model for analysing virtual inertia from a VSHP. This model is not directly comparable with the laboratory experiment performed in this thesis. It could be interesting to build a simulation model based on the laboratory set-up presented in this thesis with the estimated parameters for the synchronous generator.

Bibliography

- [1] Mengran Yu, Adam Dyško, Campbell Booth, Andrew Roscoe, Jiebei Zhu, and Helge Urdal. Investigations of the Constraints relating to Penetration of Non-Synchronous Generation (NSG) in Future Power Systems. In *Protection, Automation and Control (PAC) World Conference*, page 29–44, 2015.
- [2] B Kroposki, B Johnson, Y Zhang, V Gevorgian, P Denholm, B Hodge, and B Hannegan. Achieving a 100% Renewable Grid: Operating Electric Power Systems with Extremely High Levels of Variable Renewable Energy. *IEEE Power and Energy Magazine*, 15(2):61–73, 2017.
- [3] Mostafa Valavi and Arne Nysveen. Variable-Speed Operation of Hydropower Plants: A Look at the Past, Present, and Future. *IEEE Industry Applications Magazine*, 24(5):18–27, 2018.
- [4] Ana Fernández-Guillamón, Emilio Gomez-Lazaro, Eduard Muljadi, and Ángel Molina-Garcia. A Review of Virtual Inertia Techniques for Renewable Energy-Based Generators. 5 2020.
- [5] Fingrid Oyj, Energinet, Affärsverket Svenska Kraftnät, and Statnett SF. Challenges and Opportunities for the Nordic Power System. Technical report, 2016.
- [6] Kjeld Fjeldberg. *Theoretical and Practical Foundation for Laboratory Experiments of Virtual Inertia in Hydro Power Application*. Specialisation Project, NTNU: Norwegian University of Science and Technology, 2020.
- [7] Jan Machowski, Janusz W. Bialek, and James R. Bumby. *Power System Dynamics : Stability and Control*. Wiley, Chichester, 2nd ed. edition, 2008.
- [8] Fingrid Oyj, Energinet, Affärsverket Svenska Kraftnät, Kraftnät Åland AB, and Statnett SF. Explanatory document for the Nordic synchronous area proposal for frequency quality defining parameters and the frequency quality target parameter in accordance with Article 127 of the Commission Regulation (EU) 2017/1485. Technical report, 2017.
- [9] Lei Shang, Jiabing Hu, Xiaoming Yuan, and Yongning Chi. Understanding Inertial Response of Variable-Speed Wind Turbines by Defined Internal Potential Vector. *Energies*, 10(1), 2017.

-
- [10] Prabha Kundur. *Power System Stability and Control*. The EPRI power system engineering series. McGraw-Hill, New York, 1994.
- [11] Mircea Eremia and Mohammad Shahidehpour. *Handbook of Electrical Power System Dynamics: Modeling, Stability, and Control*, volume 92 of *IEEE Press Series on Power Engineering*. New York: Wiley-IEEE Press, New York, 1. Aufl. edition, 2013.
- [12] Math H. J. Bollen. *Integration of distributed generation in the power system*, volume 81 of *IEEE Press series on power engineering*. Wiley, Hoboken, New Jersey, 2011.
- [13] Ziping Wu, Wenzhong Gao, Tianqi Gao, Weihang Yan, Huaguang Zhang, Shijie Yan, and Xiao Wang. State-of-the-Art Review on Frequency Response of wind Power Plants in Power Systems. *Journal of Modern Power Systems and Clean Energy*, 6(1):1–16, 2018.
- [14] P K Steimer, O Senturk, S Aubert, and S Linder. Converter-fed synchronous machine for pumped hydro storage plants. In *2014 IEEE Energy Conversion Congress and Exposition (ECCE)*, pages 4561–4567, 2014.
- [15] Thomas Hildinger and Ludger Ködding. *Modern Design for Variable Speed Motor-Generators - Asynchronous (DFIM) and Synchronous (SMFI) Electric Machinery - Options for Pumped Storage Power Plants*. 2013.
- [16] MWH Americas Inc. Technical Analysis of Pumped Storage and Integration with Wind Power in the Pacific Northwest. Technical report, Army Corps of Engineers Northwest Division - Hydroelectric Design Center, 2009.
- [17] Johan Morren, Jan Pierik, and Sjoerd W H de Haan. Inertial response of variable speed wind turbines. *Electric Power Systems Research*, 76(11):980–987, 2006.
- [18] Statnett SF. Fast Frequency Reserves. Technical report, 2018.
- [19] Hans-Peter Beck and Ralf Hesse. Virtual synchronous machine. In *2007 9th International Conference on Electrical Power Quality and Utilisation*, pages 1–6, 2007.
- [20] S D’Arco and J A Suul. Virtual synchronous machines — Classification of implementations and analysis of equivalence to droop controllers for microgrids. In *2013 IEEE Grenoble Conference*, pages 1–7, 2013.
- [21] H Alrajhi Alsiraji and R El-Shatshat. Comprehensive Assessment of Virtual Synchronous Machine Based Voltage Source Converter Controllers. *IET Generation, Transmission Distribution*, 11(7):1762–1769, 2017.
- [22] S D’Arco and J A Suul. Equivalence of Virtual Synchronous Machines and Frequency-Droops for Converter-Based MicroGrids. *IEEE Transactions on Smart Grid*, 5(1):394–395, 1 2014.
- [23] D. P. Kothari and I. J. Nagrath. *Electric Machines*. McGraw Hill Education (India), Chennai, 5th edition, 2018.
- [24] Trond Leiv Toftevaag. Personal Communication 13.01, 2021.

-
- [25] August Jaros. *Parameter Identification of Synchronous Generator Using Standstill Frequency Response (SSFR) Test*. MSc Thesis, Norwegian University of Science and Technology, 2019.
- [26] F P de Mello and J R Ribeiro. Derivation of synchronous machine parameters from tests. *IEEE Transactions on Power Apparatus and Systems*, 96(4):1211–1218, 1977.
- [27] J C Pequeña Suni, E Ruppert, and F Fajoni. A guide for synchronous generator parameters determination using dynamic simulations based on IEEE standards. In *The XIX International Conference on Electrical Machines - ICEM 2010*, pages 1–6, 2010.
- [28] Peter Vas. *Parameter estimation, condition monitoring, and diagnosis of electrical machines*, volume 27 of *Monographs in electrical and electronic engineering*. Clarendon Press, Oxford, 1993.
- [29] Kjell Ljøkelsøy. Project Memo: Control System for a Three-Phase Grid Connected Converter. Technical manual, SINTEF Energy, 2019.
- [30] Kjell Ljøkelsøy. Project Memo: Control system for DC motordrive. Technical manual, SINTEF Energy, 2019.
- [31] Kjell Ljøkelsøy. Project Memo: PicoZed Based Processor Board V1.1. Technical manual, SINTEF Energy, 2020.
- [32] Kjell Ljøkelsøy. Project Memo: Excitation Converter Control System. Technical manual, SINTEF Energy, 2020.
- [33] Kjell Ljøkelsøy. Project Memo: 60 kVA Laboratory converter unit. Technical manual, SINTEF Energy, 2019.
- [34] J Are Suul and S D’Arco. Comparative Analysis of Small-Signal Dynamics in Virtual Synchronous Machines and Frequency-Derivative-Based Inertia Emulation. In *2018 IEEE 18th International Power Electronics and Motion Control Conference (PEMC)*, pages 344–351, 8 2018.
- [35] Suresh Mikkili, Anup Kumar Panda, and Jayanthi Prattipati. Review of Real-Time Simulator and the Steps Involved for Implementation of a Model from MATLAB/SIMULINK to Real-Time. *Journal of The Institution of Engineers (India): Series B*, 96(2):179–196, 2015.
- [36] Kiyong Kim and R C Schaefer. Tuning a PID controller for a digital excitation control system. *IEEE Transactions on Industry Applications*, 41(2):485–492, 2005.
- [37] K Kim, P Rao, and J A Burnworth. Self-Tuning of the PID Controller for a Digital Excitation Control System. *IEEE Transactions on Industry Applications*, 46(4):1518–1524, 2010.
- [38] Dr. P.S Bimbhra. *Electrical Machinery*. Khanna Publishers, Delhi, 7th edition, 2014.
- [39] A E Fitzgerald. *Electric machinery*. McGraw-Hill series in electrical and computer engineering. McGraw-Hill, Boston, 6th ed. edition, 2003.
-

-
- [40] A M El-Serafi and N C Kar. Methods for determining the q-axis saturation characteristics of salient-pole synchronous machines from the measured d-axis characteristics. *IEEE Transactions on Energy Conversion*, 18(1):80–86, 2003.
- [41] Mathias Gallefoss. *Synthetic Inertia from a Converter-Fed Synchronous Machine in a Hydro-Electric Power Plant*. MSc Thesis, Norwegian University of Science and Technology, Trondheim, 2018.
- [42] Bård Almås. Circuit Diagram For Siemens-Schutkert motor/generator, 2020.
- [43] Bård Almås. Smart Grid Lab. https://arkiv.elkraft.ntnu.no/lableie_ekstern/SmartGridLabDrawing.htm (accesed Dec. 01, 2020).

Results - Virtual Inertia

A.1 Close-Up of Initial ROCOF After Step in Load

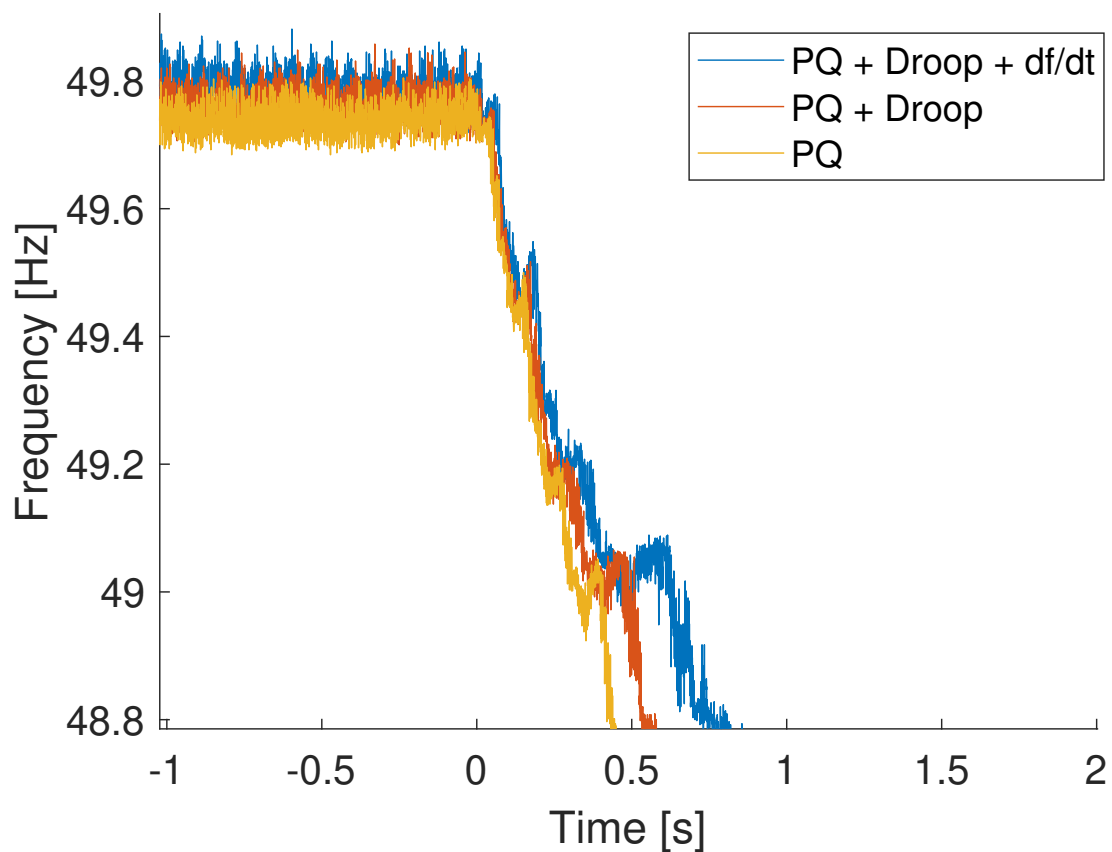


Figure A.1: Close-up of Figure 5.1 showing the initial ROCOF after a step in electrical load from 11.6Ω to 5.7Ω .

A.2 Close-Up of the Active Power Flow From the Generator During Step in Load

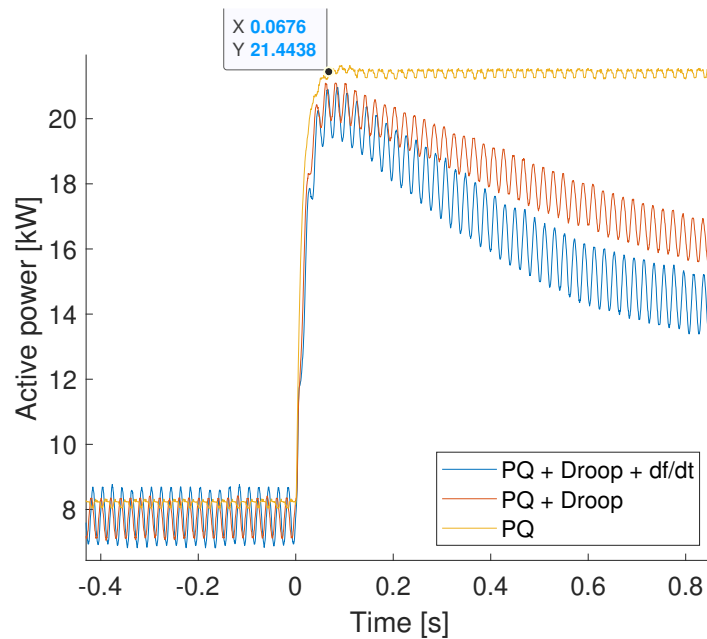


Figure A.2: Close-up of Figure 5.2 showing the active power flow from the generator after a step in electrical load from 11.6Ω to 5.7Ω .

A.3 Close-Up of the Active Power Flow From the Converter During Step in Load

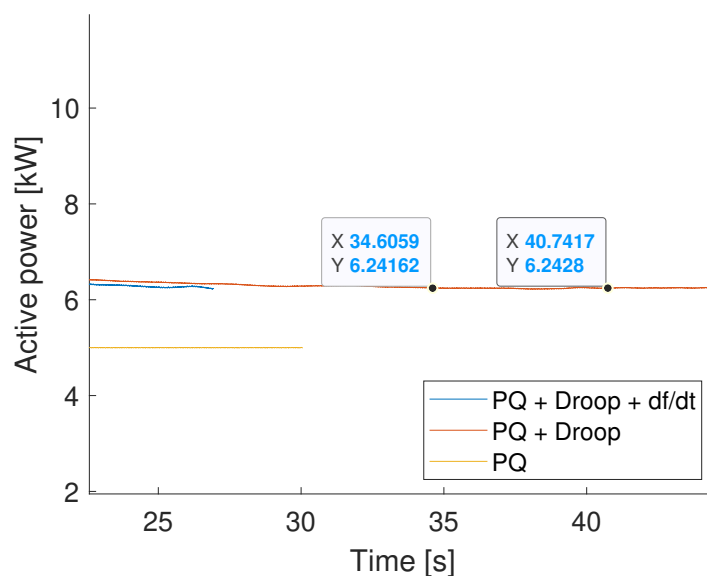


Figure A.3: Close-up of Figure 5.3 showing the active power flow from the converter after a step in electrical load from 11.6Ω to 5.7Ω .

A.4 Frequency Plots for the Remaining Cases of the Stability Limit Study

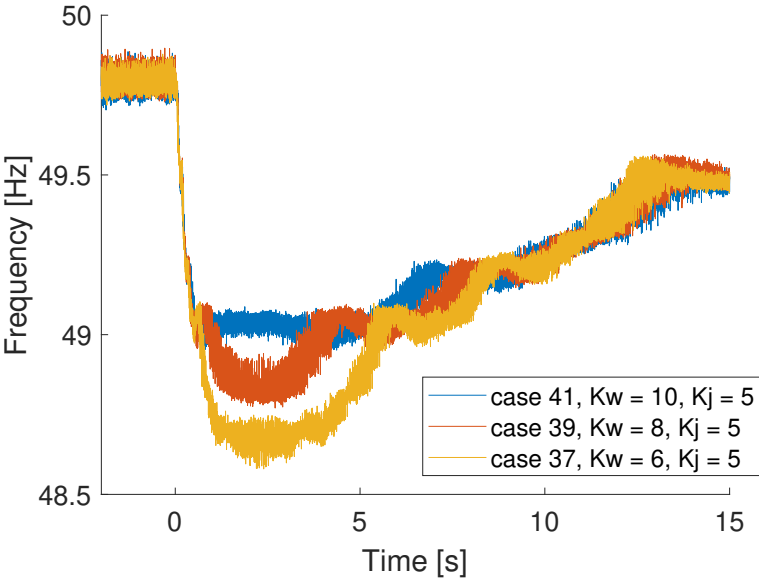


Figure A.4: Frequency during step in load with different droop gains, rest of the cases.

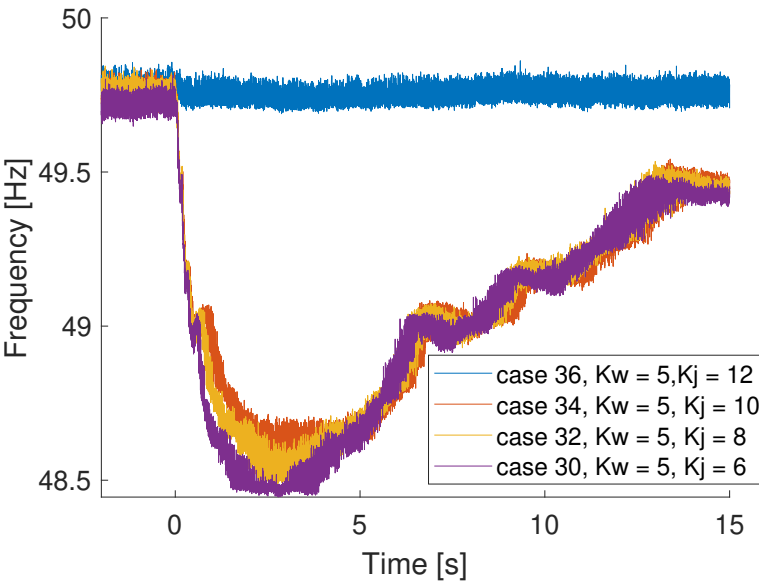


Figure A.5: Frequency during step in load with different droop gains, rest of the cases.

A.5 Fast Fourier Transform Analysis of Case 35

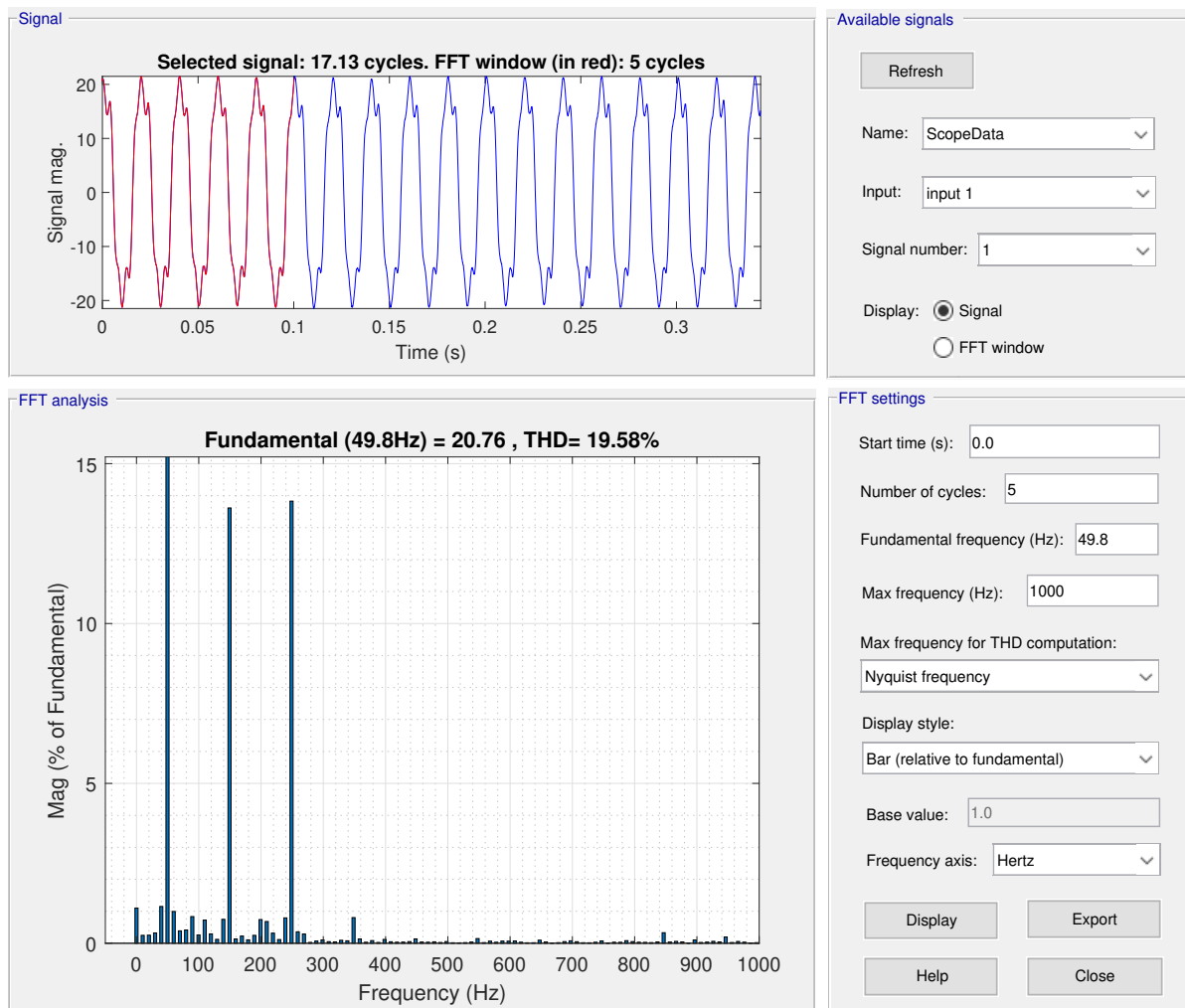


Figure A.6: FFT analysis of current from the converter in case 35.

A.6 Current for Unstable Case

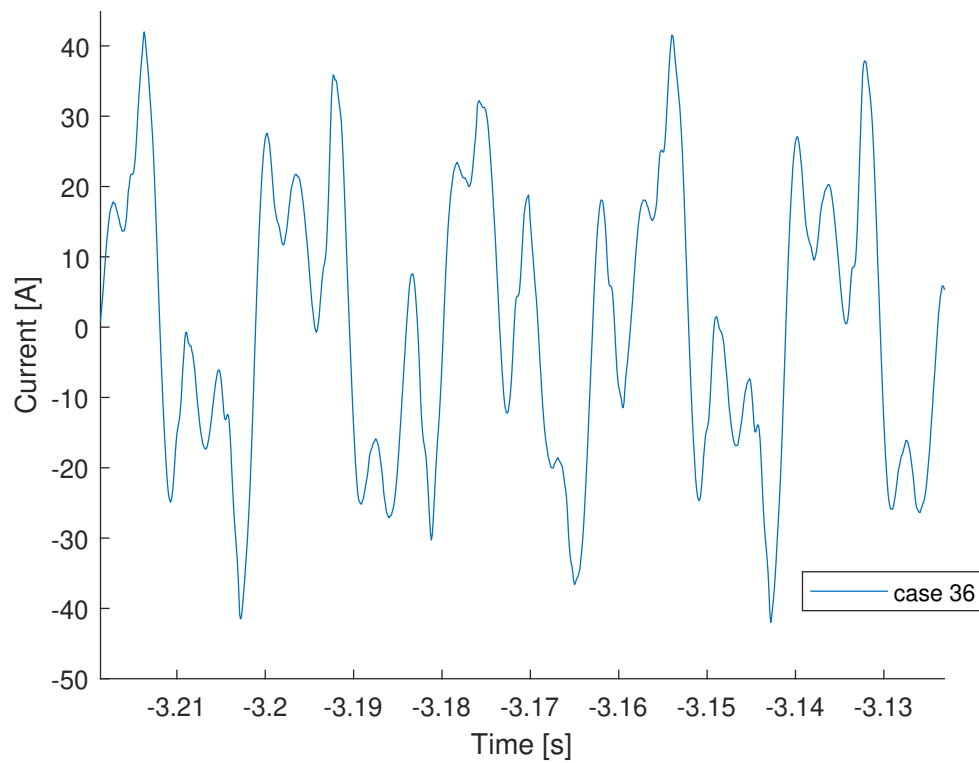


Figure A.7: Current for unstable case 36, $K_w = 5$, $K_j = 12$.

A.7 Active Power Plots for the Inital Load Conditions Study

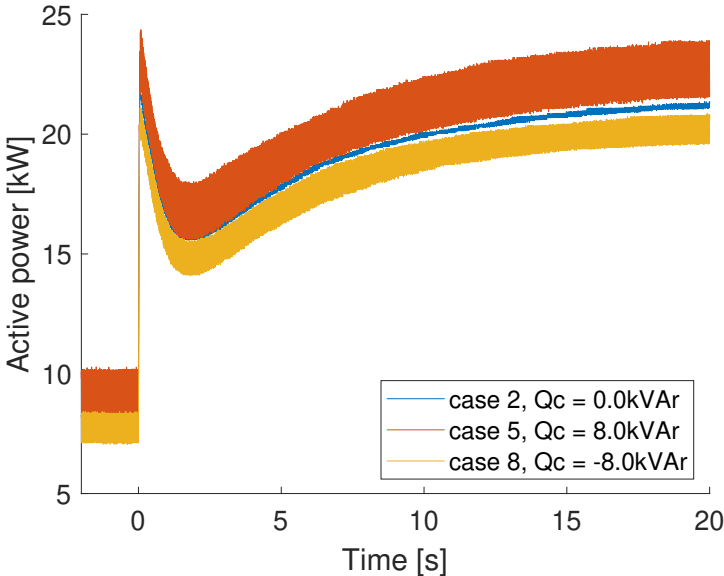


Figure A.8: Active power from generator during step in load with positive, negative and zero reactive power flow out from the converter. The active power load is shared between the generator and converter.

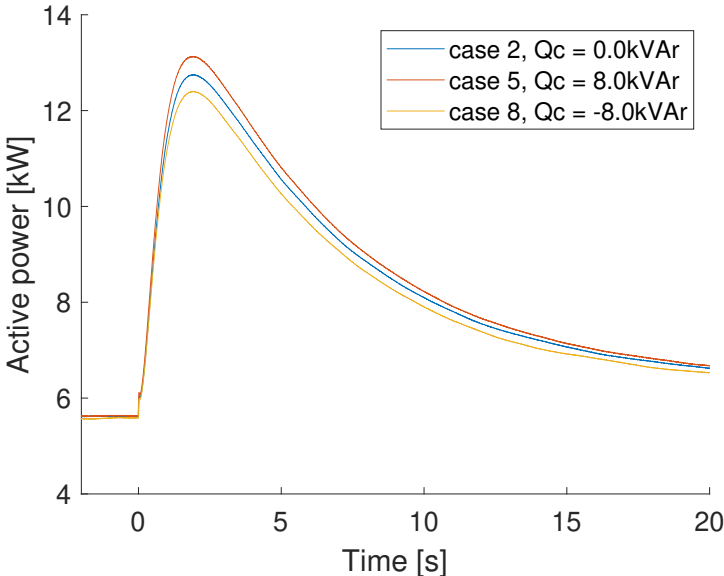


Figure A.9: Active power from converter during step in load with positive, negative and zero reactive power flow out from the converter. The active power load is shared between the generator and converter.

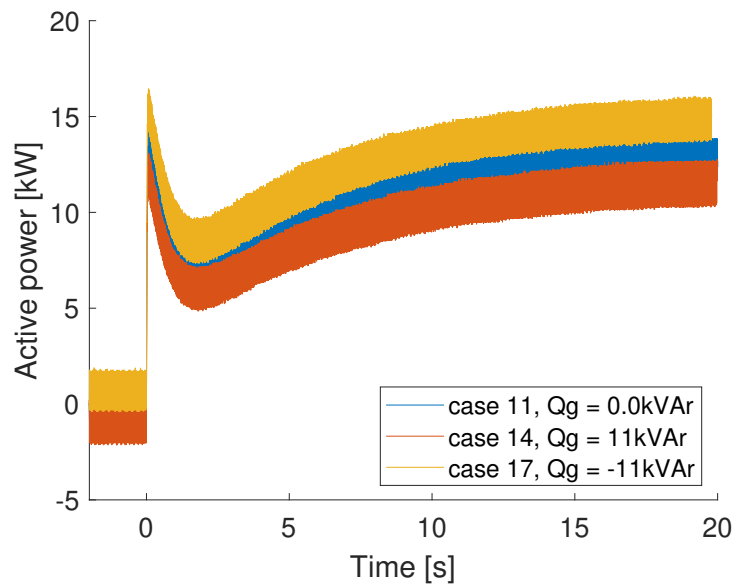


Figure A.10: Active power from generator during step in load with positive, negative and zero reactive power flow out from the generator. The generator is running no-load.

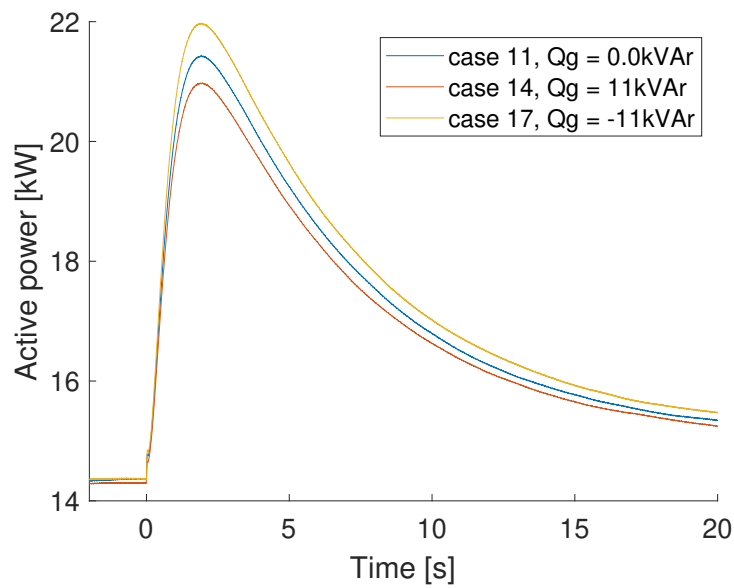


Figure A.11: Active power from converter during step in load with positive, negative and zero reactive power flow out from the generator. The generator is running no-load.

Results - Parameter Estimation

B.1 *d*-axis Parameter Estimation

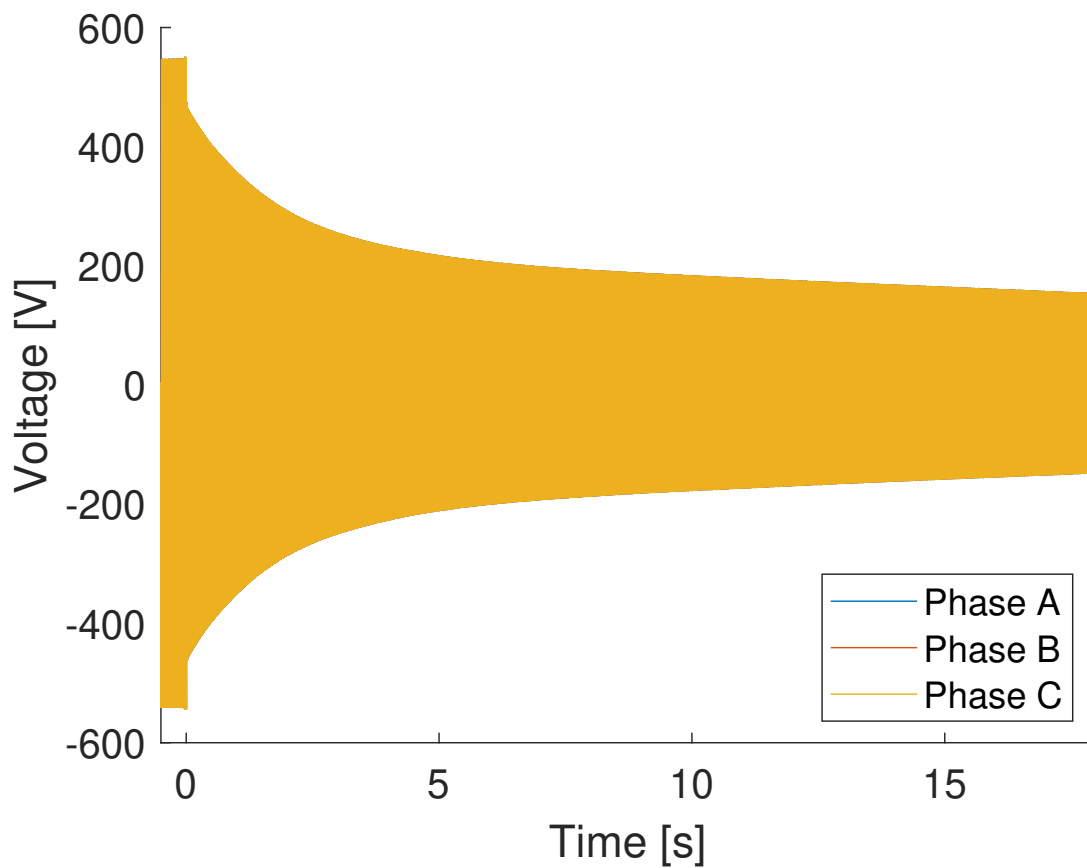


Figure B.1: Instantaneous values of the terminal voltages during *d*-axis load rejection.

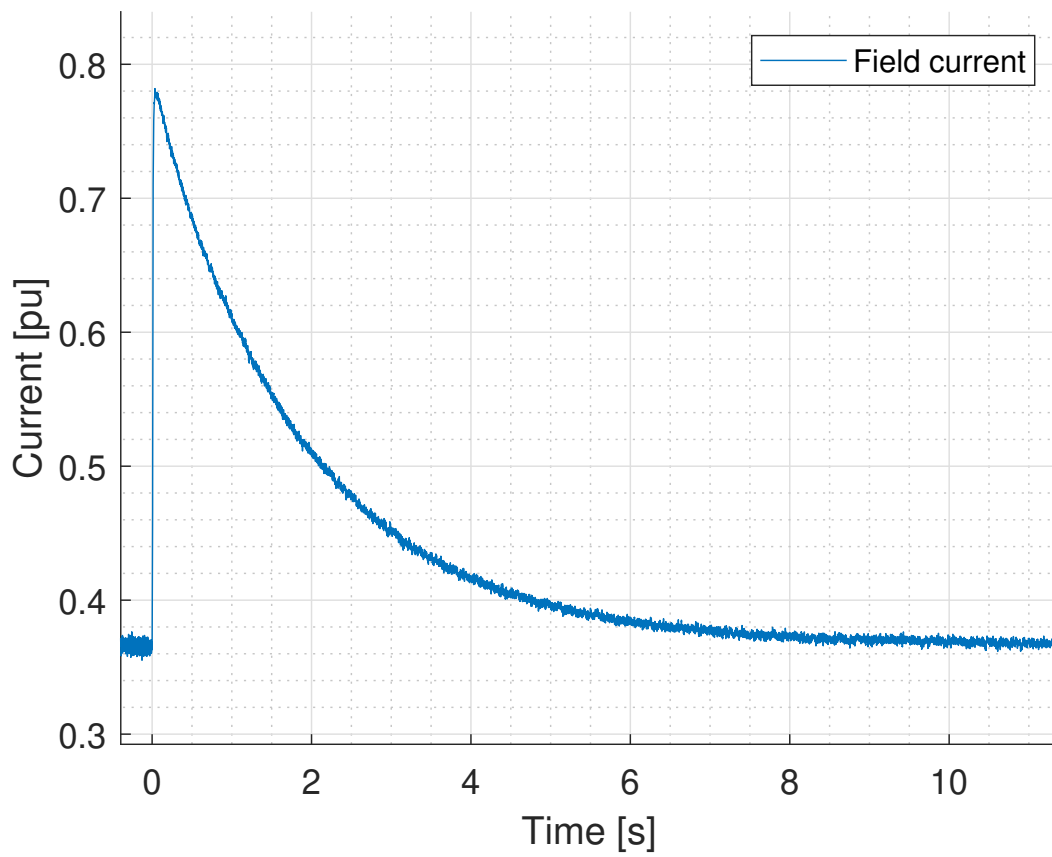


Figure B.2: Field current during d -axis load rejection.

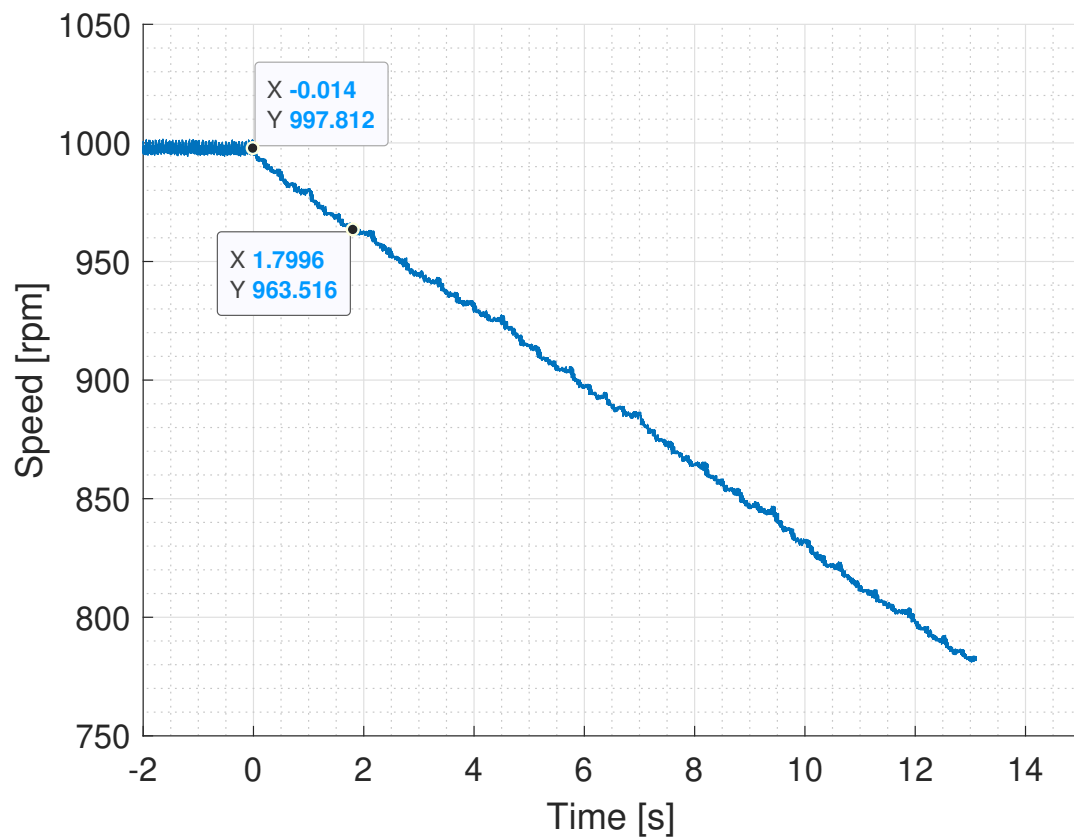


Figure B.3: Speed of motor/generator set during d -axis load rejection.

B.2 q -axis Parameter Estimation

B.2.1 q -axis Load Rejection Test

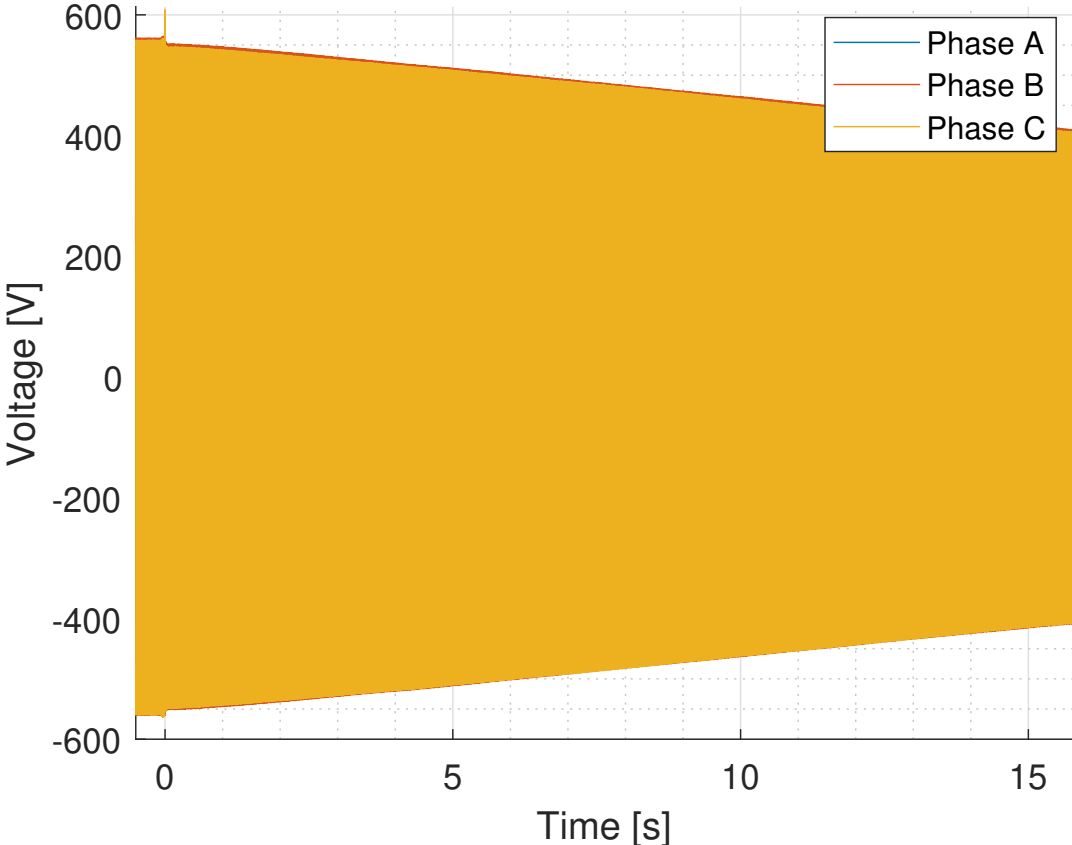


Figure B.4: Instantaneous values of the terminal voltages during the q -axis load rejection test.

B.2.2 Arbitrary Axis Load Rejection Test

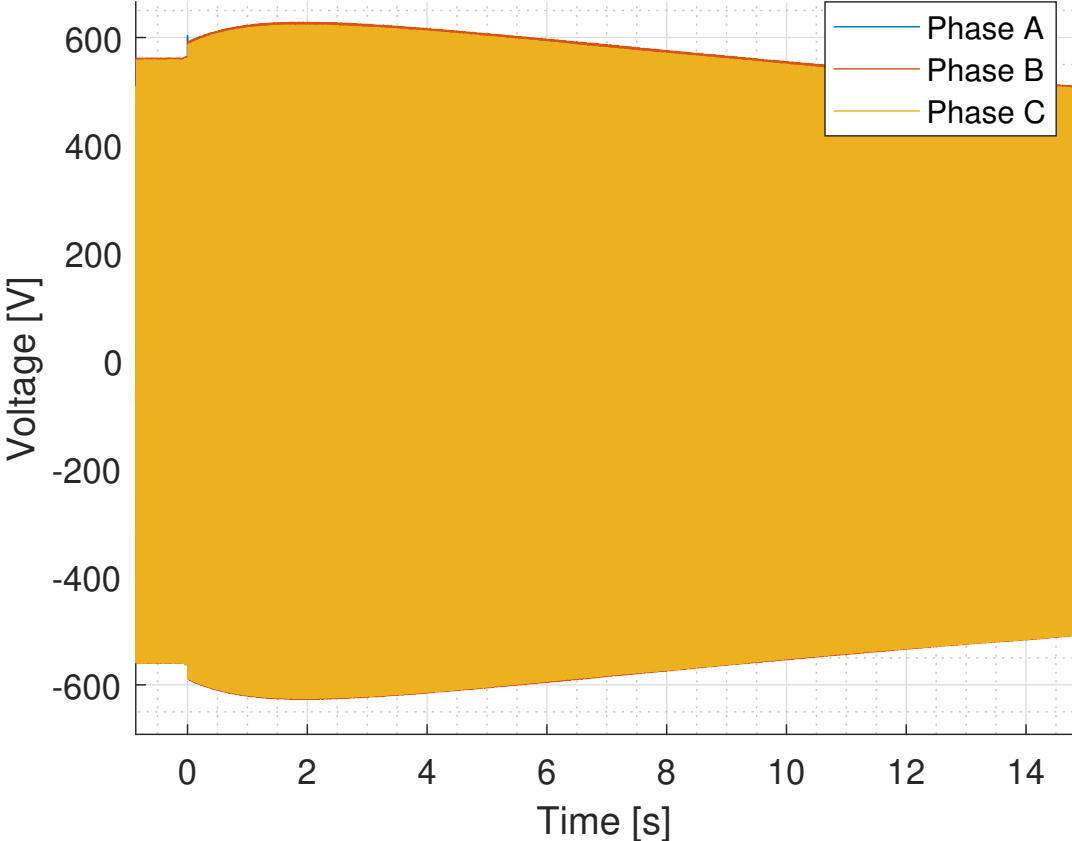


Figure B.5: Instantaneous values of the terminal voltages during the arbitrary axis load rejection test.

B.3 OCC and SCC for the Siemens-Schuckert Synchronous Machine

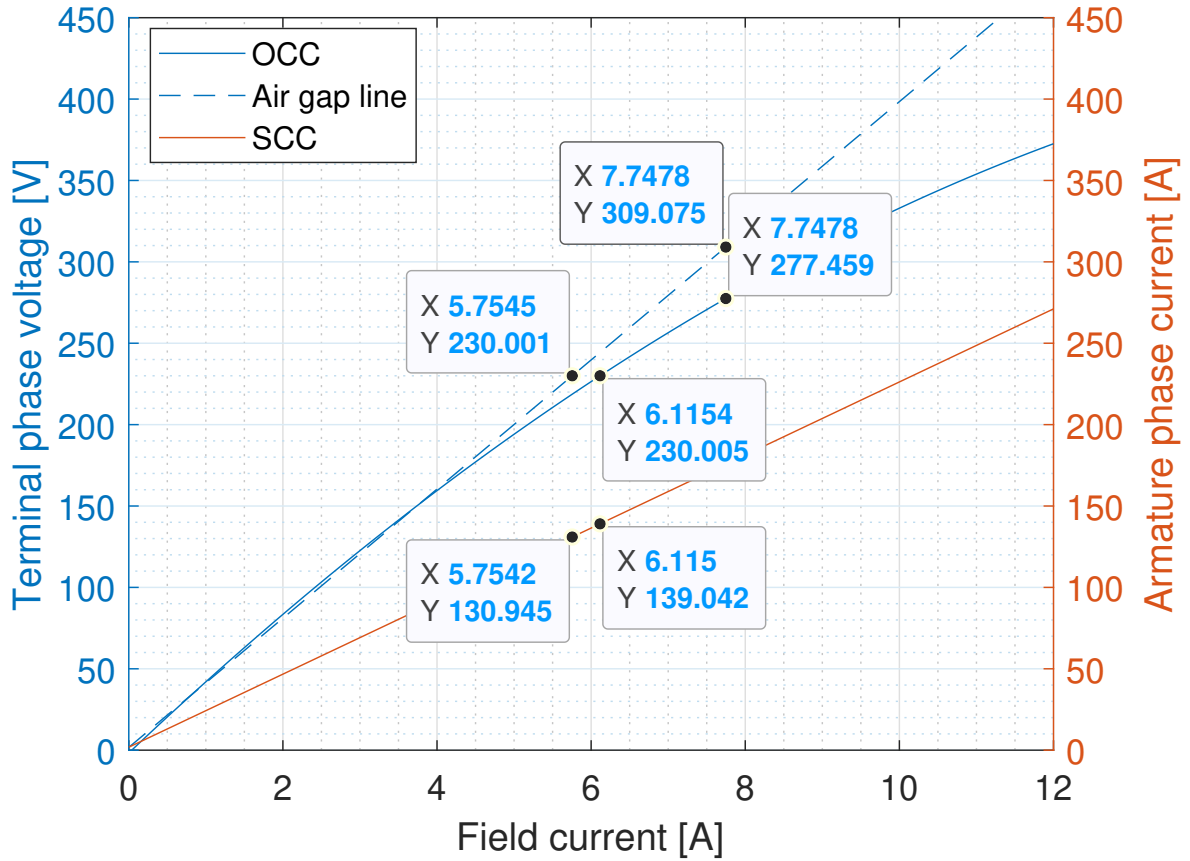


Figure B.6: The open circuit characteristics and the short circuit characteristics for the Siemens-Schuckert synchronous machine as measured by [25].

The curves as given in [25] are presented here in Equations B.1 - B.3. The OCC is based on measurements of armature voltages in range of 0 - 311 V and the SCC is based on current measurements in range from 0 - 80 A. The measurement data can be found in in [25].

$$V_{OCC} = -1.139i_f^2 + 44.86i_f - 1.735 \quad (\text{B.1})$$

$$V_{airgap} = 39.67i_f - 1.72 \quad (\text{B.2})$$

$$I_{SCC} = 22.44i_f + 1.821 \quad (\text{B.3})$$

Preliminary Laboratory Work

C.1 Voltage Measurements Circuit Diagram

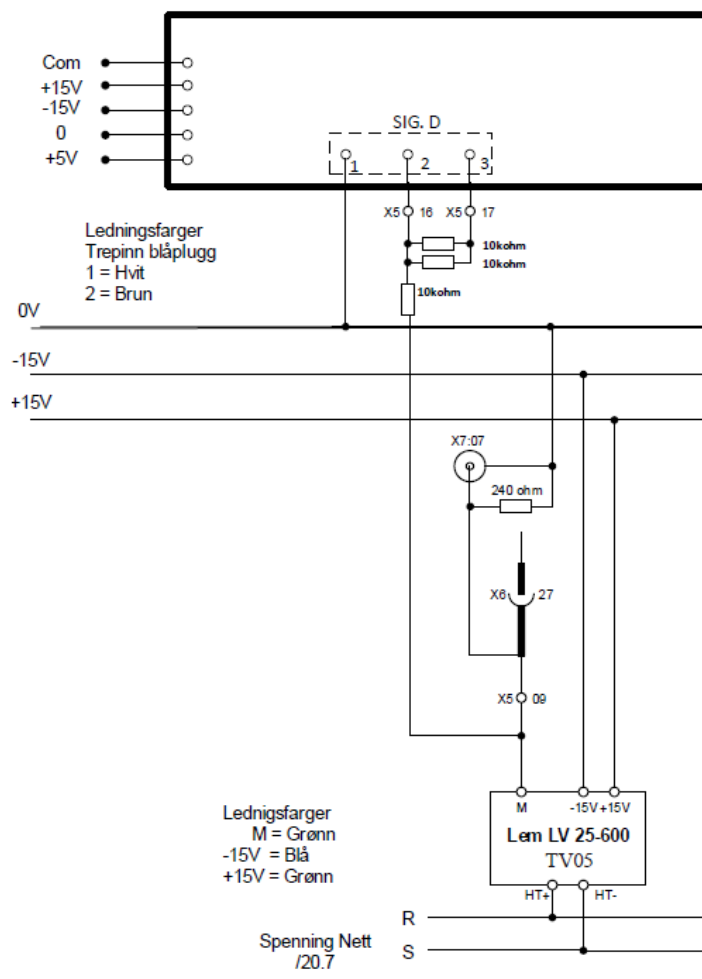


Figure C.1: Circuit for voltage measurement for phase L1-L2 on the synchronous generator, identical circuits exist for L2-L3 and L3-L1 [42].

C.2 Voltage Measurements

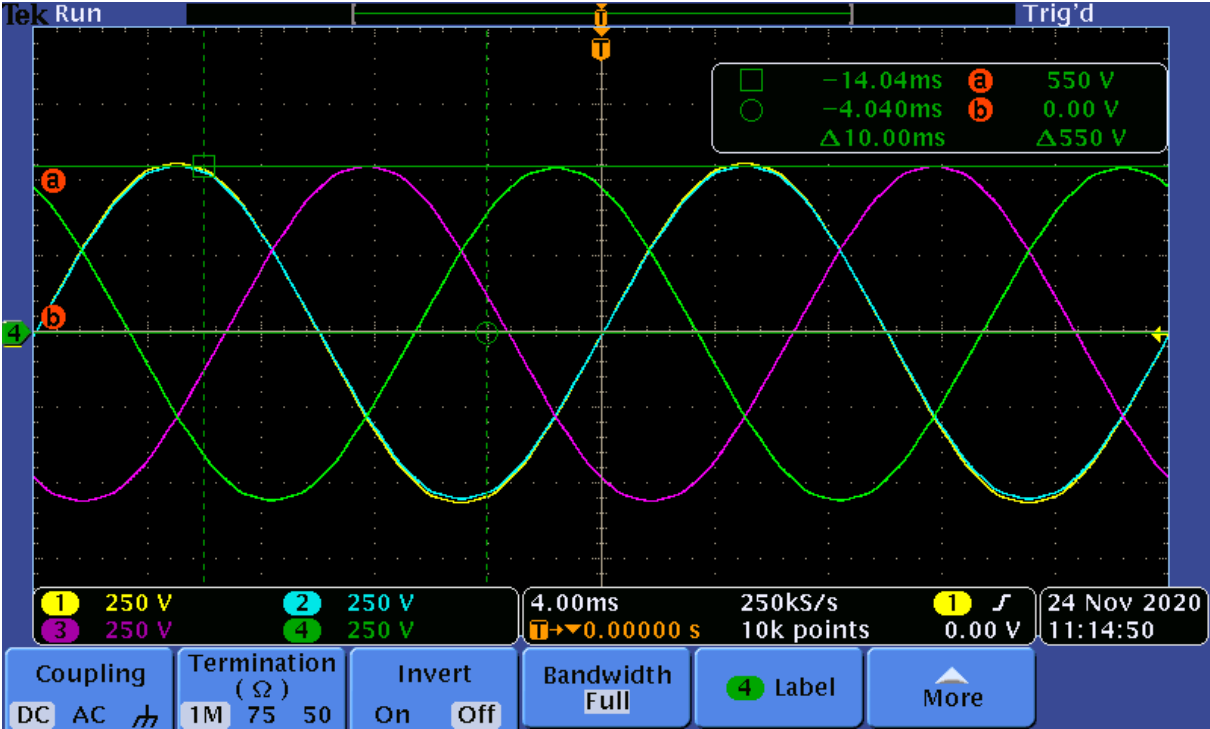


Figure C.2: The three phase voltage as measured with the oscilloscope, generator running open circuit with rms voltage of 400.4 V as measured with the multimeter.

C.3 AVR Tuning

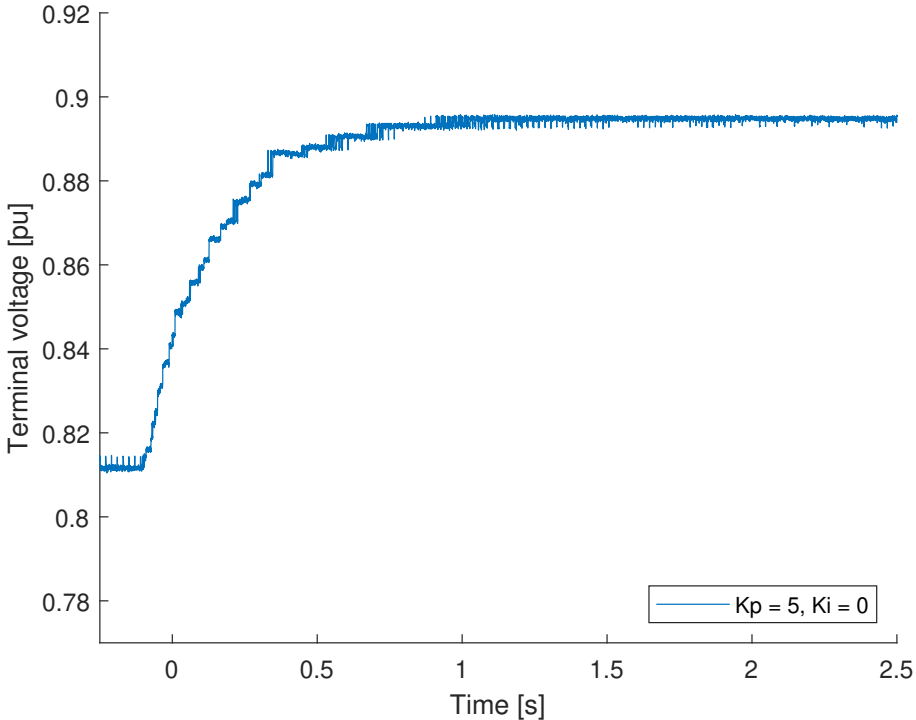


Figure C.3: Step response for the terminal voltage of the synchronous generator for a step in voltage reference from 0.95 pu to 1.1 pu.

Laboratory Set-Up

D.1 Control Cabinet for the Siemens-Schuckert Motor/Generator Set



Figure D.1: Picture of the control cabinet for the Siemens-Schuckert motor/generator set.

D.2 Picture of the VSC



Figure D.2: Picture of the voltage source converter.

D.3 Picture of the EGSTON Power Amplifier



Figure D.3: Picture of the EGSTON 200 kVA power amplifier.

D.4 Screenshot of the Auto Tune Window in Basler BEST-COMSPPlus Software

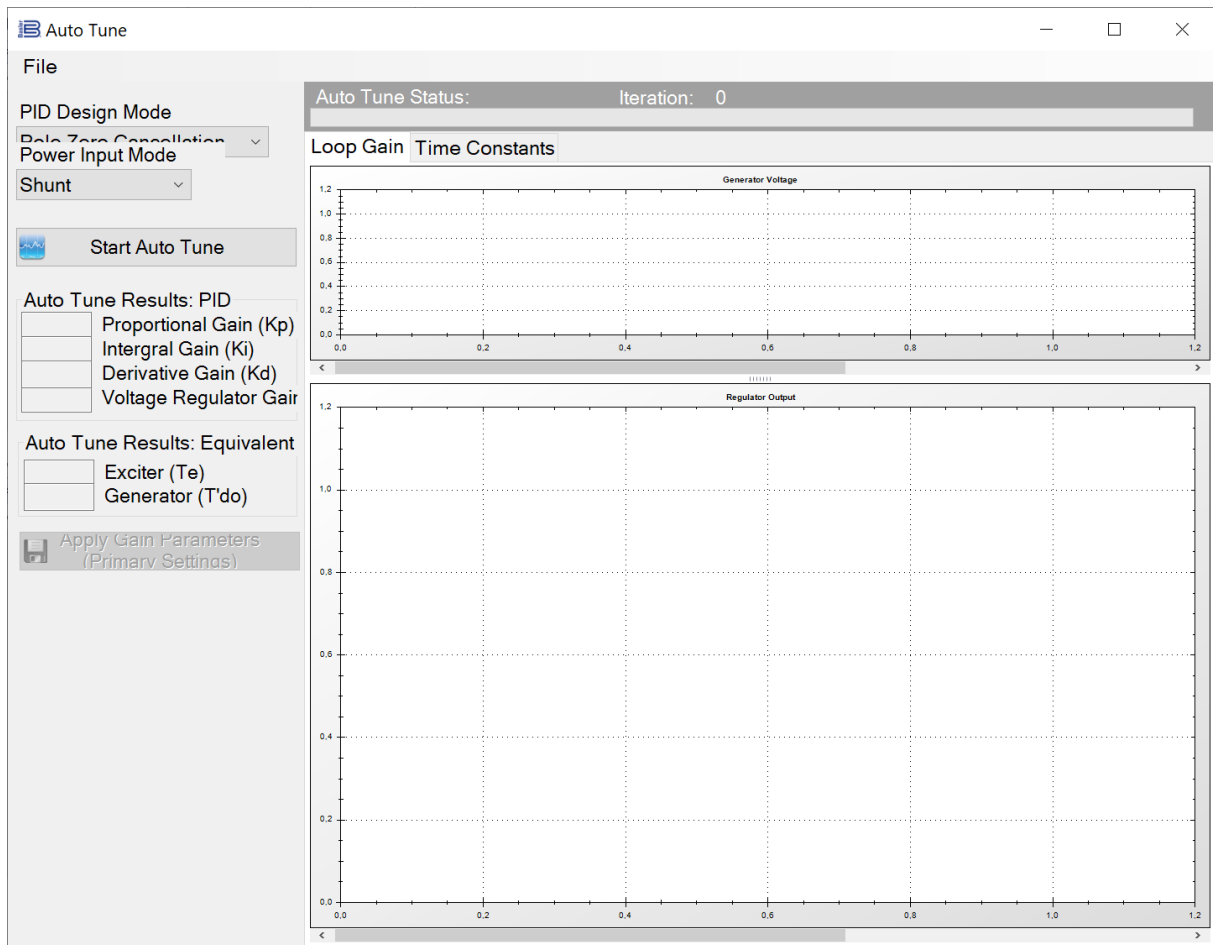


Figure D.4: Screenshot of the Auto Tune Window in Basler BESTCOMSPPlus Software

D.5 Single-Line Schematic for the Laboratory Experiment

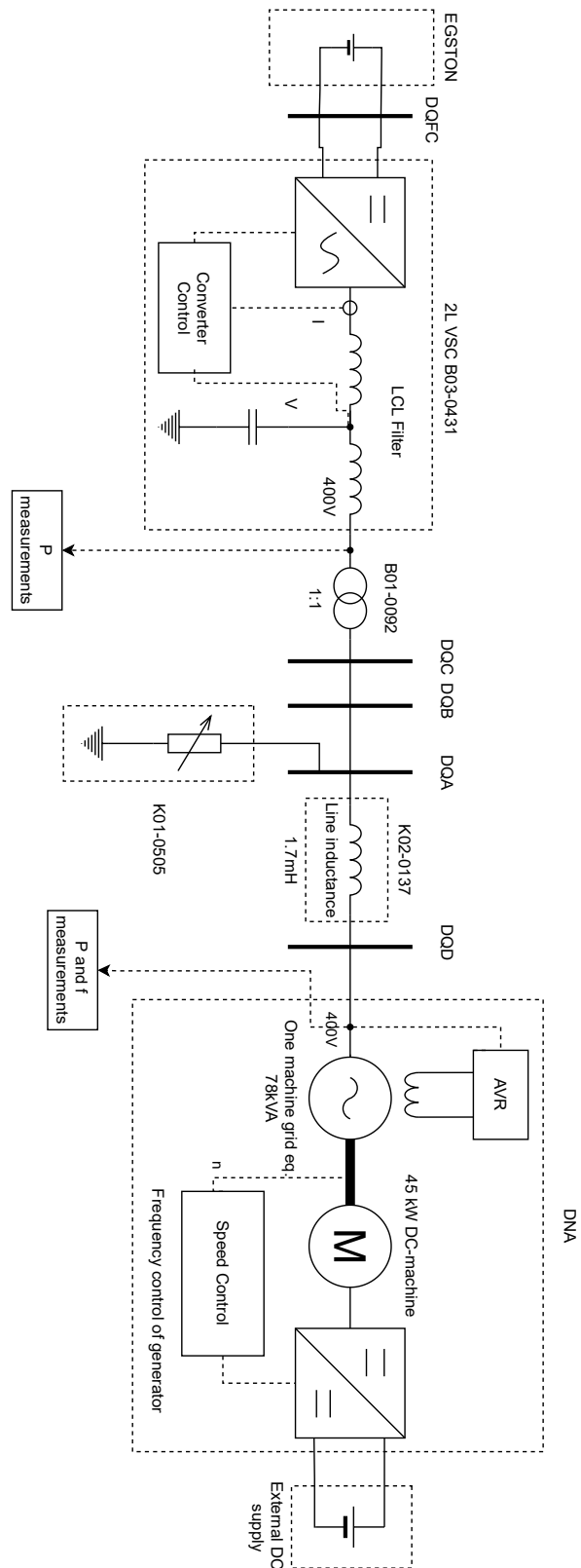


Figure D.5: Single-line schematic for the laboratory experiment.

D.6 Overview of the Smart Grid Laboratory

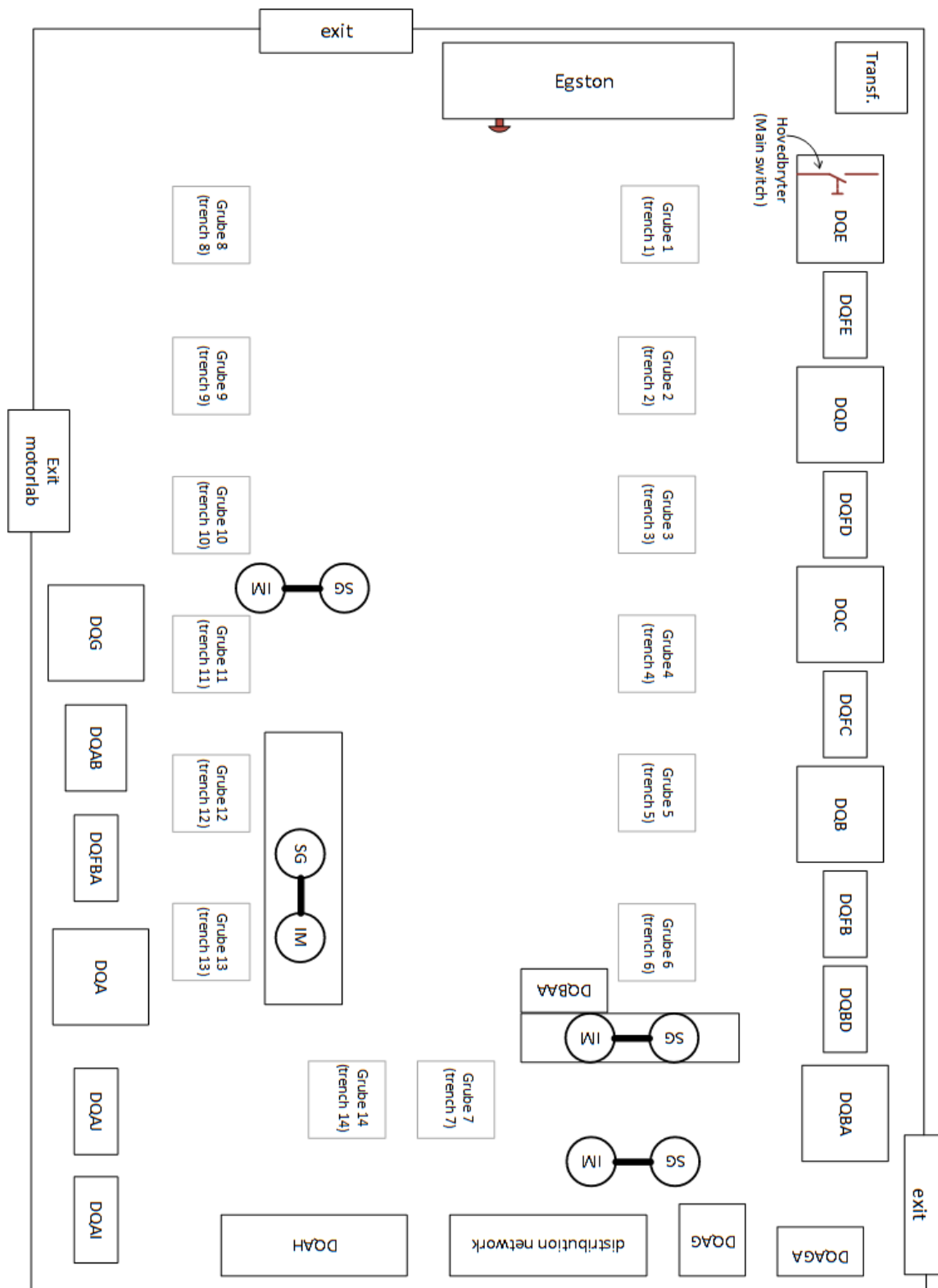


Figure D.6: Overview of the smart grid laboratory [43].

D.7 Schematic of the Smart Grid Laboratory

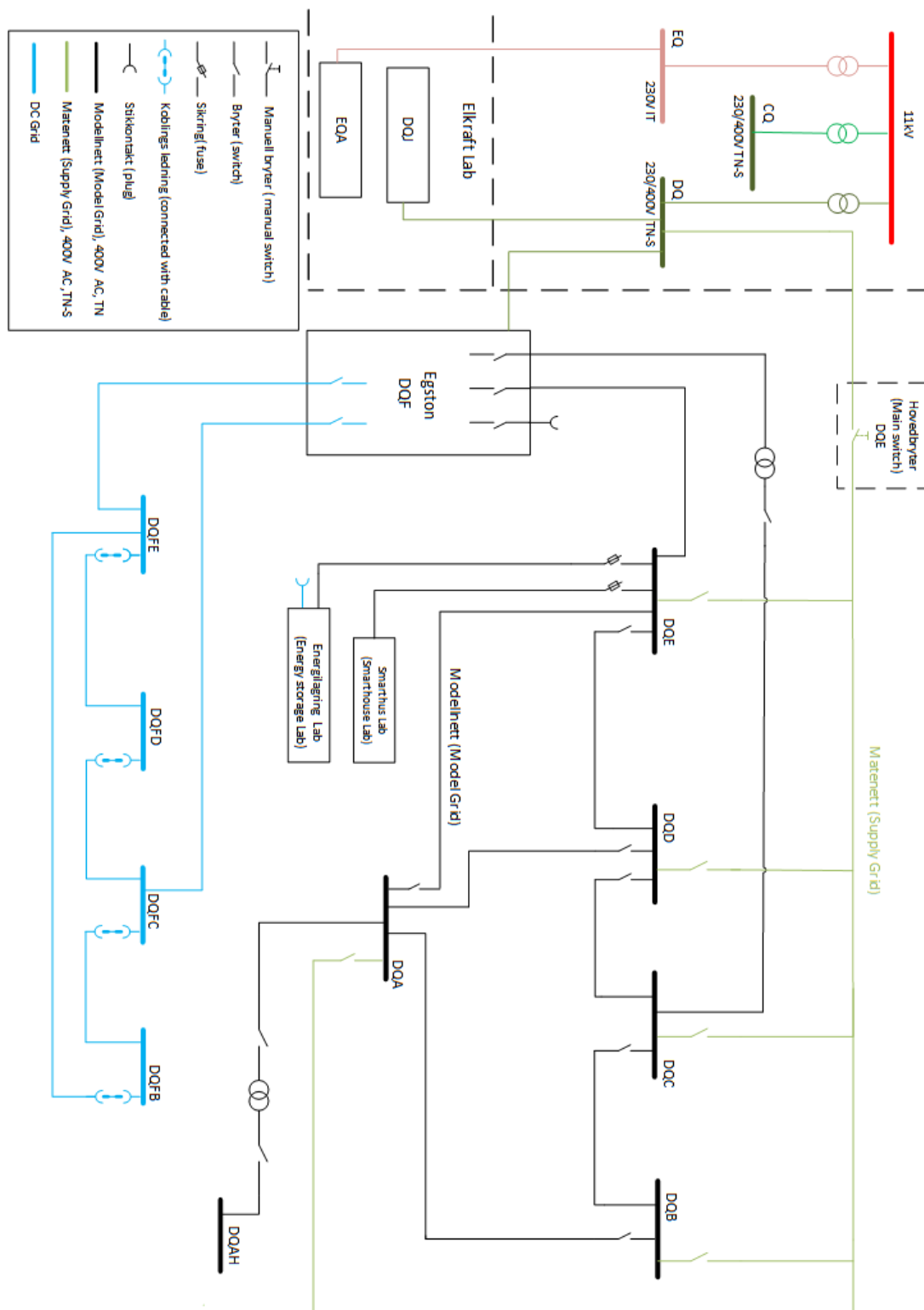


Figure D.7: Single-line schematic of the buses in the smart grid Laboratory [43].

